NASA Technical Memorandum 86290

Investigation of Light Source and Scattering Medium Related to Vapor-Screen Flow Visualization in a Supersonic Wind Tunnel

Walter L. Snow and Odell A. Morris

DECEMBER 1984

NASA

NASA Technical Memorandum 86290

Investigation of Light Source and Scattering Medium Related to Vapor-Screen Flow Visualization in a Supersonic Wind Tunnel

Walter L. Snow and Odell A. Morris
Langley Research Center
Hampton, Virginia

National Aeronautics
and Space Administration
**Scientific and Technical
Information Branch**

1984

Summary

The vapor-screen technique is described in terms of radiometry and Mie scattering to focus on the pertinent variables. Various illumination systems for generating light sheets were investigated and compared. One system tested was a 1-kW, air-cooled mercury vapor lamp which contained an ellipsoidal reflector for increasing its light output. Pulsed-circuit techniques were also implemented to successfully augment the radiant power output, but the decrease in reliability was unacceptable. A second option was a 4-kW, water-cooled mercury lamp which contained Fresnel optics for gathering and focusing the light output. This scheme provided some good-quality data and avoided the annoying acoustic noise associated with the air-cooled lamps. Finally, a 3-W argon ion laser was used to provide reasonably good light screens. This method provided the best overall solution for directing and orienting the sheet. In situ particle measurements using a light-scattering probe were inconclusive because of equipment modifications which may have depleted the particulates in the sample volume. Experiments to servo-control the dew point are described and suggest that the dew point alone is not an adequate indicator of reliable vapor screens. Several attempts to substitute smoke for water vapor as a light-scattering medium are described. The feasibility of using aerosols was established, but problems associated with the efficient production and control of aerosols for a large-scale wind tunnel were not adequately resolved. A periscope system was used to demonstrate the feasibility of removing the recording cameras from the flow. Camera access is essential in the event of malfunctions and allows for alternate detector (e.g., closed-circuit television) choices in the course of a run.

Introduction

Among the indicator techniques used for flow visualization (refs. 1 and 2), the vapor-screen method ranks highly as a means of providing the aeronautical engineer with valuable information concerning wakes and vortices. Such information can be especially valuable at high angles of attack, for which separated and vortex flows occur. The concept involves the use of light-scattering centers which are uniformly entrained in the flow and cross illuminated with a thin sheet of light. In supersonic flows the inherent tendency for moist air to condense upon expansion in the nozzle (refs. 3 and 4) can be used to entrain the particulates. Any disturbance which affects the uniform distribution of particles will either locally add or remove light scatterers, thereby brightening or darkening the screen. The paper by McGregor (ref. 5) is a thorough and readable account of the technique as it applies to supersonic flows. Much of the literature in this area exists in the form of application notes (e.g., see ref. 6). The experiments described in this report were conducted to investigate the current methods used to obtain vapor-screen data in the Langley Unitary Plan Wind Tunnel (ref. 7) with the objective of providing suggestions for a more reliable system.

A brief discussion of the theoretical model is presented to draw attention to the interplay of the light source, the scattering medium, and the detector aspects of the measurement. Experiments to improve and enhance the light source are described along with attempts to measure, control, and alter the scattering medium. An image relay system was also tested in conjunction with efforts to locate the recording cameras in more accessible locations.

This paper is not concerned with the interpretation of vapor-screen data per se. Any model being tested in the facility was deemed suitable for providing test screens to compare illumination and seeding options.

The authors acknowledge the support of Scotty Hall for designing and constructing the electronics required for these studies. David C. Woods provided the instrumentation and expertise for the particle-measurement data. Brooks A. Childers assisted in developing and testing the smoke generators.

Symbols

A	distance from source to slit (see fig. 10)
B	one-half the latus rectum of ellipsoidal mirror (see fig. 10)
c_l', c_l''	expansion coefficients in equation (12)
$d\mathbf{A}$	oriented differential area element ($d\vec{\mathbf{A}}$ in figures)
E	radiant energy
f	focal length
g	angular phase function
I	radiant intensity
I^*	incident radiant intensity
i	$=\sqrt{-1}$
k	extinction coefficient
L	geometric depth
L	lens
l	summation index
M	Mach number
m	linear magnification
N	particle number density

n' real part of complex refractive index

n'' imaginary part of complex refractive index

$\tilde{n}$ $= n' - in''$

$\mathbf{n}, \mathbf{n}'$ unit vectors ($\hat{\mathrm{n}}$ and $\hat{\mathrm{n}}'$ in figures)

Q dimensionless cross section

R redistribution factor defined by equation (4)

R° blackbody radiance

r radius

$\mathbf{r}$ position vector ($\vec{\mathrm{r}}$ in figures)

r_c radius of cylindrical optical element

r_p particle radius

S source function

s dummy integration variable with units of length

T temperature

t time

v particle speed

w radius of laser beam waist

x Cartesian coordinate; dimensionless size parameter

y Cartesian coordinate

α auxiliary angle

δ Dirac function

θ angle

θ_e efflux angle

θ_f fan angle

θ_i incident angle

θ_r refraction angle

λ wavelength

ν, ν' frequency

σ total cross section

σ_{abs} absorption cross section

σ_{sca} scattering cross section

ϕ frequency distribution

ω, ω' solid angle

Subscripts:

bck backscatter

ext extinction

sca scattering

∞ free stream

$\perp$ perpendicular

$\parallel$ parallel

Theoretical Model

Many commonplace experiences illustrate the fact that a beam of light can be rendered visible by introducing light-scattering centers along its path. We may qualify this statement without undue complication to focus attention on the critical variables in the problem. Consider the energy flow through a differential area element $d\mathbf{A}$ located at $\mathbf{r}$ and scattered into a solid angle $d\omega'$ directed along $\mathbf{n}'$. (See fig. 1.) Intuitively, the differential spectral energy dE should be proportional to the projected area along $\mathbf{n}'$, the solid angle $d\omega'$, the spectral interval $d\nu'$, and the time of consideration dt. The proportionality constant defines the intensity, that is,

$$dE = I(\mathbf{r}, \mathbf{n}', \nu', t)(d\mathbf{A} \cdot \mathbf{n}')\, d\omega'\, d\nu'\, dt \qquad (1)$$

The intensity is consequently a radiant power per projected area per solid angle, the latter ensuring its invariance with distance in a lossless medium.

It is the change in intensity as the energy propagates through a medium that is of interest since the change carries information about the medium through which the energy has passed. A phenomenological variable called the extinction coefficient is introduced to characterize the medium. The loss of photons is proportional to both the differential distance traveled ds and to the total number of photons available for scatter. The number of photons is proportional to I.

With the negative sign designating loss, then

$$dI = -kI\, ds \qquad (2)$$

defines the extinction coefficient k, which has units of inverse length and is a measure of the mean free path of a photon in the medium. It is customary to represent k as the product of an appropriate cross section σ (in cm^2) and a number density N(in cm^{-3}). Furthermore, the cross section is composed of two independent contributions. The absorption cross section σ_{abs} is a measure of photon loss to thermal kinetic energy, whereas all other incident photon losses are attributed to the scattering cross section σ_{sca}. Equation (2) is the simplest version of the radiative transfer equation obtained by neglecting source terms and scattering contributions into the beam. It is easily integrable to give

$$I(L) = I(0) \exp\left(-\int_{s=0}^{s=L} \sigma N\, ds\right) \qquad (3)$$

for a beam penetrating to depth L into a medium and with the exponent usually called optical depth. Later we shall also express $I(0)$ in terms of an optical depth characterizing the light source.

Under typical working conditions, essentially all the radiation penetrates the flow without consequence. To consider the scattered component, we introduce the redistribution function R defined such that the joint probability that $\sigma(r_p)I(\mathbf{r}, \mathbf{n}', \nu')$ will be removed from the beam in solid angle $d\omega'$ and frequency range $\nu', \nu' + d\nu'$ and be scattered into $\nu, \nu + d\nu$ in $d\omega$ about direction $\mathbf{n}$ is given by (ref. 8)

$$\sigma(r_p)R(\nu', \mathbf{n}'; \nu, \mathbf{n})I(\mathbf{r}, \mathbf{n}', \nu')\, d\nu'\, d\nu\, \frac{d\omega'}{4\pi}\, \frac{d\omega}{4\pi} \qquad (4)$$

For so-called coherent scattering,

$$R(\nu', \mathbf{n}'; \nu, \mathbf{n}) = g(\mathbf{n}'; \mathbf{n})\phi(\nu')\delta(\nu - \nu') \qquad (5)$$

where g is the angular phase function, δ is the Dirac function, and ϕ characterizes the spectral discrimination of the scatterer (for atoms, this would be line shape). Introducing equation (5) into (4) and integrating over incoming frequencies ν', we are left with

$$\sigma(r_p; \nu)\, d\nu\, g(\mathbf{n}'; \mathbf{n})I(\mathbf{r}, \mathbf{n}', \nu)\, \frac{d\omega'}{4\pi}\, \frac{d\omega}{4\pi} \qquad (6)$$

where $\sigma(r_p; \nu) \equiv \sigma(r_p)\phi(\nu)$.

Expression (6) is a result for single particles and must be scaled by particle density $N(\mathbf{r})$. The emission directed along $\mathbf{n}$, which points to the detector (e.g., a camera, an eye, or a television), is

$$\underbrace{N(r_p; \mathbf{r})}_{\text{Particle density}}\ \underbrace{\sigma(r_p; \nu)\, d\nu\, g(\mathbf{n}'; \mathbf{n})}_{\text{Particle type}} \times \underbrace{I^*(\mathbf{r}, \mathbf{n}, \nu)}_{\text{Light source}}\ \underbrace{\frac{d\omega'}{4\pi}\, \frac{d\omega}{4\pi}}_{\text{Observation geometry}} \qquad (7)$$

where the intensity is superscripted with an asterisk to emphasize the primary beam. If the flow is entrained with a uniform density of particles and cross-illuminated with a "sheet" of light, then the image of this sheet will provide a two-dimensional map of N at the axial station selected.

If uniform entrainment is achieved in the working section, then compressed flow, as within shock regions, will increase the scattering density and result in regions brighter than the surrounding region, whereas vortex flow will decrease the local density leaving "holes" in the screen. From equation (7) we see that an adequate screen is contingent upon the following conditions:

1. An intense light source whose output is contained within a small angle $d\omega$ is required.
2. A uniform entrainment of scattering centers having fixed radius and sufficient scattering cross sections is desirable. The particles should be light enough to quickly respond to the flow.
3. An optimal viewing geometry which takes into account the phase function g, choice of recording medium, ease in interpretation, and so forth, is necessary.

Improvements considered must be transferable from the laboratory table to safe and reliable wind tunnel environments which might vitiate otherwise acceptable solutions.

Illumination Systems

The light source must not only be intense but must also have its output formed into a thin sheet to provide the requisite axial resolution. Although the continuous wave (CW) laser provides a quick and easy option, its choice must be weighed against the hefty power levels (1 to 4 kW) available from high-pressure-capillary discharge lamps. Examples of mercury-capillary lamps available are shown in figure 2. Each lamp consists of a pair of electrodes immersed in a pool of mercury and contained within a quartz capillary having a 1- to 2-mm bore. The lamps must be cooled either by forced air ($\leq$ 1 kW) or by water contained in water jackets. Examples of water-cooled lamps are also shown in figure 2. Radiant output is cylindrically symmetric. The devices are powered by ac or dc supplies and must be current-limited with suitable ballast resistance or electronic limiting circuitry since they operate as arcs and have negative resistance. The dc operation is desirable for exposure times on the order of 1/60 sec to avoid flicker. Reference 9 is a good general source of information for lamps and photographic data.

Mercury capillary lamps have large radiant power output due to their high-pressure operation. The vaporization of the liquid in a closed volume results in internal pressures of 100 to 150 atm, requiring the lamps to be operated in protective enclosures. The beneficial effect of pressure broadening the spectral output with increasing power is illustrated in figure 3. The lines would be delta functions if observed under low-pressure discharge tube conditions. Figure 3 shows the results for 500-, 1000-, and 1500-W operations. In a dilute and weakly interacting gas, the atoms radiate in a small number of delta function intervals. As more atoms are crowded into the emitting volume, the concept of a free atom loses its meaning and many more quantum transitions become favorable because of the formation of molecular-like complexes. For vapor-screen work, it is the "area" under these curves within the wavelength response of the detector which matters.

Mathematically, this dependence is modelled as

$$I(0) = S_\nu(T)[1 - \exp(-\tau_\nu)] \qquad (8)$$

where τ_ν is the optical depth depending on the line shape and the number of emitters. The source function S_ν is, for the most practical cases, the Planck blackbody curve $R^\circ_\nu(T)$ and depends only on the source temperature. The important point is that the rapid spectral variations are due to the line-shape dependence of τ_ν, but for large optical depth this detail is washed out and the output "fills in" the slowly varying envelope governed by $R^\circ_\nu(T)$. This is quite evident in figure 3.

The lamps are rated according to their electrical power consumption. The earliest vendor literature cites a 2- to 3-percent conversion efficiency of power consumed into visible output; however, recent claims are approaching 50 percent! Even if we accept the ultraconservative lowest number, there is still approximately 80 W of CW radiant output power in the 4-kW lamps.

Conversion efficiency must be qualified with spectral modifiers. In particular, the spectral selectivity of the detector defines the range of useful radiant energy. For example, the unaided scotopic eye does not respond to photons outside the 410- to 620-nm band, whereas a good general purpose film such as Kodak Tri-X Pan Film (fig. 4) responds to virtually all photons below 675 nm.

The relative variation in radiant output as a function of electrical power consumption has been measured using a laser power meter which is spectrally flat from 0.3 to 30.0 μm, a photometer filtered to mimic the eye response, a scanning spectrometer, and Tri-X Pan Film. Figure 5 shows the radiant power measurements taken with the photometer and with the laser power meter. The radiant output more than doubles for a doubling of the input power, which is not surprising because of the nonlinear nature of equation (8). It is even more instructive to use the spectrometer data to demonstrate the relative importance of each spectral band, as shown in figure 6. The circle symbols in figure 6 are keyed to the right-hand vertical scale and reflect the totals for all bands. The relative instrument response pertaining to these data was determined by recording a known standard and is shown in figure 7. The spectral bands showing rapid increases in figure 6 include regions with strong atomic lines. If the optical depth were to continue increasing, these bands would eventually saturate at the blackbody limit and no further increases in radiant output would result.

Finally, the results for Kodak Tri-X Pan Film are shown in figure 8. Measured specular density on the photographic records was converted to a relative exposure value with standard sensitometry techniques. This medium has a spectral response well matched to the output of the high-pressure lamps, and the proportional increase in detected output per unit watt is evident.

Pulsed Versus Continuous-Wave Operation

The lamps should operate at the highest possible power to benefit from the accelerated conversion efficiency. Since the increased radiant output is only required during the exposure time, pulsed operation is suggested. The lamp, in effect, can be maintained at nominal power and the power boosted for brief periods to keep the duty cycle low.

To test this idea, the air-cooled 1-kW lamp was operated at 900 W and its irradiance was monitored with a 70-mm reflex camera with Tri-X Pan Film. An exposure time of 1/30 sec was selected to avoid the possible effects of flicker. A 2-μF capacitor was charged to 1400 V to provide a 2-J pulse for 50- to 100-μsec within the 33 msec exposure time. The pulse could be time-shifted within the exposure window to guard against the Villard effect (ref. 9). The Villard effect relates to the fact that an intense, short-duration exposure can sometimes result in subsequent photons destroying the latent image. Since the exposure without flash enhancement required 30 J of energy (900 W $\times$ 1/30 sec), the 2 J energy in the flash amounted to only 7 percent of that total. Thirty observations were made with delays of 0, 10, and 20 msec chosen randomly. The results are shown in table I.

TABLE I. PULSE ENHANCEMENT TEST RESULTS

No. of observations	Flash present	Delay, msec	Relative exposure
9	No		168 ± 46
11	Yes	0	468 ± 100
5	Yes	10	457 ± 75
5	Yes	20	412 ± 75
21	Yes	0–20	452 ± 98

Test exposures taken on Polaroid film led us to suspect the Villard effect, but this was not substantiated by the Tri-X Pan cut-film results, for which more control over processing was possible. There is considerable scatter within each sequence, as evidenced by the standard deviations included in the far right column. At the 900-W setting there is a gain of nearly a factor of three (2.7) for a 7-percent energy increment. Lamp failures were more frequent with the pulse-augmented CW operating mode, and the shot-to-shot variation was excessive.

Conventional Air-Cooled Model

The lamp currently used in the Unitary facility is shown in figure 9. The capillary is mounted vertically

and parallel to a defining slit. The lamp is cooled by forcing service air through the housing and directing it with nozzles to both electrodes. This results in an annoying noise level. Operation without cooling results in rapid detonation. Crossed cylindrical lenses are used to image the radiation exiting the slit as shown in figure 9. The housing is placed within 0.3 m of the wind tunnel test section window. The 16-diopter cylindrical lens images the slit width essentially at infinity, and the negative (−8-diopter) cylindrical lens fans it in the vertical plane. Despite its humble appearance, the lamp has provided some very nice vapor-screen results (ref. 7). To maintain axial resolution, the slit must be kept small. For example, a 0.32-cm slit width images to 2.54 cm at the center of the 4-ft test section.

Even this relatively crude resolution results in only 0.032 sr collected out of a total of 2π. Moving the lamp closer only causes the lens assembly to become the aperture (i.e., energy-limiting) stop. Alternate methods were sought to increase the irradiance on the slit to better utilize the radiant energy of the lamps. Lens-based concentrators were considered but dismissed in favor of a reflective optic solution described in the following section.

Ellipsoidal Collector Model

Another Cartesian surface consistent with the symmetry of the source is an ellipse. An ellipse has the property that any ray leaving one focus will be reflected through the other. It seems conceivable that nearly half the radiation could be gathered and delivered to the same front end optics, as shown in figure 10. The mirror sketched in figure 10 is shown in cross section perpendicular to the cylindrical axis. Figure 11(a) shows the three-dimensional version of the mirror. The efflux angle θ_e through the second focus must be kept small to enable "collimation" of the rays for use as a screen. The angle is clearly defined by $\tan^{-1}(B/A)$. There is a shadow zone which causes a small unavoidable loss shown shaded in figure 10.

Some in-house fabrication of ellipsoidal mirrors was attempted using available programmable milling machines. The equipment drives are only accurate to 0.1 mil (1 mil = 0.0025 cm) no matter how small the program steps. Several elliptical blanks were figured according to the equation $x^2/16 + y^2/7 = 1$, which has an eccentricity of 0.75, focii at $(\pm 3, 0)$, major-axis intercepts at $(\pm 4, 0)$, and y-intercepts at $(0, \pm\sqrt{7})$, with all dimensions in inches.

A typical mirror after hand polishing is shown in figure 11(a). The cosmetic appearance is surprisingly good. The figure was assessed by forming an image of a glowing Nichrome[1] wire placed at the near focal point and photographically examining its magnified (7×) image at the conjugate focus. The image exceeded the geometric value by 20 percent at the half-power points as determined by densitometry. When the mirror is polished and used to illuminate the slit (fig. 10), a considerable bloom is evident in the slit's image (fig. 11(b)). Defocusing the arrangement shows that the extraneous radiation is due to striations caused by machining. (See fig. 11(c).) Although it is relatively easy to configure the piece accurately, the subsequent polishing to bring it to optical tolerances is not as easily controlled.

The mirrors are mounted in the assembly shown in figure 12. The lamps are held rather loosely in spring-loaded supports, making it necessary to provide x and y translation to position the radiating column at the mirror focus. This is done with two mutually perpendicular linear slides as shown. The shafts of the slides were extended to the outside of an aluminum housing for safety considerations. The slit of the standard front end is positioned at the conjugate focus. To compare irradiance gains, the conventional lamp shown in figure 9 was placed alongside that shown in figure 12 and the optics adjusted to irradiate a photometer positioned to simulate the distance to the center of the facility test section. Without readjustment, the same optic was attached to the ellipsoidal housing, the lamp was swapped, and the identical power supply was used to power the source. The results are shown in table II. A high-quality commercial mirror was purchased from an optical supplier and also tested. Theoretical gain is calculated on the basis of solid-angle collection only.

TABLE II. IRRADIANCE GAIN USING ELLIPSOIDAL MIRROR

Theoretical	12 to 1
In-house mirror	5 to 1
Commercial mirror	8 to 1

There is definite signal gain, but the housing has become more complicated and the heat and noise associated with air cooled operation is still unacceptable. Furthermore, even with the excellent commercial mirror there remained a residual bloom around the slit image.

Fresnel Model

The larger water-cooled lamp shown in figure 2 is four times more powerful than its air-cooled counterpart and it operates quietly. Furthermore, the lamp can operate in a glow-discharge mode for safe alignment prior to full-power operation with shields and baffles in place. The disadvantage is that inordinately large optics are required to collect the output. Reflecting optics are inappropriate because of the cooling water jackets, which distort the reflected radiation.

[1] Nichrome: Registered trademark of Driver-Harris Co.

Since the source is linear (fig. 2), a simple projected image will approximate a sheet of light. If s is the distance from the source to the lens and s' is the distance from the lens to the image, then the lens equation is

$$\frac{1}{s} + \frac{1}{s'} = \frac{1}{f} \tag{9}$$

where f is the focal length and the magnification m is given by $|m| = s'/s$. If the 4-in. lamp is projected at a magnification of 12× to accommodate the test section, then the source must be placed nearly at the focal plane. Furthermore, to efficiently collect energy, the lens must subtend a large angle as seen from the source. For an extended object, many of the rays will intercept the lens at large angles and severe aberrations are expected. To avoid massive aspheric components, Fresnel lenses were used to test the technique. The refracting power of a surface depends only on the material index and the angle which the incoming ray makes with the local normal. A Fresnel lens is made by translating concentric zones of the requisite surface to a plane, reducing the lens thickness (ref. 10) and resulting in the characteristic grooved appearance.

A prototype device is shown in figure 13. An intermediate slit was required to trim the image of the water jacket, the image being quite intense even when filtered water was used because of the scattering from the very intense arc core. It is evident that the source and the lens are of comparable size and closely spaced. The aberrations were severe (ref. 11). They were alleviated in part by bending the lens concave toward the source (ref. 12). The schematic in the figure shows top and side views of the fan. The undesirable convergent nature of the image formation process is suggested in the top view. Photographs of the irradiance at three planes are shown in the inset. The photographs are overexposed to emphasize the aberrations. Not shown is the chromatic aberration which is normally quite evident for Hg arcs, which have distinct spectral signatures. Chromatic correction can only be accomplished by compounding lenses of differing refractive indexes. A Fresnel doublet was used as a compound lens in place of L_2 in later tests. This lens (fig. 14), with a front focal length of approximately 25.4 cm, was designed for projecting TV images and gave markedly improved image quality despite persistent chromatic distortion.

Laser Approaches

The laser offers the easiest solution for providing a sheet of light, since its output is a highly collimated pencil of radiation and only requires decollimation in one dimension (ref. 13). This is usually accomplished by passing the beam perpendicularly through a cylindrically symmetrical component. At this stage the laser is used purely as an intense source with its characteristic coherence, polarization, and monochromatic advantages ignored. Typically, the laser will have a normalized irradiance profile ($TEM_{0,0}$ mode) given by

$$\begin{aligned}\frac{I}{I_o} &= \frac{2}{\pi w^2}\exp(-2r^2/w^2) \\ &= \frac{2}{\pi w^2}\exp\left(-2x^2/w^2\right)\exp\left(-2y^2/w^2\right)\end{aligned}$$

where r is the radius, w is the beam waist, and I_o is the peak intensity. The signal has dropped to 13.5 percent at the waist, and over 99 percent of the energy occurs within the circle having radius $1.5w$. Typically, w will be 0.4 mm, a value consistent with a beam divergence of 1.3 mrad. One method of fanning the beam is shown in figure 15(a). Since w is small, the rod must have high curvature. Virtually all the rays are incident on the rod at large angles, resulting in large reflection losses. This can be minimized by making the first surface planar, as shown in figure 15(b). The fan angle θ_f can be changed by adjusting r_c and, to a lesser extent, the index of refraction n'. An auxiliary angle α has been included to simplify the following derivation. Obviously, $\alpha = \theta_i$.

Snell's law states that for incident and refracted rays,

$$n' \sin\theta_i = \sin\theta_r$$

The geometry shows that $\sin\theta_i = y/r_c$; therefore, $\theta_r = \sin^{-1}(n'y/r_c)$. Since the fan angle is

$$\theta_f = \theta_r - \alpha = \theta_r - \sin^{-1}(y/r_c)$$

then

$$\theta_f = \sin^{-1}(n'y/r_c) - \sin^{-1}(y/r_c) \tag{11}$$

This function is plotted in figure 16 for a glass with refractive index of 1.55. For meaningful angles, $y \leq y_{max} = r_c/n'$. At $y_{max}, \theta_f = \pi/2 - \sin^{-1}(1/n')$, which is 50° for the case plotted. Ninety-nine percent of the energy will fall within $y = (1.5)(0.4\text{ mm}) = 0.6$ mm for the case cited. Substituting in equation (11), θ_f becomes 1.9°, 3.8°, and 31.6° for respective values of r_c of 10, 5, and 1 mm. To avoid very small rods, components can be used in tandem so that the second component amplifies the divergence of an already diverging beam. A prototype device made with a split rod having a 10-mm radius is shown in figure 17. The sketch illustrates how a second optical component amplifies the divergence of a refracted ray. The fan angle is adjustable to some extent by moving the second lens. Each of the two components looks like a can with a centered hole in the bottom. One "can" telescopes into the other. A cylindrical lens is glued over each hole so that extending the telescope separates the elements. The inset shows the assembled module threaded to be compatible with a standard laser bezel. The hole and slot were provided to

allow beam dumping to monitor power. The device provided adequate fans for testing despite striations due to imperfections in the glass, but it was sensitive to misalignment. In future designs a simple 5× laser beam expander might be used in conjunction with a nominal cylindrical lens. Then, the 99-percent "waist" would be $y = (1.5)(0.4)(5) = 3$ mm and a 5-mm-radius cylinder would provide a θ_f of 32° without critical alignment. The 3-mm dimension along the tunnel axis is acceptable and can be focused tighter if desired.

Some considerations were given to sweeping the laser beam so that the flow region could be "painted in." The advantage is that there is no optical degradation of the high-quality laser beam. A rocking mirror driven with an eccentric cam is shown in figure 18(a). The extent of the sweep could be controlled by the cam as could its residence time in any location. There is no advantage in data acquisition time since the much increased intensity is exactly compensated for by the decreased residence time of the beam within any region of scattering centers. Inexpensive galvanometer-based scanners which can be driven by signal generators are available. One could conceivably program the drive to accentuate certain areas of the flow and to deemphasize others (e.g., in regions susceptible to highlighting). The rocking-mirror and fanned-beam approaches result in pie-shaped illumination fields with the apex at the reflecting, or dispersing element. One attempt to avoid this problem is shown in figures 18(b) and 18(c). A 90° prism was mounted on the end of a rack which was driven by a pinion mounted on a reversible motor (fig. 18(b)). A fixed mirror reflected the beam from its movable companion as shown in figure 18(c). The illumination field had the requisite rectangular format, but the rather crude translation device caused unavoidable jitter in the beam even though it appeared to move smoothly to the eye. An example is shown in figure 18(d). The beam was thrown 2 m to the film plane, where its irradiance was recorded as the squiggly trace shown. In contrast, a weakly fanned laser beam (1 m optical throw) is shown perpendicular to the scan along with a parasitic ghost caused by a reflection. The exponential attenuation of the fanned laser is evident in the photograph.

Supersonic facilities often have very expensive optical equipment to obtain schlieren and shadowgraph pictures. Hybridized methods which make use of such configurations (e.g., ref. 5) have not been considered here.

Comparison of Illumination Techniques

In this section, the illumination techniques investigated in this study are rated. Each technique brings with it different variables to evaluate and ultimately involves subjective judgement about the image quality of actual vapor-screen pictures. Nevertheless, some general criteria emerge.

Pulse-enhancement techniques are attractive because they use existing hardware which is optically acceptable and increase its efficiency with no modifications. Output was increased as expected, but the repeatability and reliability were degraded due to lamp failures. Since reliability cannot be compromised for a method to be used in a production facility, this approach is currently ruled out.

The ellipsoidal mirror increased the light in the useful beam by an order of magnitude. However, there was a slight degradation in image quality perpendicular to the sheet. Furthermore, adjustments required to align the lamp with the cylinder axis complicate the mounting, and the undesirable heat and noise associated with air-cooled lamps make this an unacceptable choice.

To ensure resolution of fine spatial detail, the irradiance profile in a plane perpendicular to the sheet should be narrow and have crisp edges. Otherwise, light scattered from adjacent planes may contaminate the image and reduce its contrast. The irradiance profiles for four of the source options studied were determined by setting the lamps at the nominal working distance (0.91 to 1.22 m) and using the original system as standard. The results are shown in figure 19. The profiles have been normalized to unity at peak irradiance to neutralize the gain in power, and the scale is logarithmic. The laser profile is narrowest of all, as expected. The original and ellipsoidal cases are quite similar except in the wings. The scattered radiation in the wings probably has the same origin (residual tooling marks) as that shown in exaggerated form in figure 11(c). The commercial mirror is an order of magnitude better than the in-house version used to prepare figure 11. Finally, the Fresnel lens contributes considerable flare due to chromatic aberration and scatter. The lens looks "milky" when irradiated with intense light. This scattered component shows up outside the geometric image. The significance of these "wings" lies in the fact that photographic materials usually have a sensitivity range of several orders of magnitude. Consequently, as the exposure increases, the wings become visible and the spatial resolution of the sheet is degraded, thus obscuring detail in the vortex structure.

Although physical variables are useful to describe the system for design criteria, the ultimate worth of a configuration is the visual quality of the resultant screens. Figures 20 and 21 should help to acquaint the reader with the particular configuration used to compare illumination techniques. Figure 20(a) is a conceptual sketch. The light source under typical conditions would be similar to that shown in figure 9. To augment the screen intensity, a second lamp is mounted above that shown and tilted downward to illuminate a com-

mon area in the flow. This technique is referred to as a "twin 1-kW" technique. Figure 20(b) shows the spatial relationship of the two vapor-screen cameras. The backscatter arrangement shown is commonly used, although the forward scatter can be more intense. The side-mounted cameras provide a less desirable perspective view and are used primarily to back up the inside camera, which is subject to failure and is inaccessible during a run sequence.

Unquestionably, some aeronautical models provide richer vortex flow detail than others. For example, finned missile models at high angles of attack usually provide a distinct vortex pattern. A comparison series of tests was done with a parawing shape which was available. The detail of the model is unimportant for our purposes. A picture from the inside camera is shown in figure 21 to orient the reader. The mounting sting knuckle is shown as a defocused shadow. The screen was positioned just aft of the model to provide as much vortex information as possible.

One of the initial objectives of the study was to increase irradiance while preserving its slice-like format. The increased light flux can be used either to decrease exposure time or to decrease water vapor content in the flow. Short exposure times are desirable to avoid time averaging. Since condensation adds energy to the flow and affects critical variables such as Mach number, it is also desirable to maintain the dew point as low as possible.

The format of figures 22 to 24 reflects these tradeoffs by displaying dew point versus exposure time. It is not possible to judge the quality of the photographs on the reduced scale required to make up the collages. Later figures show enlarged versions better suited for judging quality. The properly exposed frames are all deemed adequate from a user's standpoint. Thus, in general, if more scatterers are added, the exposure time can be decreased while maintaining image quality.

Conversely, if exposure time is lengthened, the facility can be operated at a lower dew point. In the figures two views are provided. The side-mount camera shots are generally a little brighter since they take advantage of the increased efficiency for forward scatter and backscatter. The inside views are more acceptable from a symmetry standpoint and are the preferred orientation for interpretation purposes.

We may draw the following conclusions from figures 22 to 24:

1. Both the Fresnel and the laser system offer advantages in exposure which, as we have noted, can translate to lower dew points or shorter exposure times or both. This can be shown by comparing figures 22(a), 23(a), and 24(a). The laser is at an advantage for these particular comparisons since its irradiance profile is fixed inherently by the cavity design. More light can be dumped into the screen with the other two techniques by increasing the width of the acceptance apertures. For some field applications for which the detail is coarser (e.g., full-scale facilities), the Fresnel or the original conventional system might incur advantages from increased radiant power into the light sheet.

2. Judging only from the results of this test sequence, we find the image quality would be adequate for the original system, better for the Fresnel system, and best for the laser system. Even considering day-to-day variations, it is safe to say that neither of the new systems, the Fresnel or the laser, degrade the image quality.

3. The Fresnel prototype is easier to operate and to align than the original system, especially when the latter is used in the twin mode, since this involves careful co-alignment of two separate systems. The laser would probably be chosen in terms of operational simplicity, and in most instances has been found to be quite reliable (ref. 14).

Results from the original, Fresnel, and laser systems are compared in figure 25 for an exposure time of 1/4 sec. These shots were selected from the matrix of contact prints in figures 22(a), 23(a), and 24(a), and the exposure times were constrained to 1/4 sec in order to minimize the effects of model dynamics on picture clarity. A higher dew point was required to get a usable negative for the original system. Note that this figure was prepared by simultaneously contact printing the three negatives, so a compromise in contrast is required. The same negatives were printed individually, with the freedom of adjusting conditions for maximum contrast. These results are shown in figures 26 to 28. Comparing results is complicated by the fact that altering contrast in the printing involves subjective choices. Part of the loss of detail in figure 26 (original system) is due to multiple scattering caused by operating at a higher dew point. The Fresnel prototype system results in somewhat better detail (fig. 27). The laser-system photograph seems to offer the best contrast. Striations in the rod produced intensity variations which could be removed by using a better optical fanning rod or by dithering the existing one slightly.

Figure 29 demonstrates the effect of quadrupling the light intensity while proportionately reducing the exposure time with the laser as the light source. The laser has an in-line power meter and the output can be dialed quickly and conveniently so that tunnel conditions will not change appreciably. The higher intensity shots seem decidedly better, yet the concept of reciprocity (ref. 9) suggests that all photos should give comparable results. In the section entitled "Illumination Systems" we noted that power conversion efficiency increased with electri-

cal power. This single test sequence suggests that intensity is favored in the intensity-time product for obtaining high-contrast vapor-screen images. If substantiated by further investigation, one might be tempted to use a high-power pulsed laser for the light sheet. However, the number of scatterers irradiated by the beam is proportional to vt, where v is the particle speed and t is the pulse duration. For pulsed lasers, t might be shorter than 10^{-8} sec. Yet, the number density of scatterers should only be increased to the onset of multiple scattering. Beyond this number density, the images become noisy or grainy.

Scattering-Medium Investigations

In this section a brief description of particulate scattering is given. Then, in the next section, the results of tunnel tests to measure the size distribution of scattering centers are presented, followed by a description of partially successful attempts to substitute smoke for the water droplets as the scattering centers. The physical description of scattered light hinges on the calculation of cross sections, as suggested by equation (3). This is a problem in electromagnetic theory and is tractable for particles with geometries conforming to constant surfaces in standard reference frames. By far the most frequently encountered solution is that for dielectric spheres of radius r_p and characterized by complex refractive index $\tilde{n} = n' - in''$. The problem was first worked by Mie and bears his name. Several excellent sources exhaustively treat the topic. The most notable is by Van de Hulst (ref. 15). The boundary-value problem is solved for plane waves incident on the sphere and, as is characteristic of many electromagnetic solutions, is represented in series form. It is convenient to write the answer in terms of the dimensionless size parameter $x = 2\pi r_p/\lambda$, where λ is the radiation wavelength. The problem is schematized in figure 30(a). Two typical size parameter choices for which calculations were made are shown in figure 30(b). The detected radiation is composed of a superposition of plane waves that get around the particle and those that scatter from it. Furthermore, it is desirable to nondimensionalize the cross sections by dividing by the shadow area of the scatterer πr_p^2 to define an efficiency factor $Q = \sigma/\pi r_p^2$. The angular dependence of this problem is expressed in terms of Legendre polynomials of order l with coefficients c_l' and c_l''. The coefficients are complicated (though straightforward) combinations of spherical Bessel functions of half-integer order. In terms of these coefficients, the scattering efficiency Q_{sca} is

$$Q_{\text{sca}} = \frac{2}{x}\sum_{l=1}^{\infty}(2l+1)(|c_l'|^2 + |c_l''|^2) \qquad (12)$$

Explicit formulas are found in the many references. Those of Wickramasinghe (ref. 16) were used for this study and were programmed in BASIC computer language for a calculator to prepare plots. The highly oscillatory functions are calculated using recursion relations to maintain accuracy.

Figure 31 shows how the efficiency factor varies as a function of size parameter for spheres having the index of refraction of water (1.33). Several points are to be noted. First, the efficiency increases exponentially for the region where x is small, which is of primary interest in applications wherein particles must follow the flow. The actual cross section increases quadratically with particle radius in conformity with the definition of Q. Second, the efficiency oscillates with x and asymptotically approaches $Q = 2$, both of which indicate the diffraction nature of the phenomenon (ref. 15).

In figures 32 and 33, the conventional log-polar scattering diagrams are shown for particles of water having size parameters of one and five, respectively. In these diagrams the components parallel and perpendicular to the scattering plane defined by the incident and scattered directions have been separated out. The ability of smaller particles to scatter radiation is strongly dependent on polarization at 90° to the incident beam direction. The small particles essentially have one dominant term in the series expansion as shown in figure 32(b) and this results in the familiar dipole pattern. On the other hand, the larger particle of figure 33 has at least five significant terms and the lobe-like structure of its scattering plot is evidence of the superposition of the contributions. Note the scale of the figures. The polar plot corresponding to $x = 1$ would fall completely within that for $x = 5$, in accordance with the graph of figure 31.

Facility Scattering Measurements

To improve the reliability of vapor-screen experiments, an attempt was made to characterize and control the scattering medium. Knowledge of the size distribution is useful for modelling purposes as well as for assessing alternative scattering media. The disadvantage of using a condensate are well known and hinge on the fact that heat is released to the flow with consequent change in static conditions, Mach number, and so forth, as detailed in references 3 and 4.

Since scattering signatures of spherical particles are unique functions of the radius, it is sometimes possible to infer particle size from angular variations of scattered radiation. One device based on this principle is shown mounted in the test section in figure 34. This instrument is known as a Knollenberg forward scattering spectrometer probe (FSSP). (See ref. 17.) The sample volume lies within a tubular inlet aligned along the cylindrical axis of the instrument. The inlet is supported by two arms, one of which is visible in the pho-

tograph and is distinguished by its white hemispherical cowling.

Light from a 5-mW He-Ne laser is propagated inside one of the support arms, is deflected 90° into the sample volume where it is focused to a 200-μm-diameter waist, and proceeds to the second support arm where detection optics accept radiation within a 4° to 18° conical annulus. Complex pulse height discrimination and transit time circuitry allow the particles to be sized. The instrument has 4 overlapping size ranges, with each range divided into 15 linear intervals providing up to 60 size channels in the 0.5- to 45.0-μm range. This instrument and related models are described by Knollenberg in reference 17. The instrument is designed for subsonic flow (usually 10 to 125 m/sec), so an insert was made to reduce the flow velocity to Mach 0.3 at the Mach 2.0 condition for tunnel testing.

An insignificant number of particles were detected under vapor-screen run conditions. Although it is possible that the particle size range is below the range of the instrument (i.e., < 0.5 μm), a more probable explanation is that the particles are vaporized as the flow is decelerated within the inlet. (See ref. 18.) This instrument was effectively used (unmodified) as a laboratory tool to size particles in other phases of this investigation.

Previous facility experience has indicated that the dew point required to establish acceptable vapor-screen results is a monotonic (though sometimes weak) function of Mach number. The dew point readings were obtained with a standard chilled-mirror hygrometer, which was connected to the tunnel forward of the test section. To better quantitatively assess this dependence, an automated fluid-injection system was tested. All previous work involved introducing known volumes of water (typically 2 to 3 liters) downstream and allowing the dew point and the vapor density to subsequently rise. Having reached a desirable level of screen visibility, the water was shut off and the condition would deteriorate as the tunnel dried out. A solenoid which was activated by a different signal generated by the dew point recorder output was installed in the injection line. This allowed setting the dew point and letting the system call for water until it had satisfied the set point. To monitor the scattered light during the course of these experiments, the inside-camera housing was modified to accommodate a photomultiplier tube. The geometry was arranged to allow the detector to monitor a conical volume with a 10° included angle. A second phototube monitored the light output of the lamps used to generate the light sheet; otherwise, incident light intensity changes could be misinterpreted as true scattering changes.

A hastily contrived add-on experiment was conducted to examine the effects of adding a fluorescent dye (rhodamine 6G) to the water in hopes that the working fluid would absorb some of the light and reradiate it into the detector to augment the anticipated Mie component (refs. 19 to 21). Two data sets were acquired, one at a constant Mach number (figs. 35 and 36) and another at varying Mach numbers (figs. 37 and 38). Each of the variables was measured as a function of time into the run and is so plotted in subsequent figures. The time scale is in minutes and is compatible with the circuit distance, which is on the order of 305 m (ref. 7). Solenoid malfunctions accounted for the loss of data indicated in figures 35 and 36 as "injection system problems." The solenoid was replaced prior to taking the second data set and remedied the problem, as can be seen by the constant output for varying Mach numbers in figure 37(b) when the dew point was set for 10°F for the time interval from 15 to 45 minutes.

Figure 35 shows that the variation in scattered-light output tends to follow dew point changes, especially in the 15°F to 20°F range which previous work had deemed suitable for good screens. When the dew point is further increased, the correlation of scattered light with dew point can even be negative! The signal also becomes very noisy, as shown in the traces from the photomultiplier viewing the screen from the conventional camera position. (See fig. 39.) This noisiness may be due to multiple scattering because the fog is dense to the eye under the higher dew point conditions. Droplets which form on the window of the protective housing can also contribute. At the low Mach number condition, the screen appears very patchy. Also, a given dew point level is less effective in terms of scattered light as the Mach number increases. To emphasize the relationship between scattering and dew point, the ratio of these quantities is plotted in figures 36 and 38. We are dealing with the formation of droplets given appropriate boundary conditions, one of which is the dew point. There is, therefore, no direct relationship with scattered light, as would occur if aerosols were entrained in the flow. Figure (36) shows that under certain circumstances the scattered light tends to decrease with increasing dew point. In any case, there appear to be other variables affecting the formation of droplets. The reduction in scattered light with increasing Mach number is evident in figure 38(c), since dew point was held constant for most of that series. To average out the short-term fluctuations, the mean and variance of the ratio of scattered light to dew point over 5- or 10-minute intervals was computed. These values are indicated in figures 36(b) and 38(b). The correlation coefficients for these ratios have also been calculated over the same intervals and are indicated in parentheses on the plots. The horizontal bar indicates the time interval over which the correlation was computed, and the vertical bar indicates the root-mean-square deviation from the mean. If the dew

point is increased above the value considered suitable for vapor screens, there is a diminishing return in light scattered. Beyond the 70-minute mark in figure 38 this was the case. The level of scattered light (fig. 35(c)) remained essentially the same as the dew point increased. There is an overall positive correlation of scattered light and dew point over the testing conditions independently deemed suitable for vapor-screen formation, but the situation is by no means simple. These findings suggest that dew point alone does not ensure high-quality vapor screens. At lower Mach numbers, although the correlation remains positive, the signal becomes more erratic. This condition was also judged to be "patchy" to the eye. At the higher Mach numbers, the correlation remains high and the signal much more constant. The screen becomes less intense and more finely grained.

The final segment of the run for which the Mach number varied (105 to 125 minutes in fig. 38) was used to test the potential advantage of adding dye to the scattering fluid. Most of the light introduced in the illumination beam proceeds through the test section. This is because the total projected geometric area offered by the scattering centers is a small fraction of the cross-sectional area of the beam. The light that does impinge on the particle is either scattered or absorbed. For substances like water the absorption is very small. Adding an absorber to the particle removes energy from the beam and converts it to heat unless the additive is a fluorescent material which will reemit the absorbed radiation at a different wavelength band. If the scattering properties are unaltered by the addition of the dye, then the net result should be to extract photons which would have gone unscattered and redirect some of them toward the detector. For these tests, the pure water vapor was purged from the tunnel and rhodamine 6G was added to the water supply. The absorption and emission characteristics of this compound are shown in figure 40. (Compare ref. 19.) The lifetime of the transition is on the order of 4 nsec; therefore, even at Mach 3, the particles move on the order of 1 μm before reemission, so no smearing of the detail is expected. The emission-absorption regions of the dye are indicated in the emission curve of the light source in figure 41. It is significant that the source emits in a region which will be absorbed by the dye and that the reemission is compatible with the spectral response of the detector. Both requirements are met for this work. In figure 38(b), we note an increase in correlation coefficient as well as in the signal level, but the effect is not dramatic. To fully exploit the effect, one would have to experiment with varying concentrations of dye and test over the full Mach number range. Since all the adverse aerodynamic effects attendant on using water vapor would persist, the use of dye seems inadvisable at this time.

Even discounting the disadvantages of introducing energy-exchange mechanisms resulting from condensation, we have seen that dew point control alone does not guarantee effective screens. In fact, in the low Mach number range ($M = 1.47$ to 1.70), it has not been possible to reliably obtain vapor screens within the facility's normal operating envelope. When attempted, the water vapor tends to pass through the test section in unsteady bursts or in layers along the floor. On the other hand, the entrainment of particulates which are light enough to follow the flow should, after several circuits, result in uniformly dispersed particulates even in the low Mach number case and provide excellent initial distributions for the vapor screens. For a scatterer to be seriously considered, its size distribution must ensure that it can follow the flow (refs. 22 and 23), it must be nontoxic and noncorrosive, it must be producible in controlled amounts, and, for this particular facility, it must be produced in large quantities (i.e., to fill volumes on the order of 7080 m^3.

Kerosene-based foggers are successfully used in wind tunnels for localized particulate seeding in anemometry work, but their use in large-scale applications in closed-circuit systems can be dangerous (i.e., explosive), and furthermore, prolonged use results in oily residues that must be cleaned at considerable expense. Dioctyl phthalate is an excellent choice for small-scale applications, and commercial generators are available, simple to use, and inexpensive (refs. 24 and 25). A test generator pictured in figure 42 was purchased for laboratory evaluation. Compressed air is applied to a nozzle arrangement which is submerged in the liquid, and aerosol formation is based on cavitation principles. This liquid also tends to leave an oily residue. This unit can supply particles having diameters of 0.8 μm at a rate of 10^{11} to 10^{12} particles per minute. Models several times larger than that shown still would provide inadequate aerosols for large-scale tunnels so this avenue was not pursued in this study.

Some experimenting was done with smoldering cellulose materials, since they have been effectively used for flow visualization in the past. Most work was done using tobacco, since a critical factor is to evolve a system which is as standardized as possible. Our limited experience with wood and paper products yielded nonrepeatable results often related to where and how the materials were obtained. The primary emphasis was to examine methods of easily starting and stopping the smoke production, since in closed-circuit facilities there is a danger of oversupply. Too much smoke obliterates the detail. On the other hand, the air is exchanged for drying purposes, and this coupled with unavoidable leakage tends to dilute the smoke. Ideally, a manual or servo-controlled system is desired to keep the number density of scatterers fixed.

Figure 43 shows an early attempt to design a smoke generator, which burned wood shavings. (See ref. 26.) The receptacle for the combustible material consists of a 0.61-m-long, 1½-in-diameter pipe with reducing couplings on either end. Compressed air is supplied to the pipe containing smoldering shavings. The smoke-laden air leaves the pipe and enters the filter tube shown above it. The filter is filled with steel wool to remove large particulates. After leaving the filter, the smoke is routed either to an outside vent or to the desired location by using solenoid valves. The system worked reasonably well but was awkward to start since the coupling on the supply side had to be unscrewed, the shavings lighted, and then the air supply reattached. The arrangement provided a continuous flow of smoke for 10 to 20 minutes and the "fuel" burned quite uniformly as evidenced by examining the ash after the tests. Tarry- and watery-type residues tended to accumulate in the tubing in the course of the experiments and prompted the search for a suitable condenser.

A second model which incorporates several new features is shown in figure 44. It is scaled-up in size to allow greater volumes of smoke per loading. The 2-in-diameter pipe is 0.91 m long and has quick disconnects on either end so that spent canisters can be replaced rapidly. To ignite the mixture, a diesel glow plug has been introduced on the inlet end. The tube is loosely packed with shavings placed around the glow wire prior to the assembly. Air is applied at reasonably low flow rates and power is supplied to the plug. After ignition, combustion is verified by watching for the appearance of smoke, power is removed from the glow plug, and the "flame front" propagates down the tube. The smoke again is filtered to remove large particulates and then is passed through a Graham condenser placed behind the generator. A rear view of the assembly is shown in figure 45. Smoke proceeds down through the helical coil, which is contained in a water bath. Condensation forms and drips from the bottom of the helix into the flask. Smoke collects in the flask and is drawn off to the T where it is routed either to the flow or to a suitable vent. The device performed reasonably well in short laboratory tests and the condenser removed most of the objectionable tarry residues. The glow plug was effective in starting the generator, but some irregular burning was noted. Occasionally a core of ash was found around the plug and the embers extinguished. Difficulty in obtaining "standard" shavings complicated the evaluation of the device.

A third model in the series is pictured in figure 46. Three canisters are mounted in parallel to provide increased supply for the tunnel, and tobacco was chosen as the combustible. Tobacco is known to produce smoke particles in the 1-μm range and has been used for flow visualization in the past. Driven by the cigarette industry, the quality control of marketing a consistent, evenly burning product is well in hand. For these tests, 22.7 kg of "redried strips" were purchased. This product comes in compressed bales consisting of pieces ranging in size up to about 2.5 cm. The pieces were crumbled by hand prior to loading. The three-tube device was tested with mixed results. Burning was irregular and often stopped prematurely. This was attributed to a thermal engineering problem. The rather massive metallic structure apparently cooled the combustion zone to the point where burning could not be sustained. As with previous models, the inability to watch the process proved bothersome. Progress of the combustion could only be monitored indirectly by noting the diminution of smoke and by feeling the side of the tube to locate the flame front.

In an attempt to resolve both the thermal-conduction and the viewing problems, several loadings were made in Pyrex[2] glass tubes, as pictured in figure 47. The tubes are readily available in a variety of diameters. The nominal 3-in. by 48-in. tube pictured provided sufficient volume to generate smoke on the scale required for the large tunnel volume. The tube is shown in a makeshift mount in figure 48. The inlet end is shown unstoppered as it might appear in a tunnel installation. The reduced pressure in the tunnel provides suction on the stoppered end. The tobacco is ignited and the flame propagates up the tube. The tube is sloped to allow draining of liquid by-products of the burning. The rate of burning was controlled by throttling the suction flow. The concept worked reasonably well, but with the large-diameter pipes the burning often was irregular, sometimes snaking down the fuel volume and sometimes confining itself to a narrow region near the top, necessitating rather frequent rotation to use up all the combustible. Some of the incomplete-burning problems could be averted by using a bank of smaller diameter tubes. The model is at best awkward to use and is too slow to provide an effective generator for a tunnel. As air flow was increased to accelerate the smoke generation, combustion became more efficient and smoke production even decreased, although more fuel per unit time was consumed.

A commercially available smoke candle, shown in figure 49, was also tested. The item is sold primarily for use in leak detection in large duct systems. The chemical composition is proprietary, but chemical analysis suggests that it might be a hexachloroethane smoke similar to that used by the military for screening purposes and designated as HC (refs. 27 to 29). Among the expected products are $ZnCl_2$ and traces of HCl. The material is mildly toxic, and prolonged usage in the

[2] Pyrex: trademark of Corning Glass Works.

presence of some materials affected by acid should be avoided. The size distribution of the particles produced by the smoke candle was determined in the laboratory using the Knollenberg FSSP instrument. The results are shown in figure 50. Several samples were taken and some time-dependent variation in the size distribution was noted. The reason for this time dependence has not been determined. The size distribution is skewed to the desirable small-particle range to ensure rapid response to the flow. This was the only smoke tested which worked in the facility to provide acceptable pictures. (See fig. 51.) Four 1-minute candles (see fig. 49) were used to obtain the data. According to the manufacturer's specifications, each candle produces 8000 ft^3 of smoke. It is not known whether, once formed, any additional condensation occurs or is induced in passing through the nozzle, with the attendant deleterious effects of heat addition on flow variables. The material tends to leave a black, watery residue which can be wiped off. The biggest drawback is with controlling the smoke generation, which is quantized by the candle size. One attempt to solve this problem is illustrated in figure 52. Several candles held in the stand shown in figure 49 were ignited and introduced into the chamber through the access door on the bottom. Slight overpressure was noted by the slight bowing of the sidewalls. The chamber was connected to an exhaust port to simulate its coupling into the reduced-pressure diffuser in the facility. Another inlet solenoid could be actuated to vent the chamber. The scheme did not seem to work at all. The flow of air through the chamber was ineffective in entraining the smoke. It would appear that mixing vanes or perhaps a bellows arrangement are required to accomplish the desired objective.

A scaled-up commercial device similar to that pictured in figure 53 was also tried. Such a device would be ideal since it is switch-activated and it produces a nontoxic, reasonably dense aerosol (possibly polypropylene glycol). For this particular facility, the aerosol did not survive the round trip after having been introduced in the diffuser side of the circuit. One attempt was made to connect the device to the upstream settling chamber to no avail. The strong suction was incompatible with the heated nozzle configuration in the unit.

The aerosol problem has yet to be successfully resolved despite the obvious advantages, especially for low-speed regimes. Phosphorous-based materials would be suitable candidates for further testing (refs. 27 to 29).

Detection

High-quality 70-mm reflex cameras are currently used to record the data, thus providing excellent resolution and a large format. When used in the preferred mode, the camera is housed in a protective housing inside the test section as shown in figure 54. The housing is somewhat streamlined and encroaches upon the limit set for nonchoked flow in the facility (ref. 7). The obvious disadvantage of this data mode is that the equipment is inaccessible during a run in event of malfunction. Furthermore, the film processing defers the availability of data for at least a day.

Occasionally the processed film will show signs of electrical discharges. (See fig. 55.) This occurs despite the fact that the camera is grounded to the housing and the housing is mounted to the massive metal tunnel structure. Steps to ensure that the camera chamber doesn't become too dry (and thus subject to electrical discharges) must be taken even in the "wet" external environment of a vapor-screen run.

One attractive alternative to the present system involves using a periscope arrangement to relay the information from the test section. The advantages would include the following: (1) removing the camera to an accessible location to deal with malfunctions, replace film magazines, and so forth; (2) allowing use of alternative recording schemes such as video detectors, which would otherwise be difficult to place in the flow; (3) providing for alternative views, focus settings, or exposure times to accommodate test-condition changes; and (4) providing easier access to the image plane for adding identification labels and test information. The frontal area of the relay system head would be comparable to that used by the existing camera housing so as not to further choke the flow. The unavoidable loss in throughput could easily be compensated for by increasing the intensity of the light sheet.

A test was conducted using a periscope fabricated from salvaged optical components. Laboratory tests indicated that the system was 15 times less sensitive than the standard reflex camera operating at $f/2.8$. To evaluate the imaging quality, 1-sec exposures were required in lieu of the usual 1/8- to 1/4-sec settings. A 3-W Ar^+ laser provided the illumination. Figure 56 presents the views obtained with the periscope and side-mount cameras. The side-mount camera also benefits from the enhanced forward scattering. A well-designed relay system could be tailored to the reflex camera and provide speeds in the $f/4$ to $f/6$ range with little or no degradation in image quality.

Although we should mention the use of image processor technology statements regarding the state of the art are ephemeral in this rapidly advancing area. It is perhaps fair to say that engineers accustomed to seeing high-quality 70-mm-format images might be somewhat disappointed with the more common image processor output. A medium-resolution film can easily resolve 60 lines per millimeter, or $60 \times 70 = 4200$ lines across the image field. In television (TV) parlance, a black line and its adjacent white space are separately counted as "lines;" therefore, our film example would correspond

to 8400 "TV lines." A standard vidicon operating at a scan rate of 525 could approach a resolution of 400 TV lines and a high-resolution TV tube at higher scan rates might approach 800 to 1000 TV lines.

A second consideration in digitally acquired imagery is its handling. Digital images are attractive from the standpoint of further computer manipulation and it is possible to "frame grab" at rates of 30 Hz, but if the data are to be stored on some serial medium, then an allowance must be made for transferral. For example, 1024×1024 pixels with 256 gray-scale resolution represents 8.4 million bits of information. A tape with 1600 bits per inch (8 bits across the tape) moving at 45 in/sec would require 15 sec to transfer a single image. In practice, a 2400-ft tape could hold the 50 images of a single film magazine. At some point, hardcopy of the video images is desirable. Display on and photography of monitors can result in considerable distortion. The higher fidelity slow-scan equipment is quite expensive. To assess the merits of image processing for a particular field application, it would be advisable to carry high-quality film records to an image processing laboratory. The handling and manipulation of images could be exercised with actual data and the output assessed prior to committal of funds.

Conclusions

The vapor-screen technique is useful for visualizing vortex structure in fluid mechanics. It is based on classic Mie scattering theory. Its effective implementation requires an intense, collimated light source, uniform entrainment of light-scattering centers, and a suitable image detection scheme (usually film cameras). High-pressure mercury-capillary lamps and lasers were evaluated as light sources. Air-cooled 1-kW lamps are normally used in the facility under consideration and served as comparison standards for the alternative illumination schemes. Attempts to more efficiently collect and use the energy from these (1 kW) sources as well as methods to increase energy input with pulsed circuitry were only partially successful. Gains in light output were offset by added complexity and decreased reliability. Water-cooled 4-kW lamps in tandem with low f-number Fresnel lenses provided substantial improvement in throughput and reasonably high-quality images. Customized lens design could improve the image quality, although chromatic aberrations would persist. For some large-scale applications, the Fresnel-lens-based system could offer distinct advantages. The 3-W Ar^+ laser provided the easiest solution to the lighting problem, since the collimation is inherent and only needs to be "spoiled" in one dimension to form the screen. High-power lasers have become fairly robust and, with suitable care, can operate in a facility environment. The rather cumbersome optical head with its attendant cooling and power requirements could be remotely stationed and the beam routed to the test section of interest.

Uniform entrainment of light-scattering centers is probably the toughest problem for large-scale facilities. Condensation becomes less reliable in the lower Mach number regime. The use of injected aerosols is fraught with engineering problems. It is difficult to inject large volumes of smoke into a wind tunnel circuit in controlled amounts. Presently, a dew-point-controlled feedback system to inject water into the circuit coupled with an empirically determined operating curve offers the best reliability while other methods are investigated.

A retractable periscope to transfer the image from the flow axis to an external station would offer advantages over the current method for recording the data. The relayed image could be recorded with reflex cameras to provide high-quality data. Cameras would be accessible during the run for setting changes or replacement in case of malfunction. Moreover, alternative solid-state or video approaches to image recording could be investigated with a minimum effort.

Langley Research Center
National Aeronautics and Space Administration
Hampton, VA 23665
July 11, 1984

References

1. Maltby, R. L., compiler: *Flow Visualization in Wind Tunnels Using Indicators.* AGARDograph 70, Apr. 1962.
2. Merzkirch, Wolfgang: *Flow Visualization.* Academic Press, Inc., 1974.
3. Wegener, Peter P., ed.: *Nonequilibrium Flows—Part I.* Marcel Dekker, Inc., c.1969.
4. Wegener, P. P.; and Mack, L. M.: Condensation in Supersonic and Hypersonic Wind Tunnels. *Advances in Applied Mechanics,* Volume V, H. L. Dryden and Th. von Kármán, eds., Academic Press, Inc., 1958, pp. 307–447.
5. McGregor, I.: The Vapour-Screen Method of Flow Visualization. *J. Fluid Mech.,* vol. 11, pt. 4, Dec. 1961, pp. 481–511.
6. Nietubicz, Charles J.: *Vapor Screen Technique Development at the Ballistic Research Laboratories.* BRL Memo. Rep. No. 2387, U.S. Army, June 1974. (Available from DTIC as AD 784 077.)
7. Jackson, Charlie M., Jr.; Corlett, William A.; and Monta, William J.: *Description and Calibration of the Langley Unitary Plan Wind Tunnel.* NASA TP-1905, 1981.
8. Mihalas, Dimitri: *Stellar Atmospheres.* W. H. Freeman & Co., c.1970.
9. Thomas, Woodlief, Jr., ed.: *SPSE Handbook of Photographic Science and Engineering.* John Wiley & Sons,

Inc., c.1973.

10. Vanderwerf, Dennis: Approximating the Fresnel Lens. *Electro-Opt. Syst. Design,* vol. 14, no. 2, Feb. 1982, pp. 47–51.
11. Delano, Erwin: Primary Aberrations of Fresnel Lenses. *J. Opt. Soc. America,* vol. 64, no. 4, Apr. 1974, pp. 459–468.
12. Delano, Erwin: Primary Aberration Contributions for Curved Fresnel Surfaces. *J. Opt. Soc. America,* vol. 68, no. 10, Oct. 1978, pp. 1306–1309.
13. Philbert, Michel; Beaupoil, Robert; and Faleni, Jean-Pierre: *Application of a Laminar Lighting Device to the Smoke Visualization of Flows in a Wind Tunnel.* ESA-TT-609, Jan. 1980, pp. 25–33.
14. Dowley, M. W.: Reliability and Commercial Lasers. *Appl. Opt.,* vol. 21, no. 10, May 15, 1982, pp. 1791–1795.
15. Van de Hulst, H. C.: Light Scattering by Small Particles. Dover Publ., Inc., c.1981.
16. Wickramasinghe, N. C.: *Light Scattering Functions for Small Particles With Applications in Astronomy.* John Wiley & Sons, Inc., c.1973.
17. Knollenberg, Robert G.: Single Particle Light Scattering Spectrometers. *Aerosol Measurement,* Dale A. Lundgren, Franklin S. Harris, Jr., William H. Marlow, Morton Lippmann, William E. Clark, and Michael D. Durham, eds., Univ. Presses of Florida, c.1979, pp. 271–293.
18. Hansen, C. Frederick; and Nothwang, George J.: *Condensation of Air in Supersonic Wind Tunnels and Its Effects on Flow About Models.* NACA TN-2690, 1952.
19. Stevenson, Warren H.; dos Santos, Reginaldo; and Mettler, Stephen C.: Fringe Mode Fluorescence Velocimetry. *Applications of Non-Intrusive Instrumentation in Fluid Flow Research,* AGARD-CP-193, Sept. 1976, pp. 20-1–20-9.
20. McNulty, Peter J.; and Chew, Herman W.: *Fluorescent Scattering by Molecules Embedded in Small Particles—Comprehensive Report 1977–1980.* Contract EE-77-S-02-4361, Clarkson College of Technol., 1980.
21. Kerker, Milton: *Fluorescence and Light Scattering of Aerosol Particles.* Contract DRXRO-CB-15703-C, Clarkson College of Technol., July 1982. (Available from DTIC as AD A118 273.)
22. Morsi, S. A.; and Alexander, A. J.: An Investigation of Particle Trajectories in Two-Phase Flow Systems. *J. Fluid Mech.*, vol. 55, pt. 2, Sept. 1972, pp. 193–208.
23. Gartrell, Luther R.; and Rhodes, David B.: *A Scanning Laser-Velocimeter Technique for Measuring Two-Dimensional Wake-Vortex Velocity Distributions.* NASA TP-1661, 1980.
24. Griffin, O. M.; and Ramberg, S. E.: Wind Tunnel Flow Visualization With Liquid Particle Aerosols. *Flow Visualization,* Tsuyoshi Asanuma, ed., Hemisphere Pub. Corp., c.1979, pp. 65–73.
25. Griffin, O. M.; and Votaw, C. W.: The Use of Aerosols for the Visualization of Flow Phenomena. *Int. J. Heat & Mass Transfer,* vol. 16, no. 1, Jan. 1973, pp. 217–219.
26. Yu, J. P.; Sparrow, E. M.; and Eckert, E. R. G.: A Smoke Generator for Use in Fluid Flow Visualization. *Int. J. Heat & Mass Transfer,* vol. 15, no. 3, Mar. 1972, pp. 557–558.
27. *Engineering Design Handbook—Military Pyrotechnics Series, Part One—Theory and Application.* AMCP 706-185, U.S. Army Materiel Command, Apr. 1967.
28. *Engineering Design Handbook—Military Pyrotechnics Series, Part Two—Safety, Procedures and Glossary.* AMCP 706-186, U.S. Army Materiel Command, Oct. 1963.
29. *Engineering Design Handbook—Military Pyrotechnics Series, Part Three—Properties of Materials Used in Pyrotechnic Compositions.* AMCP 706-187, U.S. Army Materiel Command, Oct. 1963.

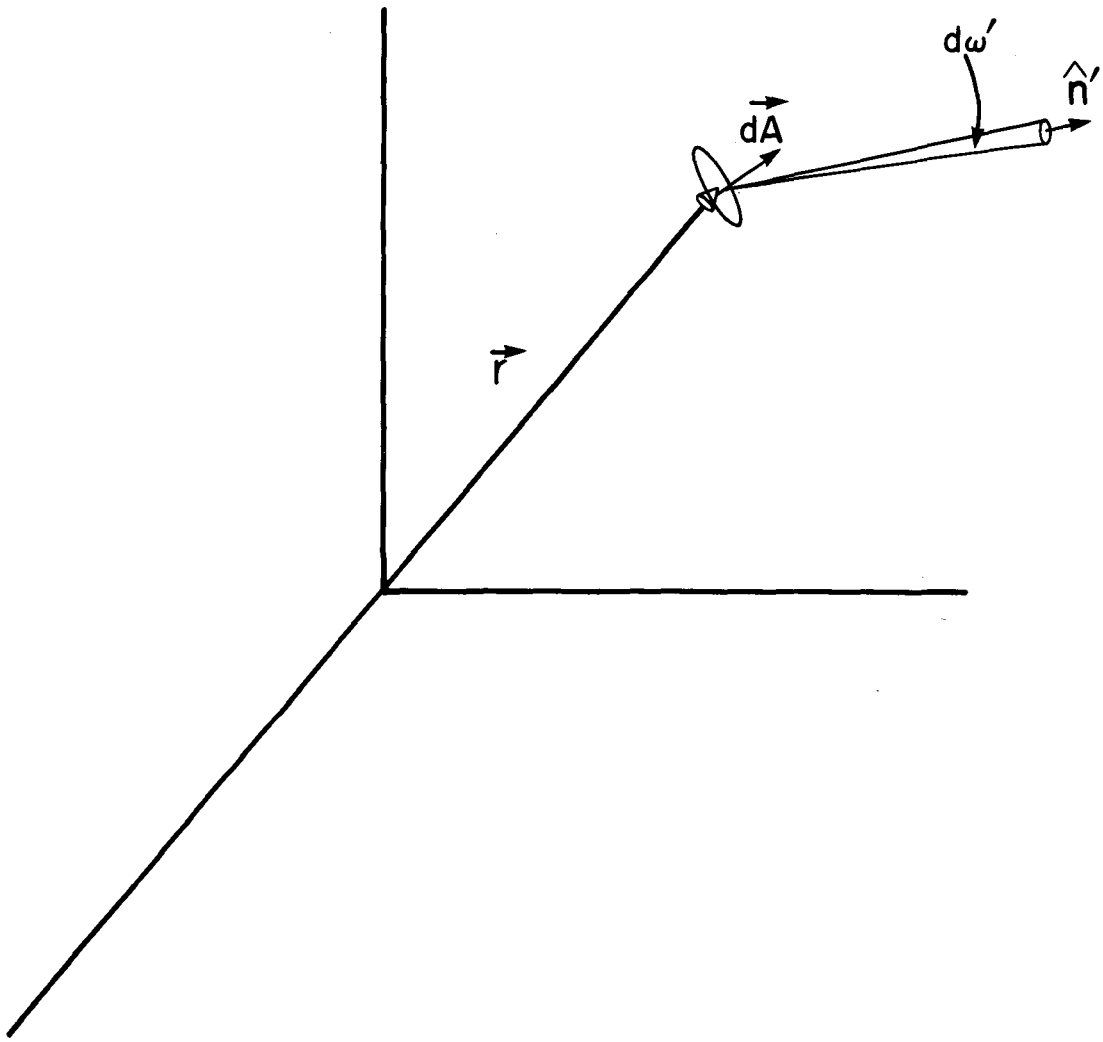

Figure 1. Geometry used to define intensity.

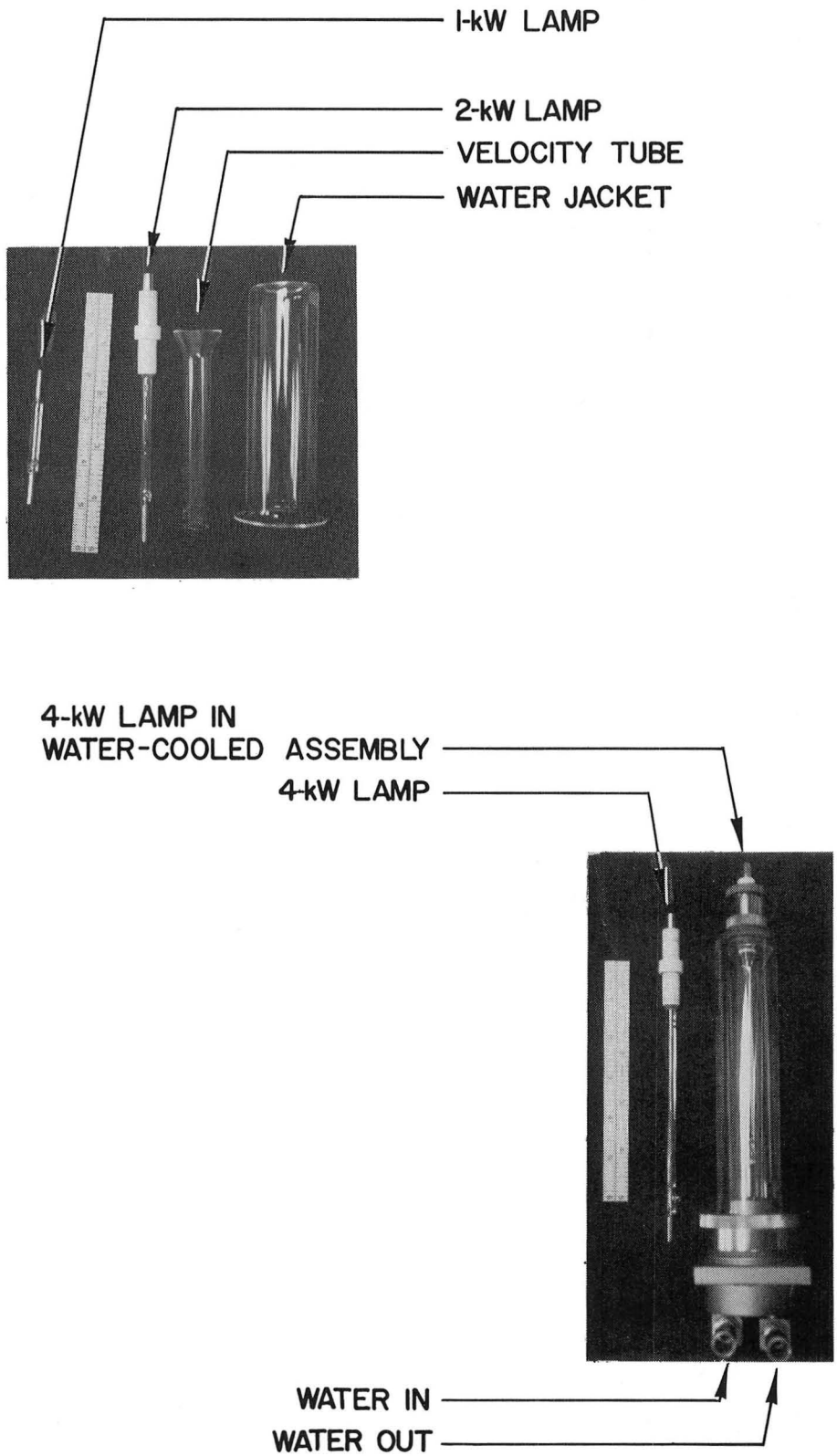

Figure 2. Examples of mercury-capillary lamps.

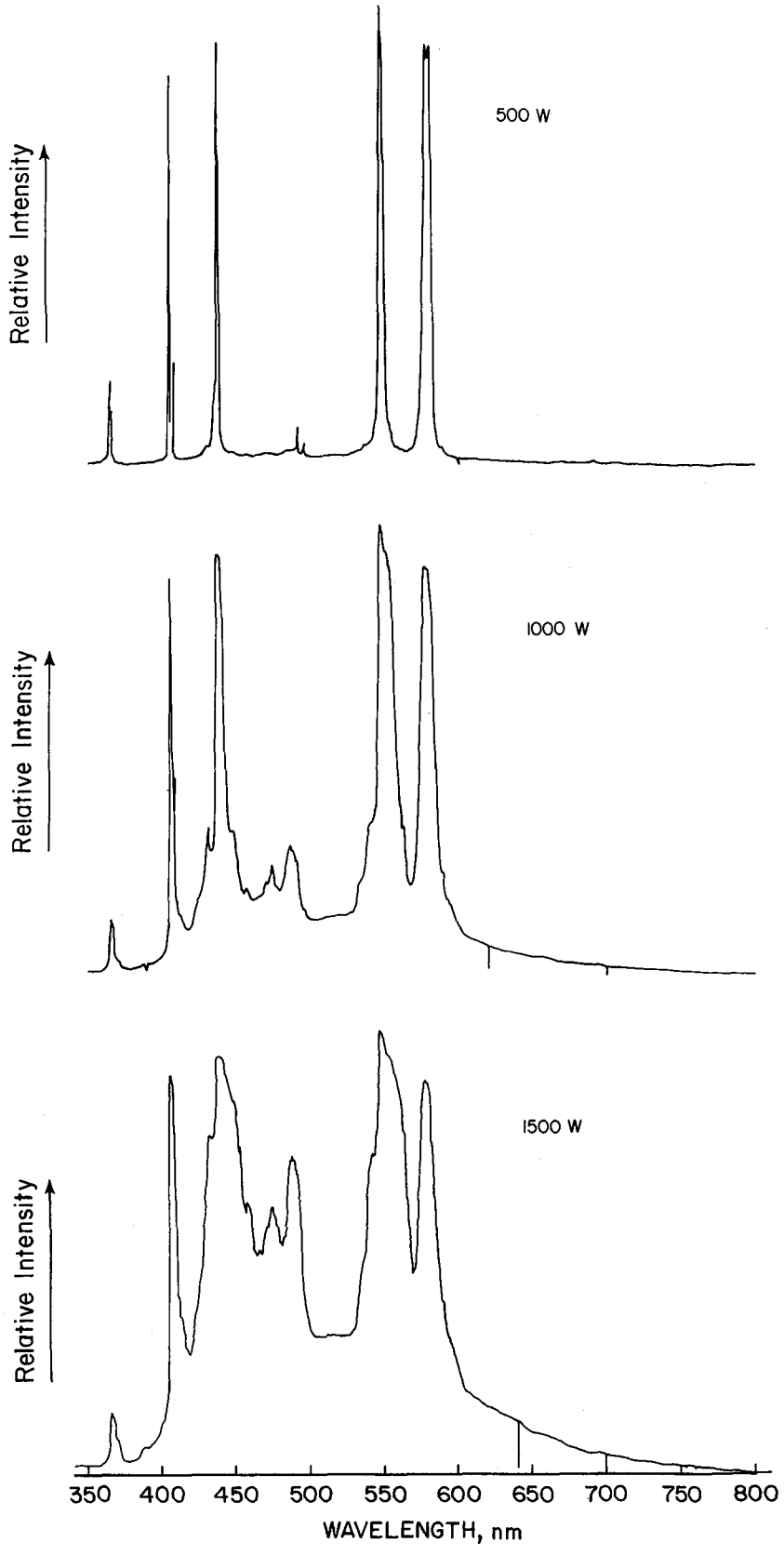

Figure 3. Effect of pressure on discrete spectral output as electrical input power is increased.

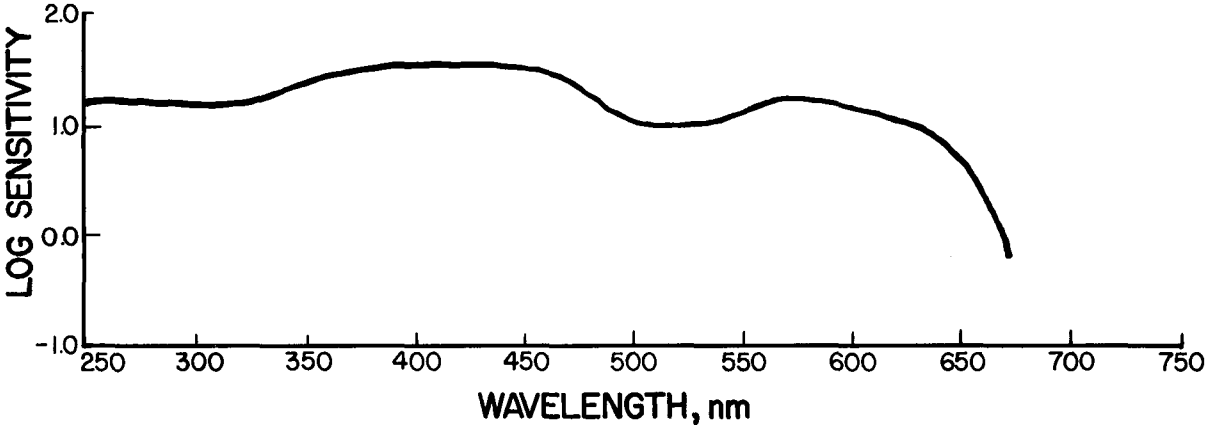

Figure 4. Spectral sensitivity of Kodak Tri-X Pan Film.

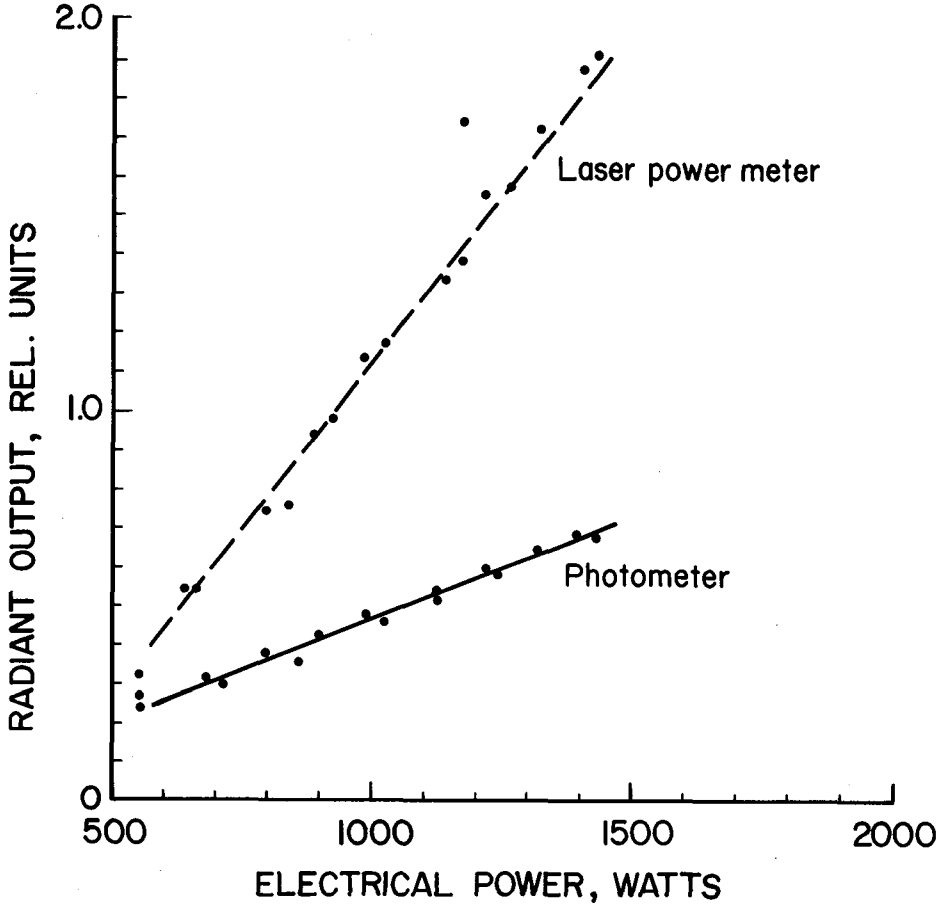

Figure 5. Radiant power as measured with filtered photometer and with laser power meter.

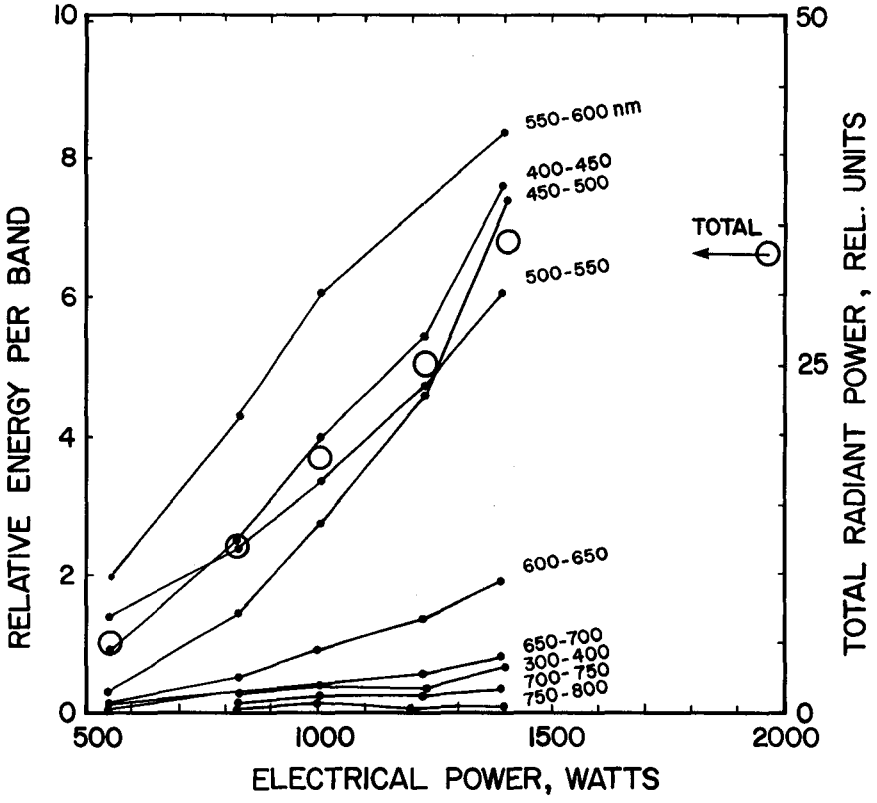

Figure 6. Radiant power in selected spectral bands measured with spectrometer. Open circles represent total radiant power in the 300- to 800-nm range.

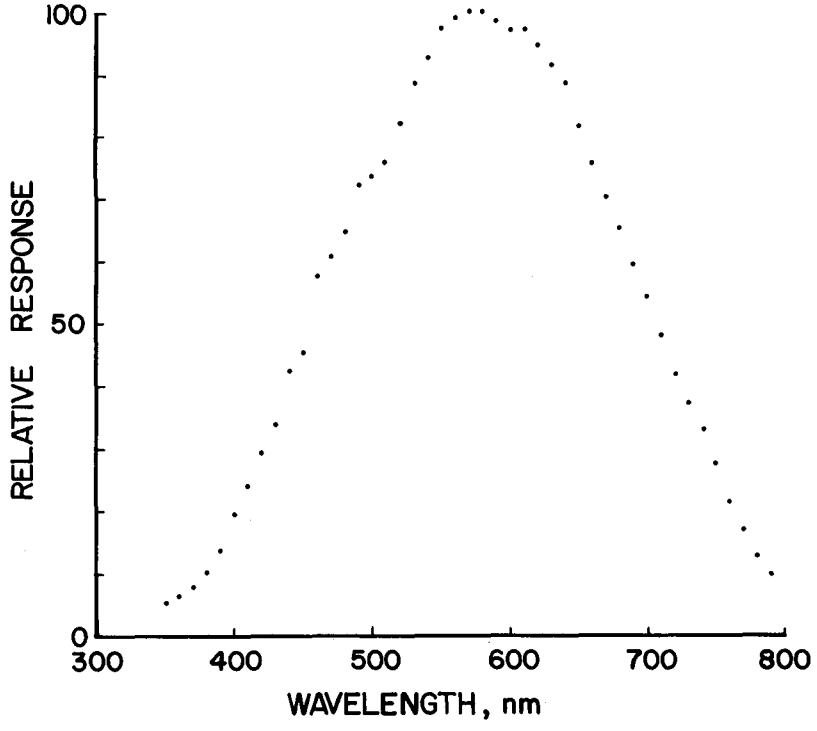

Figure 7. Response of spectrometer used to acquire data of figure 6.

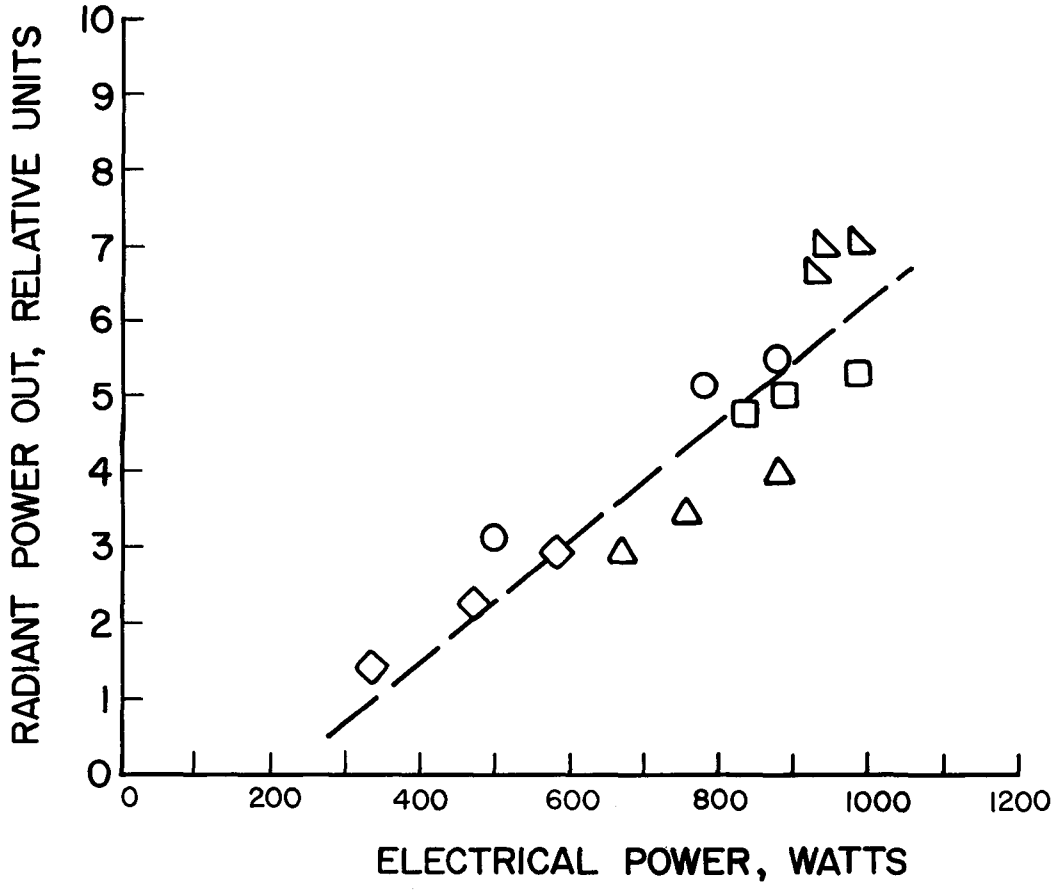

Figure 8. Photographically deduced (using Kodak Tri-X Pan Film) radiant power as a function of electrical power to lamp. Five independent data sets are represented by different symbols.

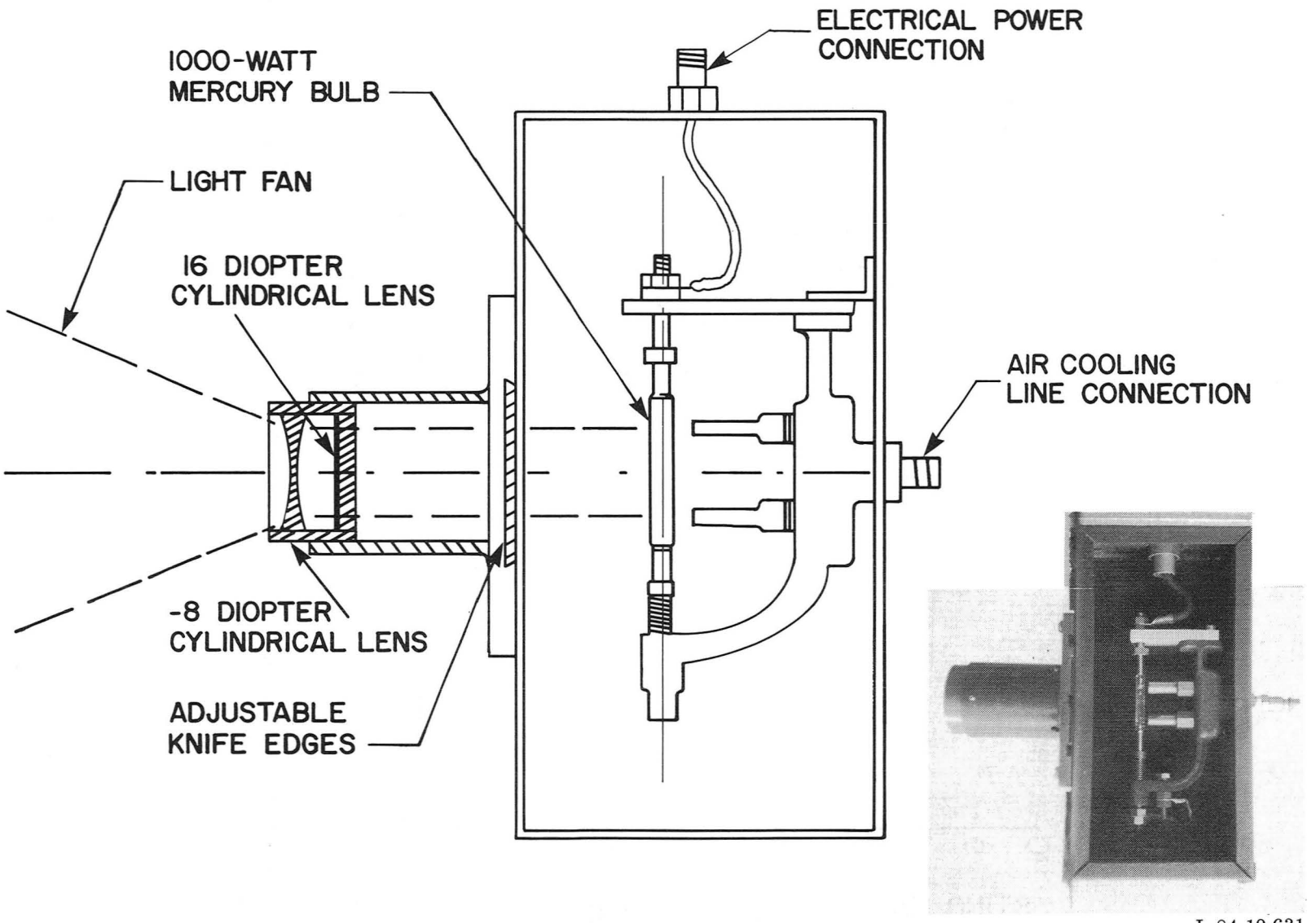

L-84-10,631

Figure 9. Housing for air-cooled, 1-kW lamp.

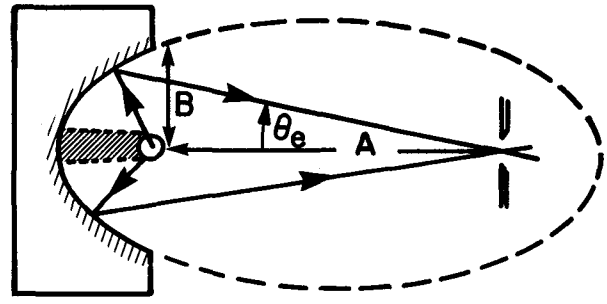

Figure 10. Schematic showing concept of ellipsoidal mirror to collect energy from capillary source.

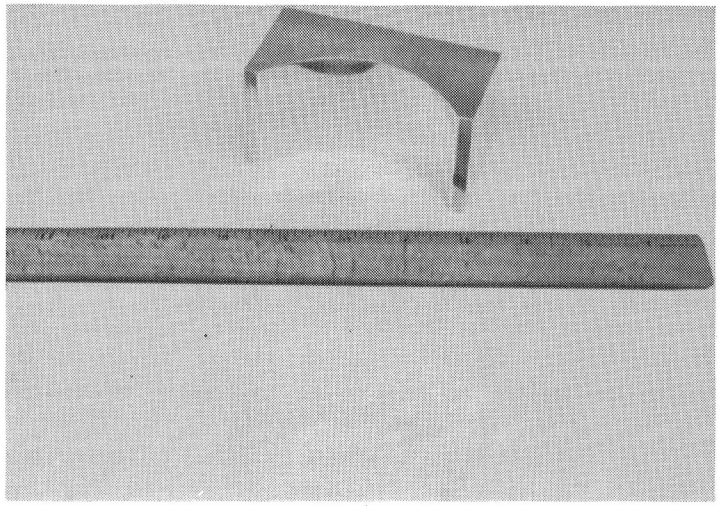

(a) Hand-polished collector.

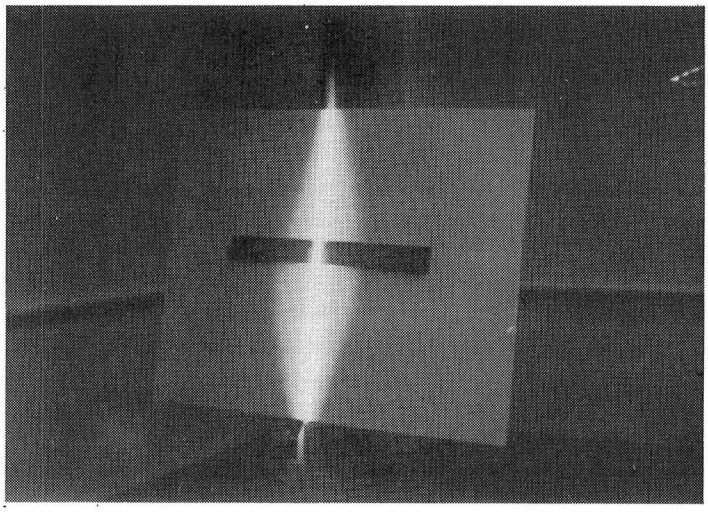

(b) Overexposed image of light beam to accentuate bloom.

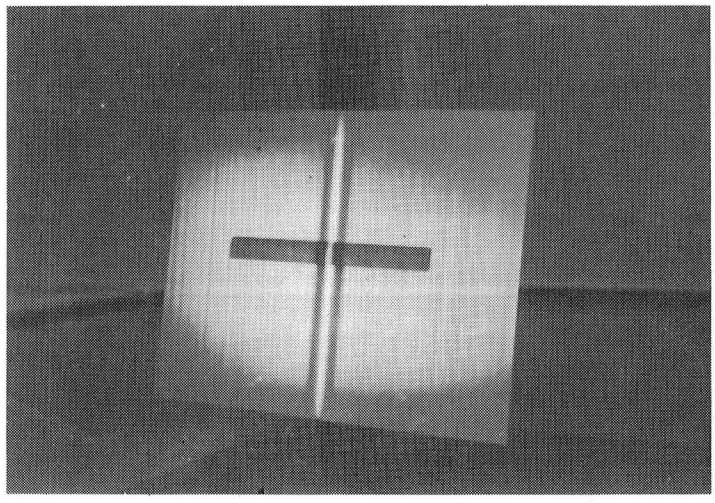

(c) Defocused image to show machining marks.

L-84-10,632

Figure 11. Ellipsoidal mirror used to increase light output of 1-kW air-cooled lamp.

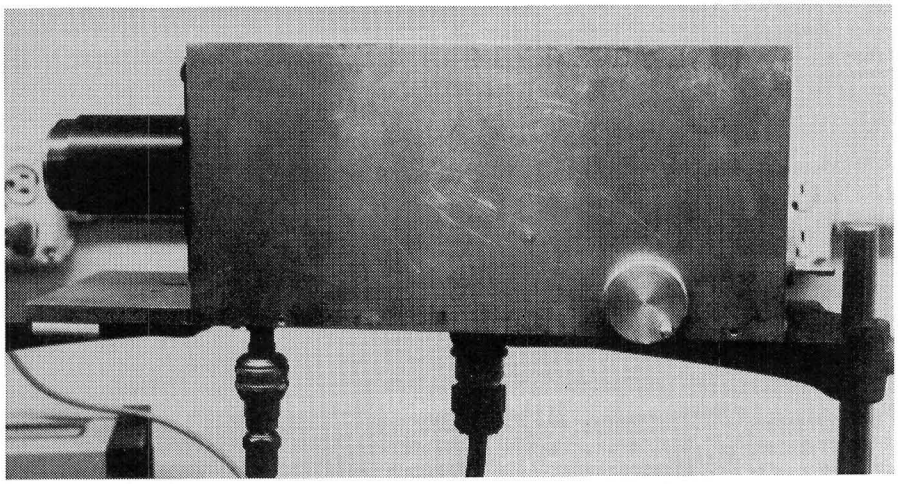

(a) Side view with cover on.

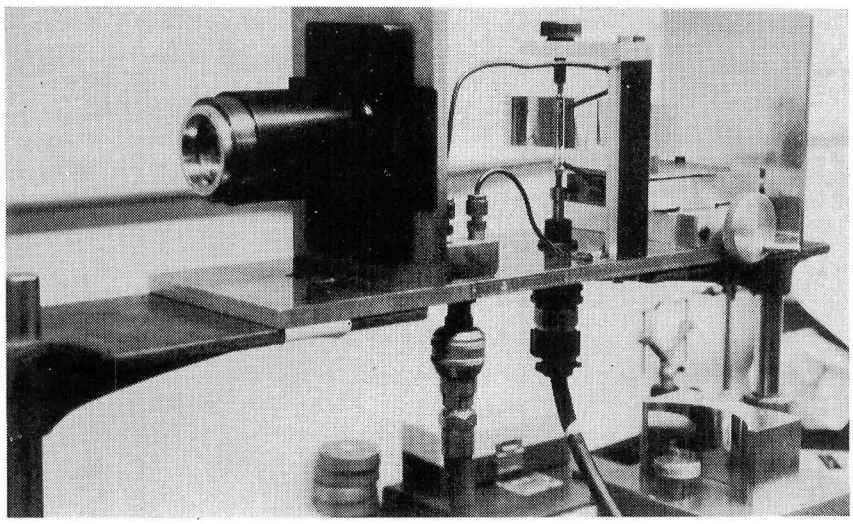

(b) Cover removed to show lamp at focus of ellipse.

L-84-10,633

Figure 12. Housing to accommodate ellipsoidal collector mirror.

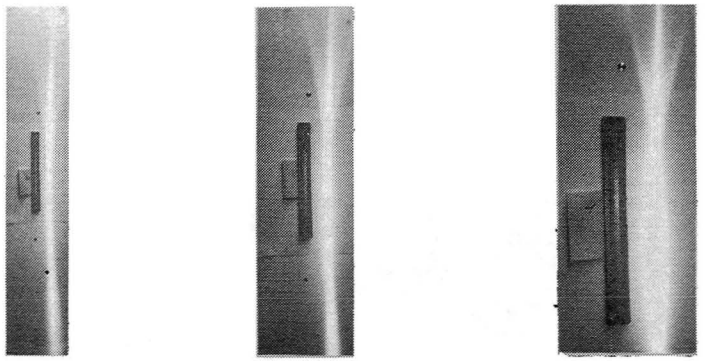

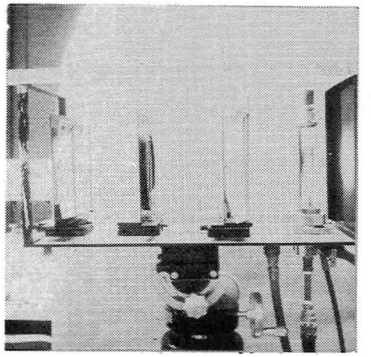

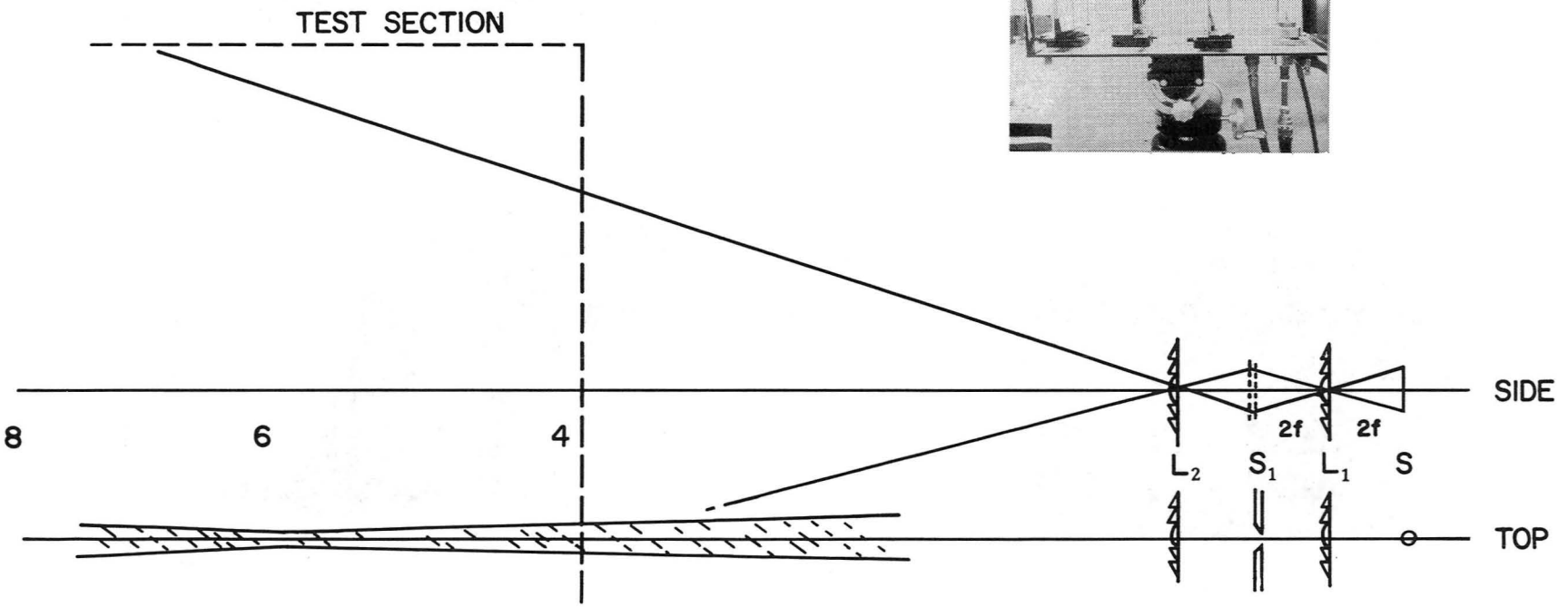

L-84-10,634

Figure 13. Prototype source with 4-kW water-cooled lamp and Fresnel collection optics. Overexposed photographs of the irradiance profiles are inset to show aberrations. Dimensions are in feet.

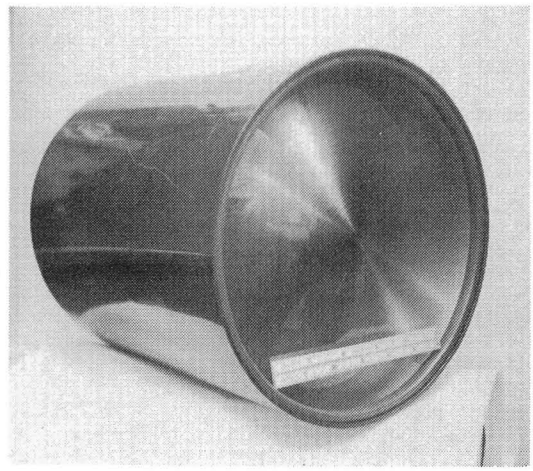

L-84-10,635

Figure 14. Doublet used as optical component in 4-kW lamp assembly.

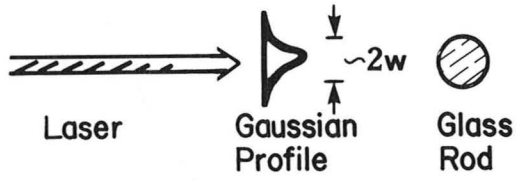

(a) Gaussian beam incident on cylindrical rod.

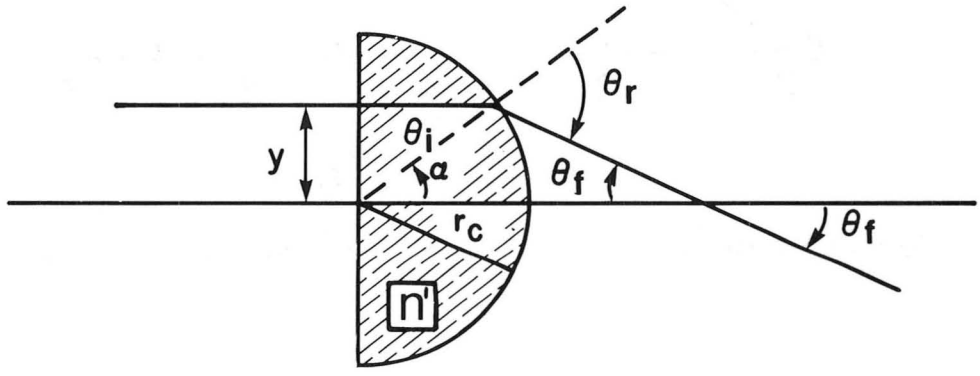

(b) Variables used to trace ray at height y through plane-cylindrical lens.

Figure 15. Method for fanning laser beam.

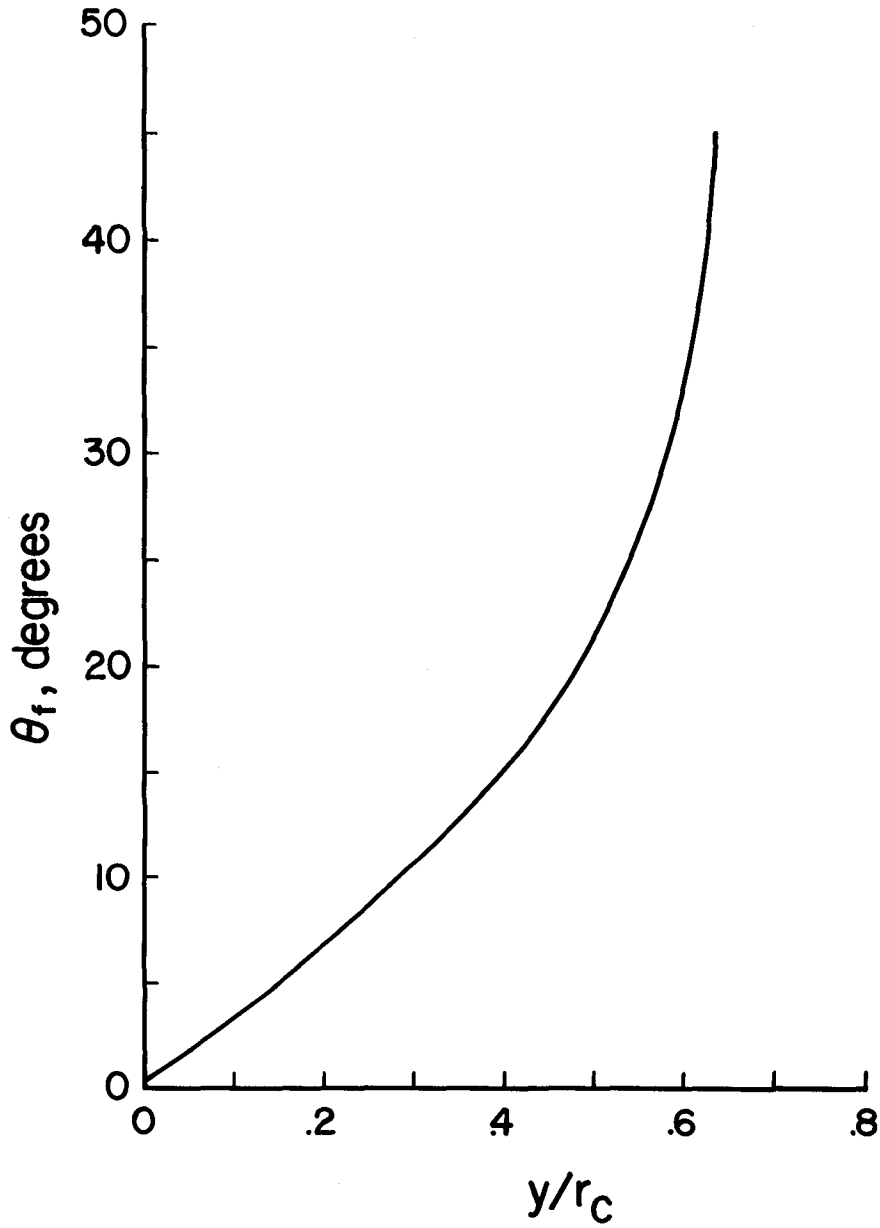

Figure 16. Fan angle as a function of dimensionless incidence height. $n' = 1.55$.

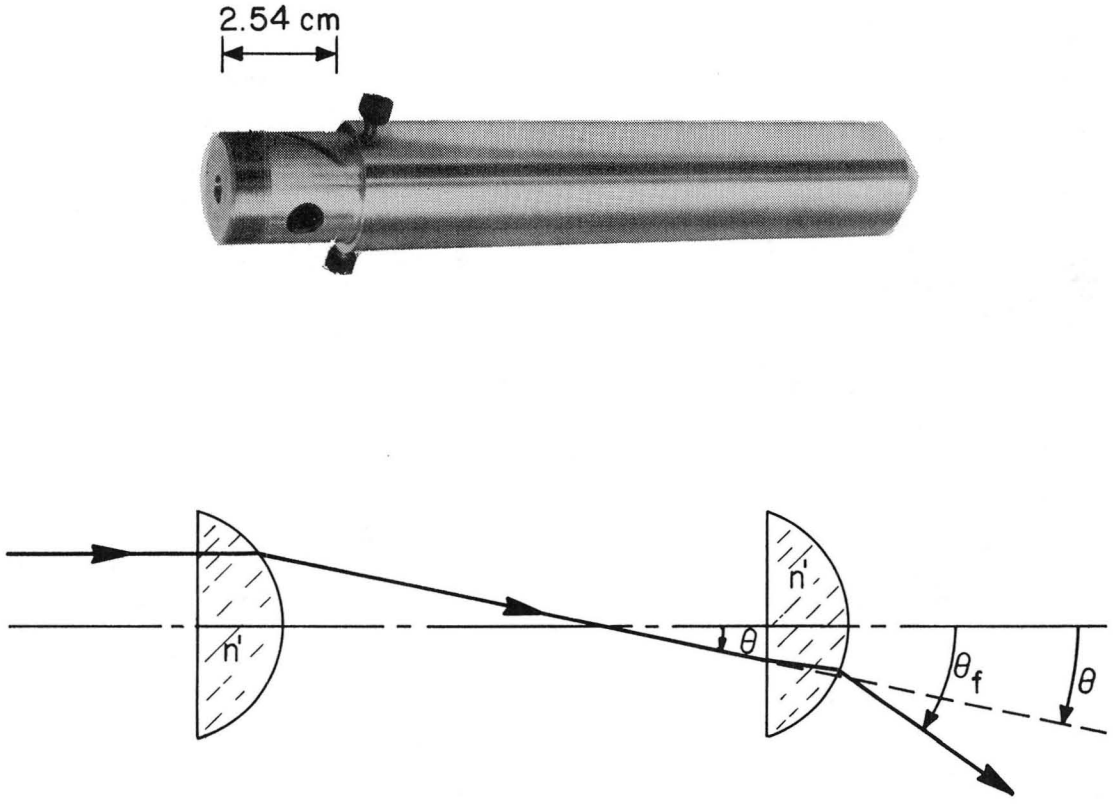

L-84-10,636

Figure 17. Telescoping fanning module.

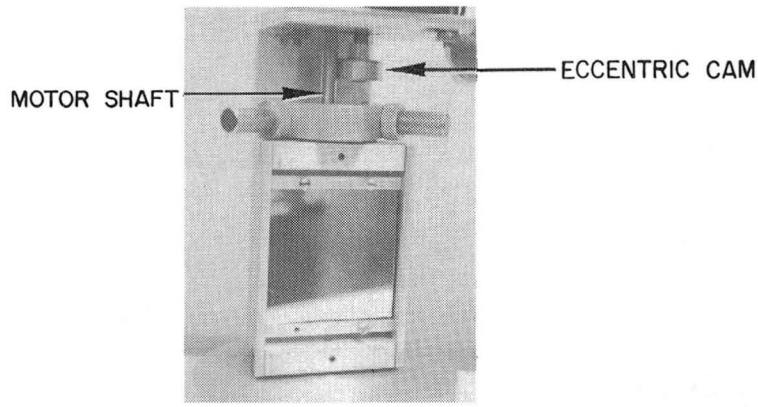

(a) Laser beam scanned by reflecting it from mirror rocked by eccentric cam.

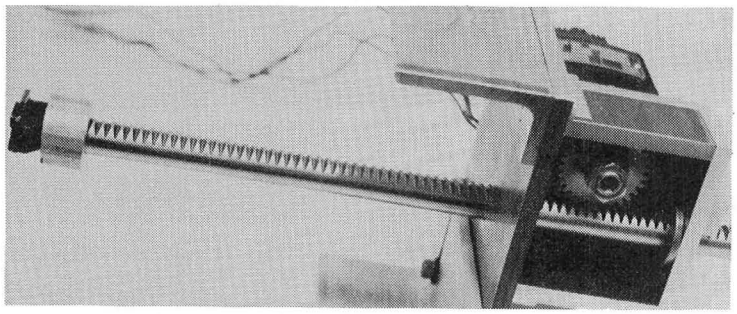

(b) Rack and pinion arrangement to translate laser beam.

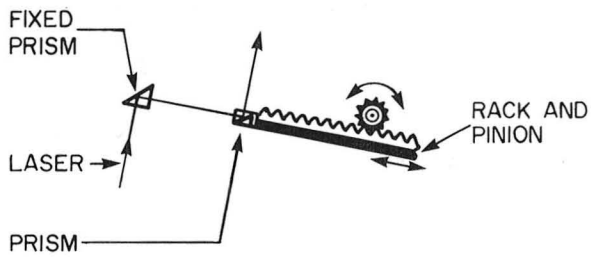

(c) Schematic of rack and pinion arrangement.

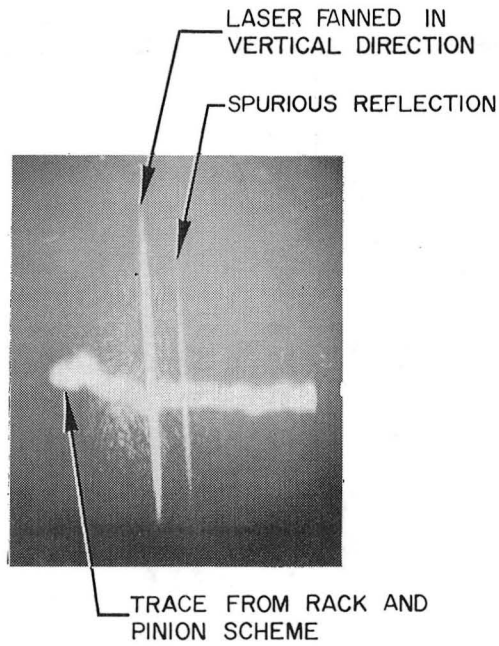

(d) Irradiance obtained using rack and pinion device compared with fanned laser image. Images recorded at right angles to avoid overlap.

L-84-10,637

Figure 18. Beam scanning techniques.

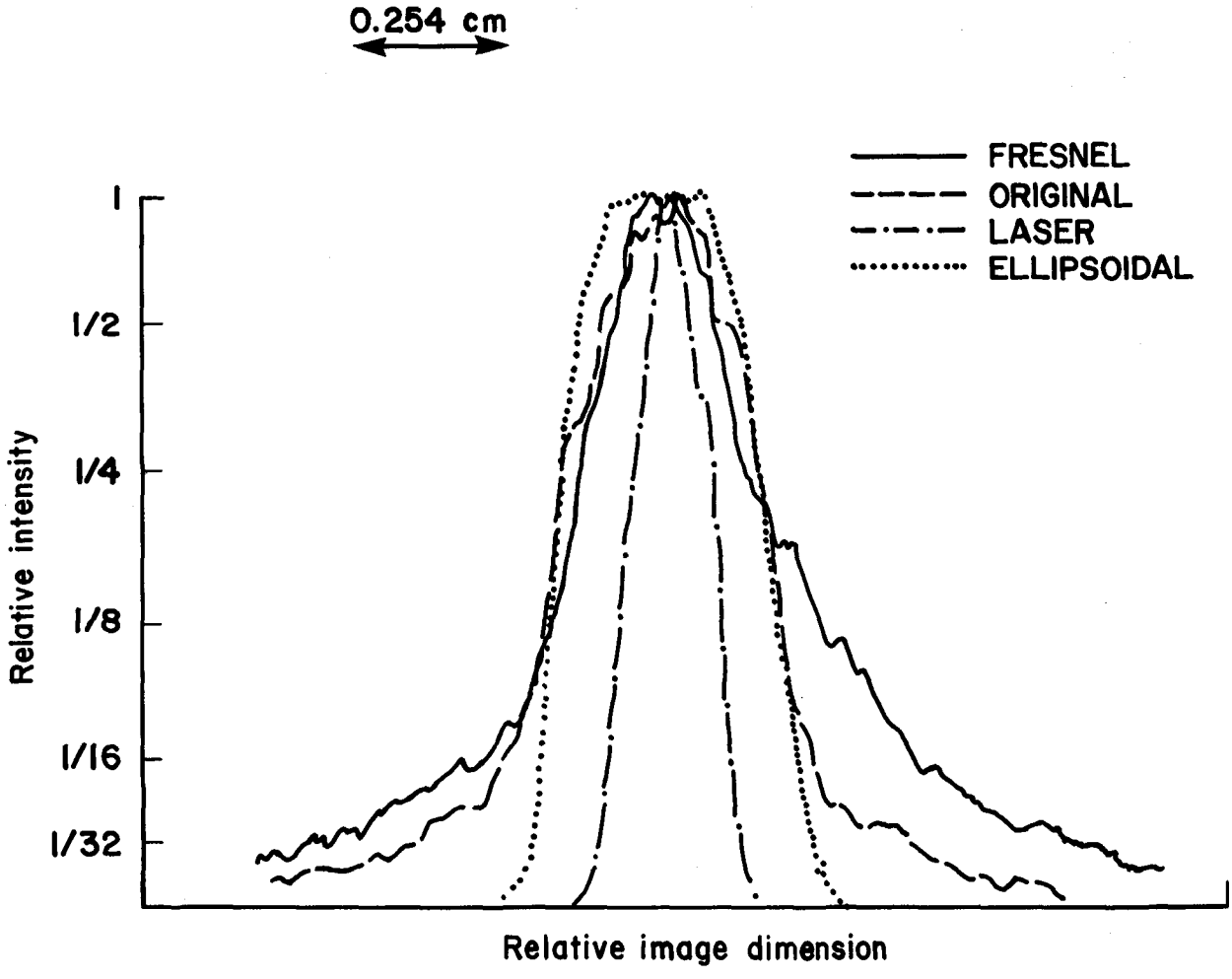

Figure 19. Normalized irradiance profiles for the sources studied.

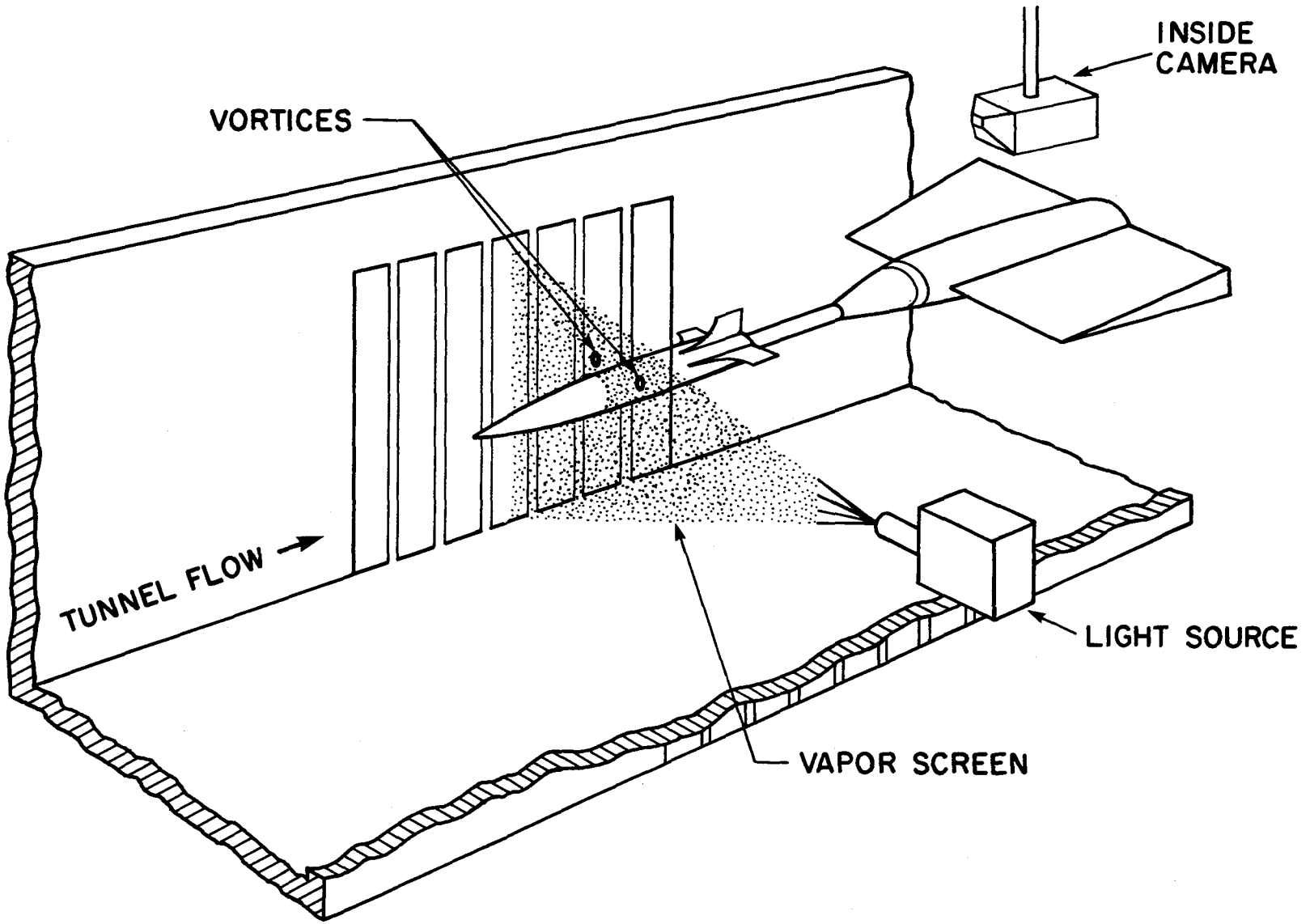

(a) Perspective view to show concept.

Figure 20. Vapor screen implementation in Langley Unitary Plan Wind Tunnel.

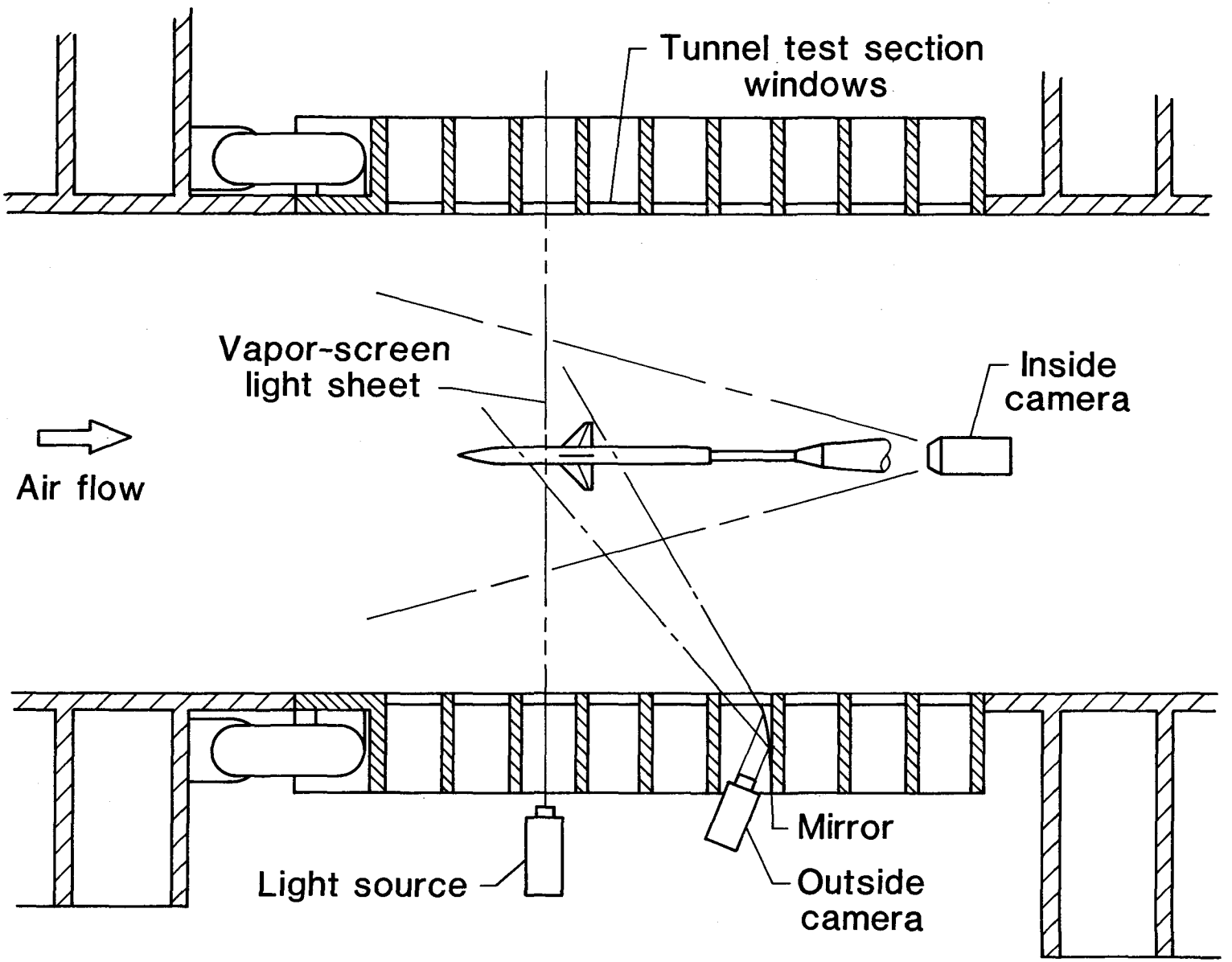

(b) Plan view to illustrate use of auxiliary side-mount camera.

Figure 20. Concluded.

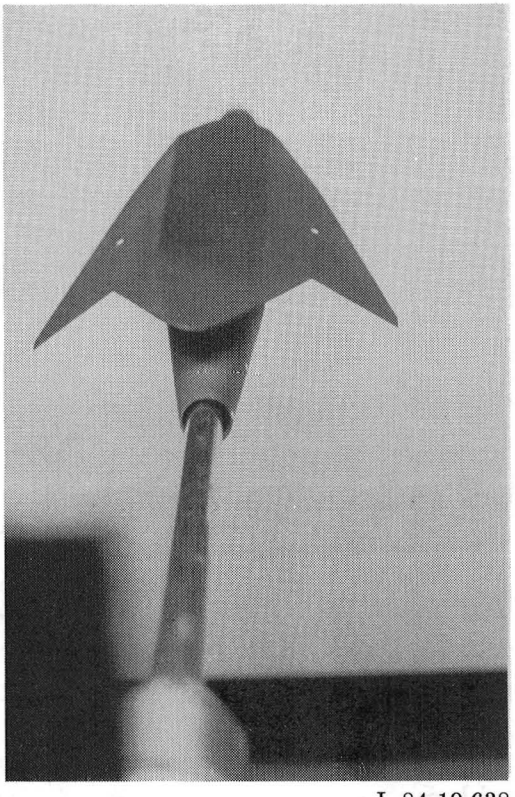

L-84-10,638

Figure 21. Model used to compare vapor screens.

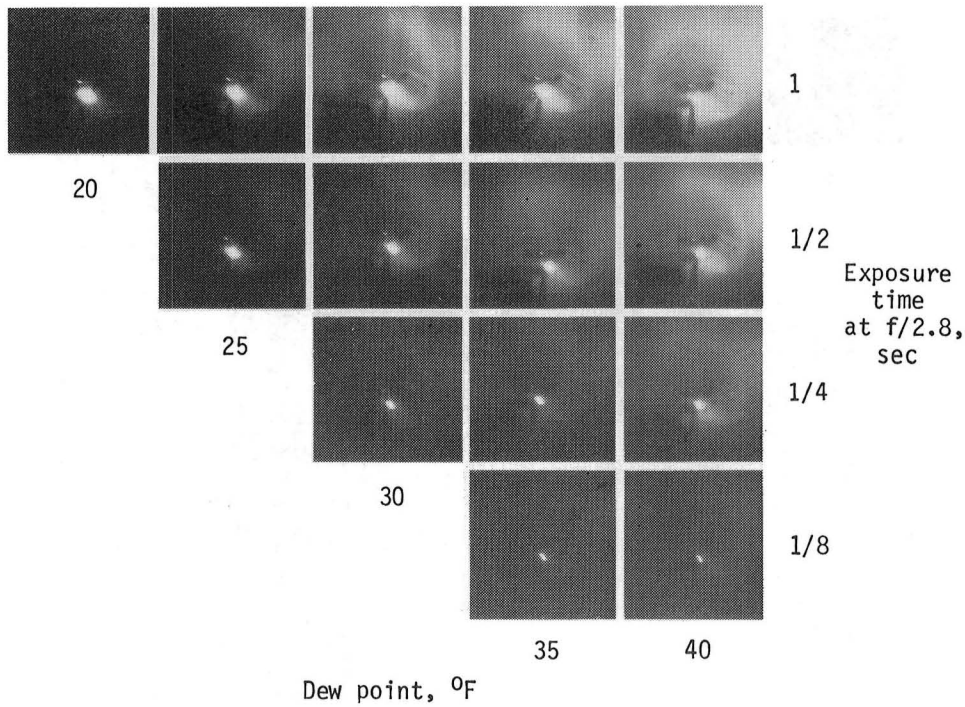

(a) Inside camera.

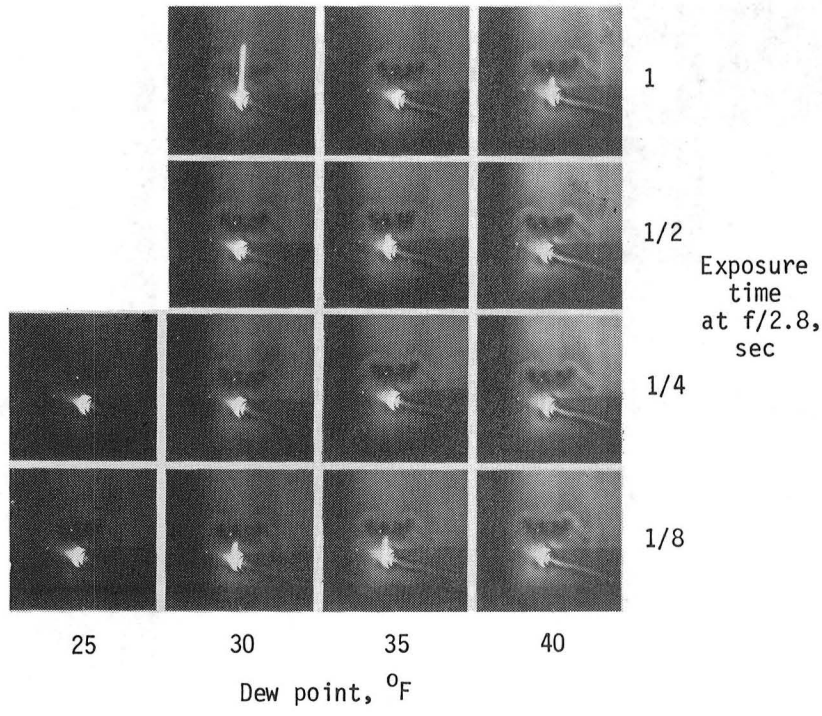

(b) Side-mount camera.

Figure 22. Exposure time versus dew point for conventional lighting arrangement.

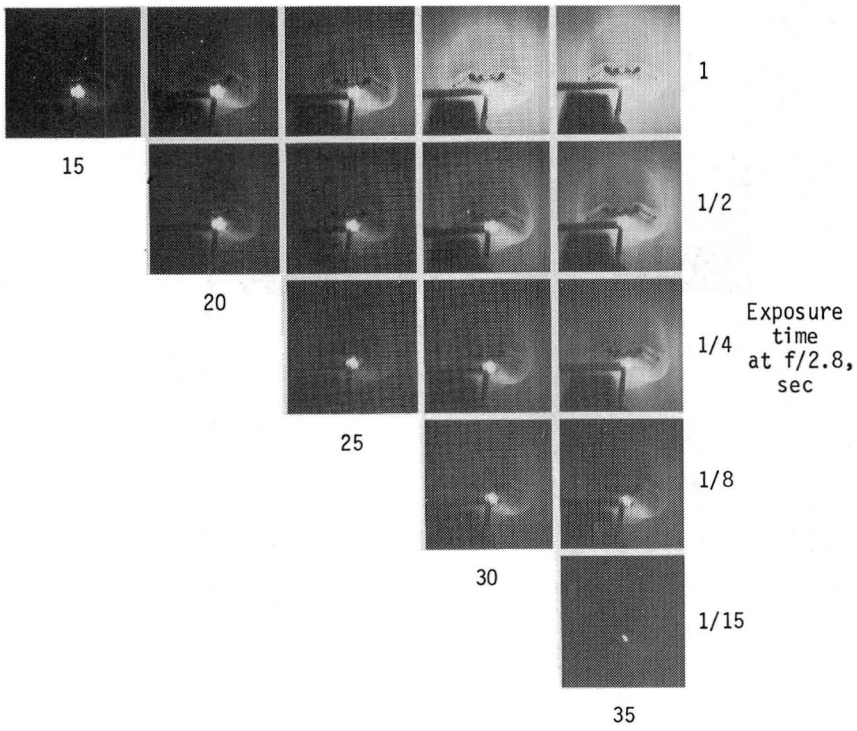

(a) Inside camera.

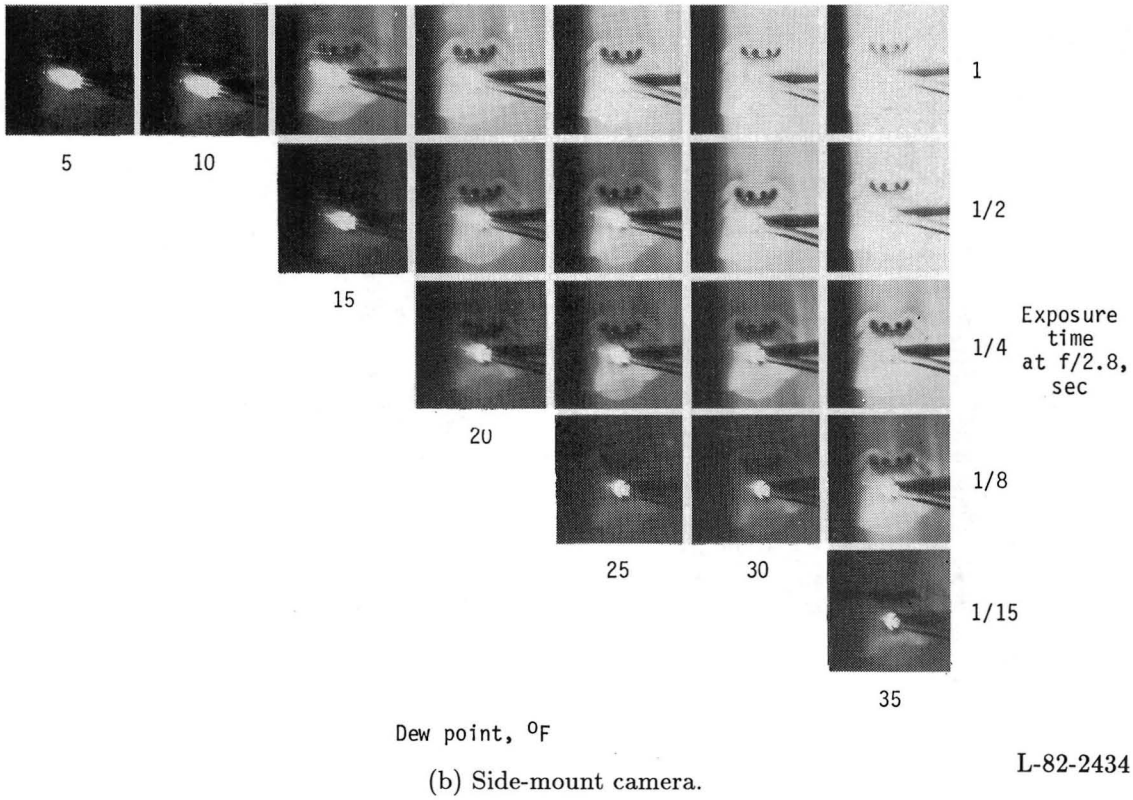

(b) Side-mount camera.

Figure 23. Exposure time versus dew point for Fresnel-based prototype system. The power supply did not allow operating lamp at its full 4-kW rating.

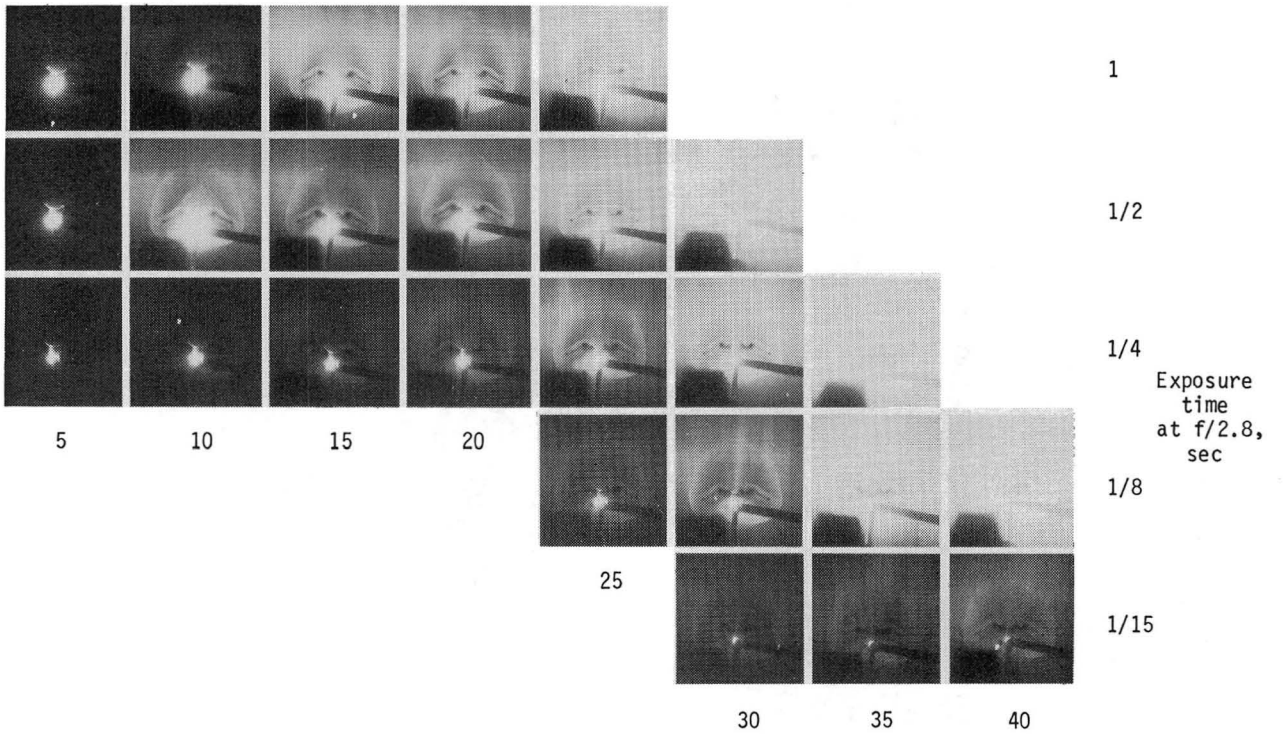

(a) Inside camera.

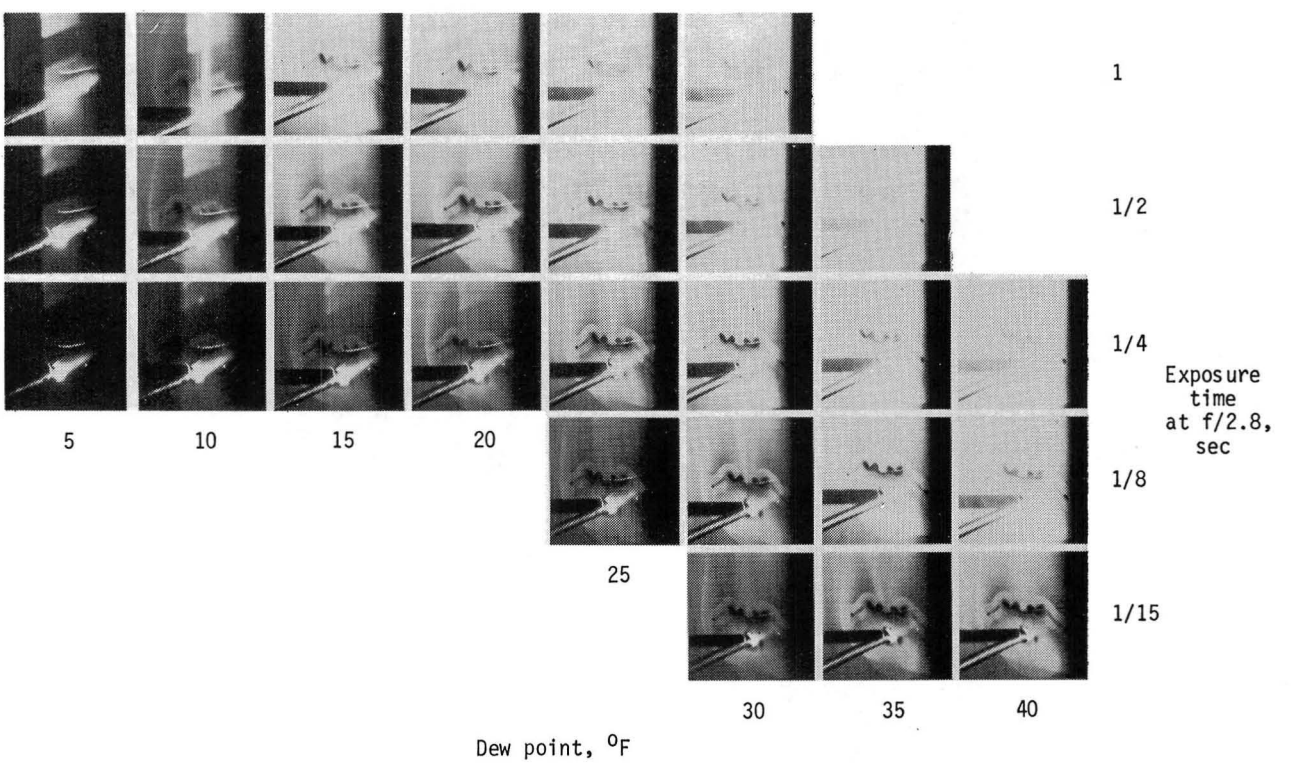

(b) Side-mount camera.

Figure 24. Exposure time versus dew point for Ar^+ laser operating at 3 W with "all lines" mirror.

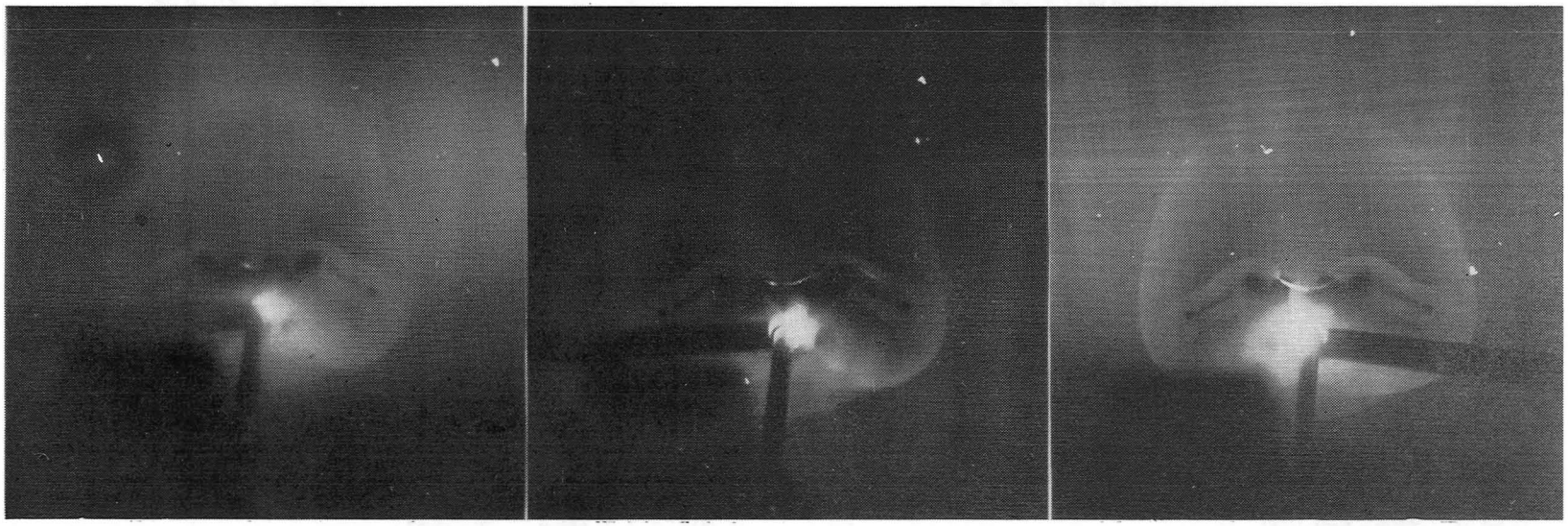

Twin 1-kW air-cooled capillary, 40°F dew point

Fresnel (3-kW) prototype, 25°F dew point

Fanned 25°F dew point

L-82-2436

Figure 25. Comparison of vapor-screen photographs from three different light schemes. Exposure time was 1/4 sec for each.

L-84-10,639

Figure 26. Results for original system (twin 1-kW lamps, at 40°F dew point and 1/4-sec exposure). Contrast was enhanced in printing.

L-84-10,640

Figure 27. Results for Fresnel prototype system (3-kW lamp) at 25°F dew point and 1/4-sec exposure. Contrast was enhanced in printing.

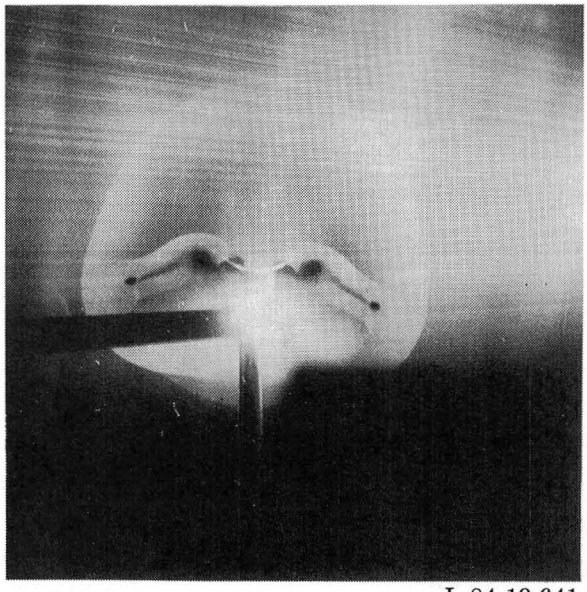

L-84-10,641

Figure 28. Results for Ar^+ laser system (3 W) at 25°F dew point and 1/4-sec exposure. Striations are due to imperfections in glass rod used to fan beam. Contrast was enhanced in printing.

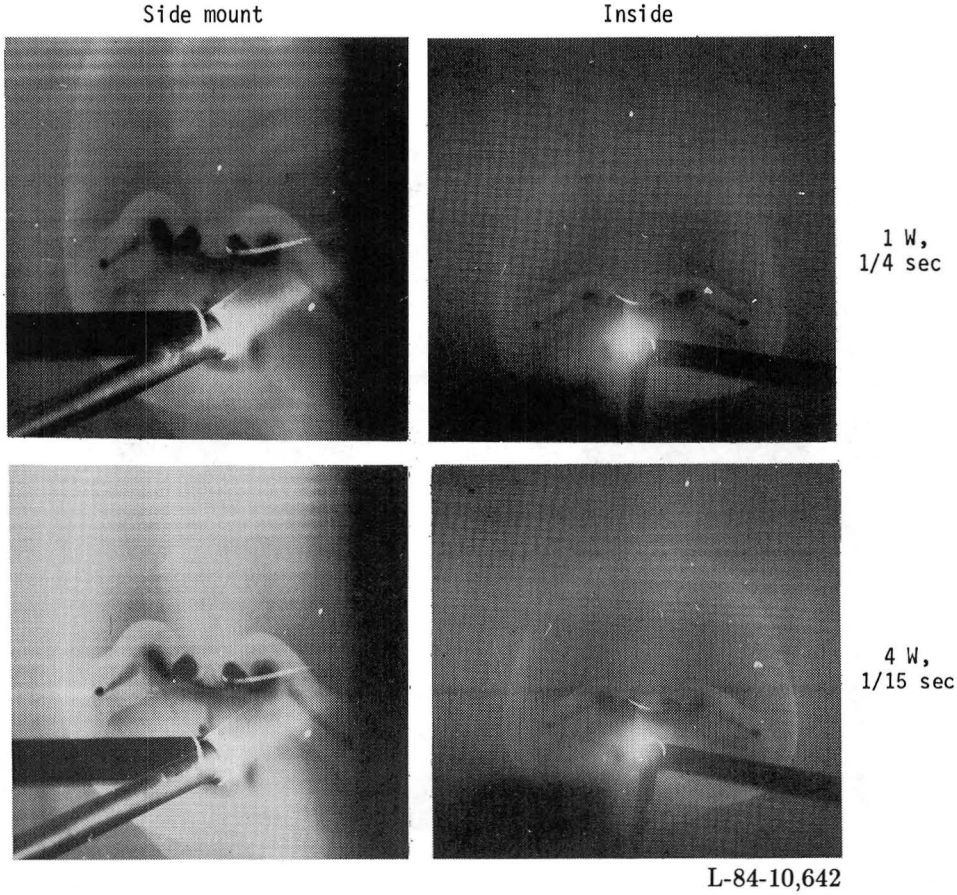

L-84-10,642

Figure 29. Exposure tests with laser light source.

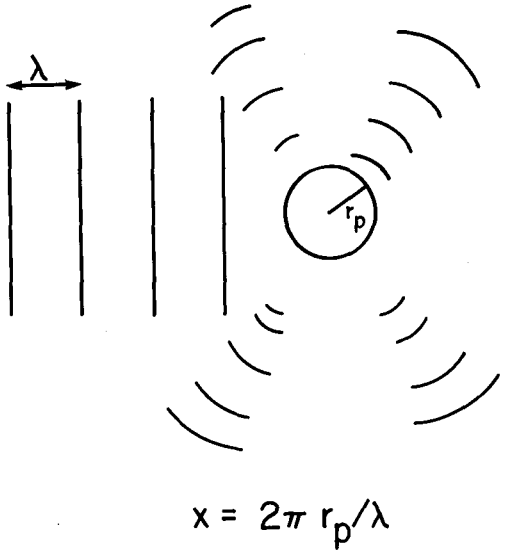

(a) Schematic of problem.

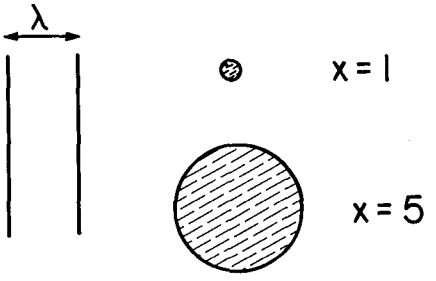

(b) Relative sizes of particles and wavelength for two cases for which calculations were made.

Figure 30. Classic Mie theory for plane waves scattering from spherical particles of radius r_p.

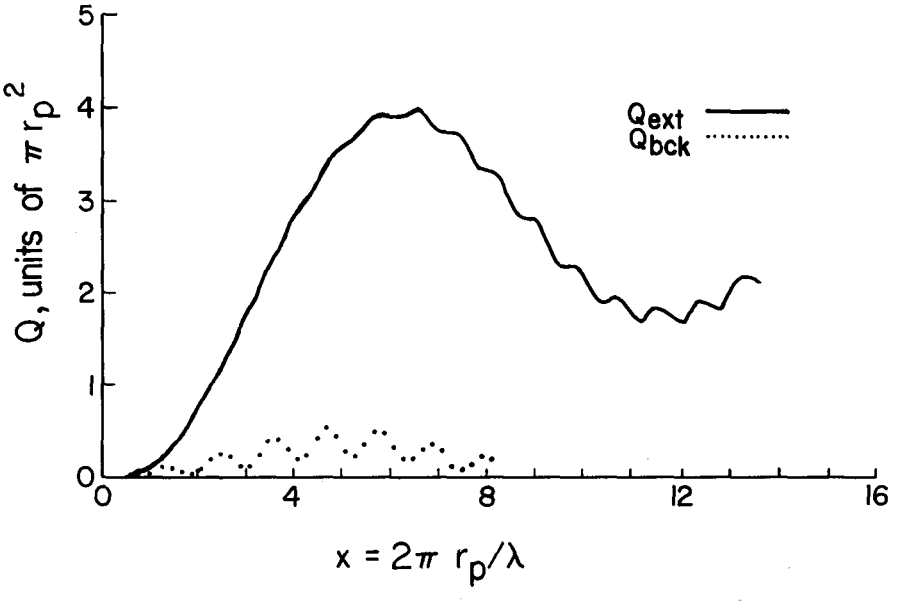

Figure 31. Scattering efficiency as function of size parameter for spherical particles having refractive index of water ($n' = 1.33$).

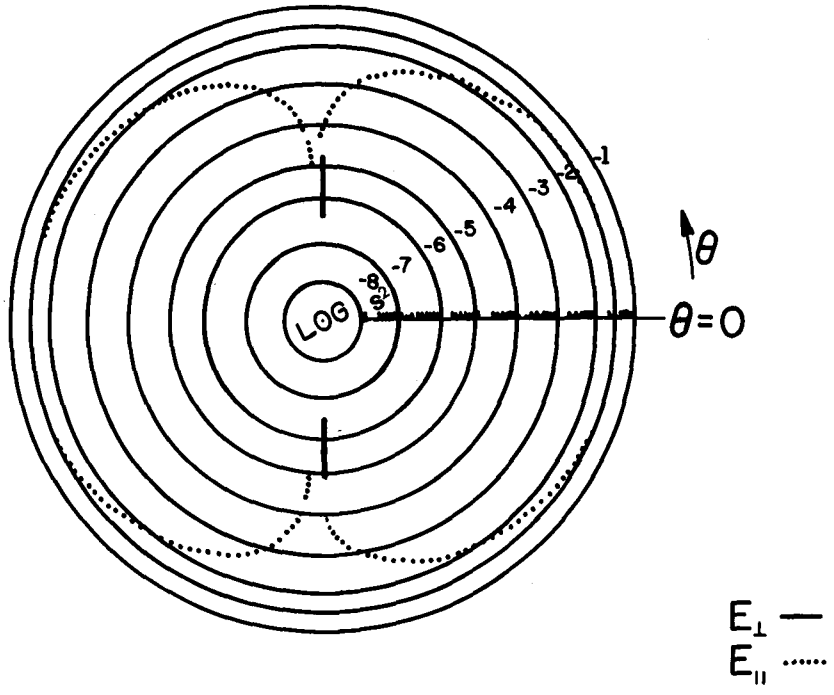

(a) Polar scattering diagram.

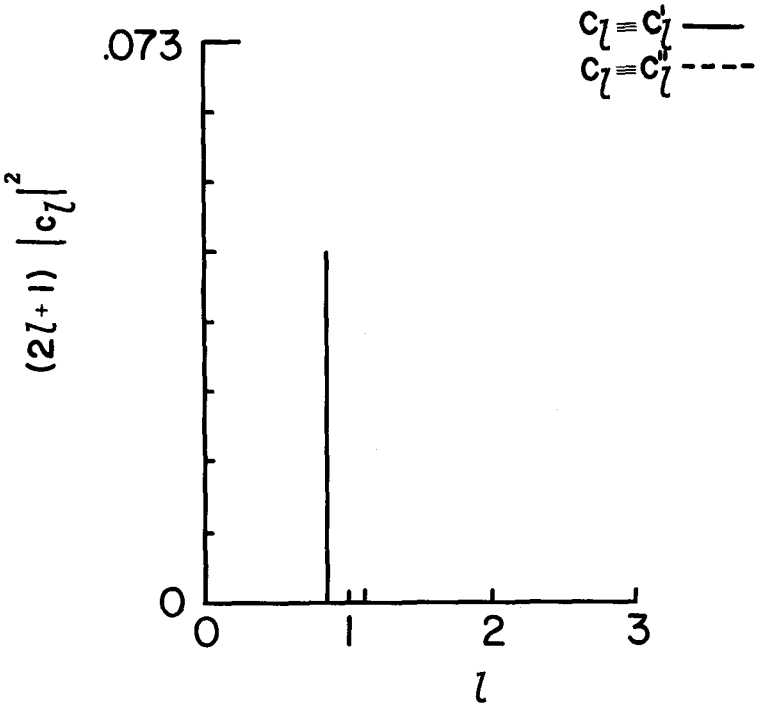

(b) Expansion coefficients.

Figure 32. Polar scattering and expansion coefficients for particles having size parameter of 1 and refractive index of water ($n' = 1.33$).

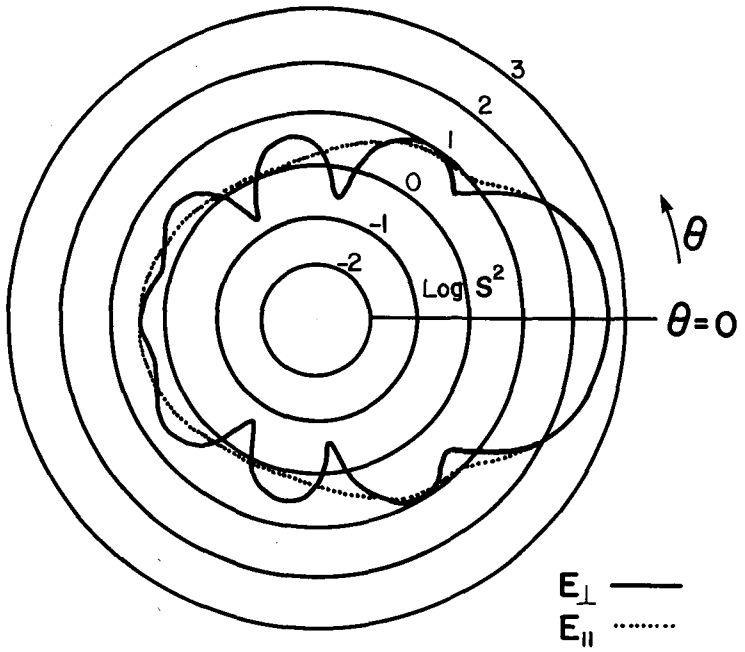

(a) Polar scattering diagram.

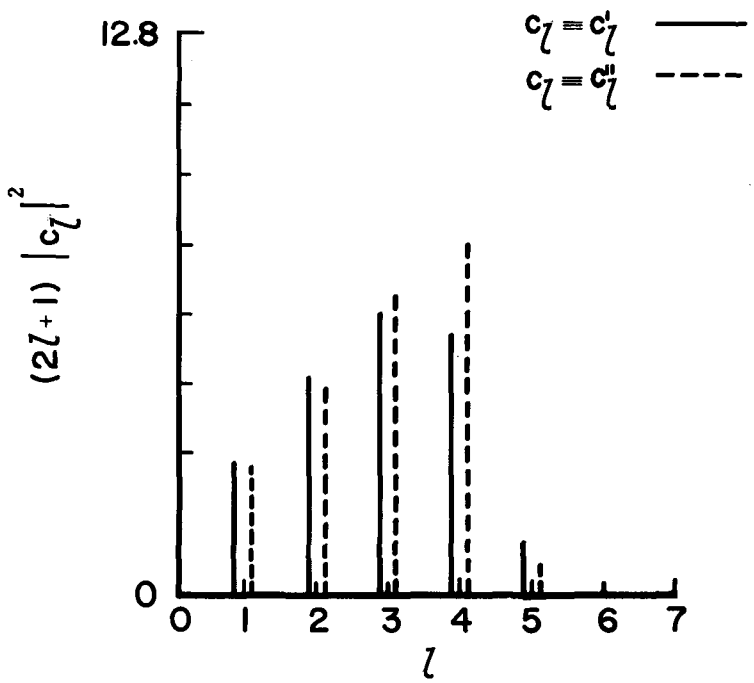

(b) Expansion coefficients.

Figure 33. Polar scattering and expansion coefficients for particles having size parameter of 5 and refractive index of water ($n' = 1.33$).

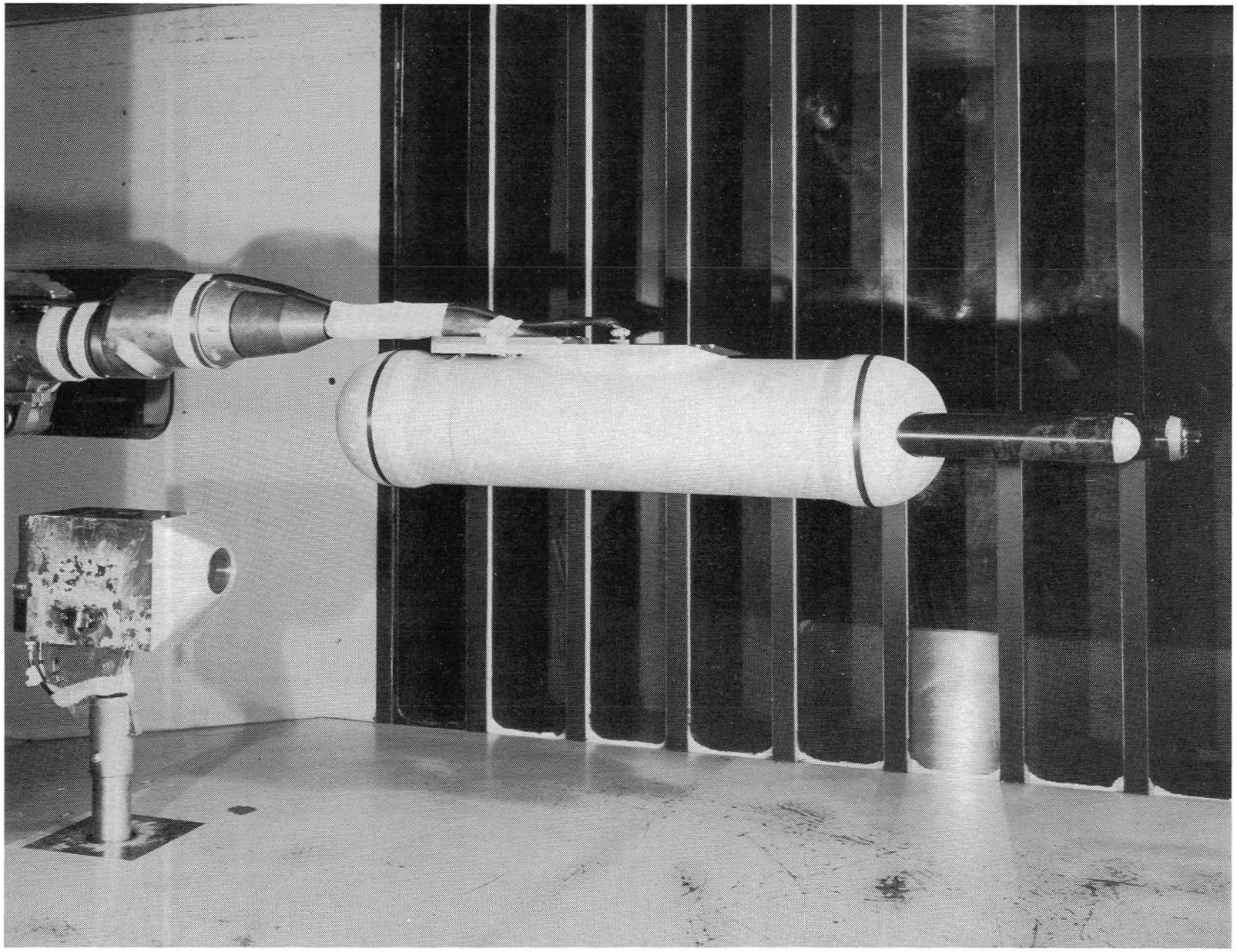

L-77-7087

Figure 34. Particle sizing probe mounted in test section.

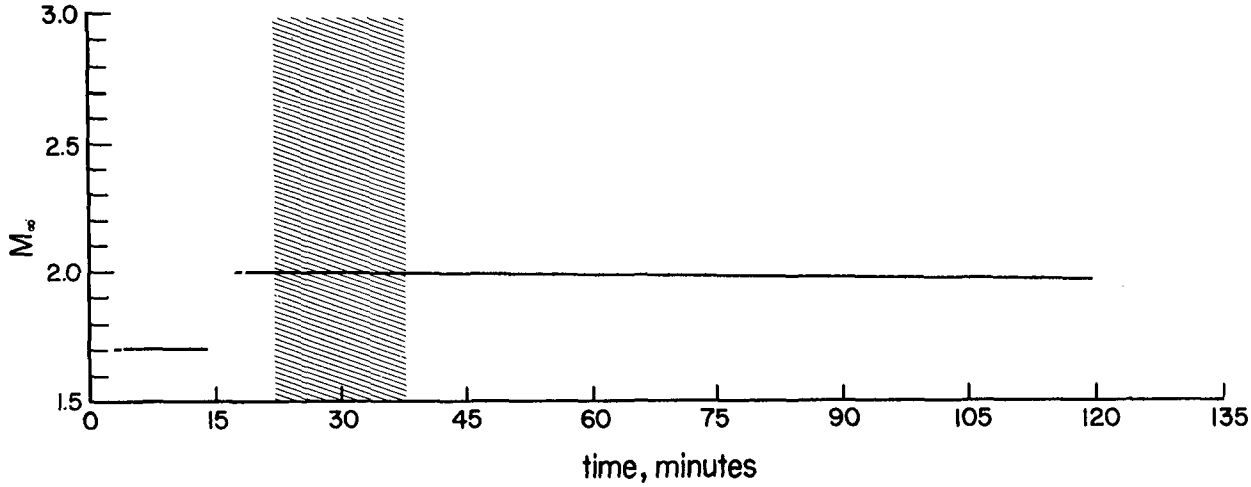

(a) Variation of Mach number.

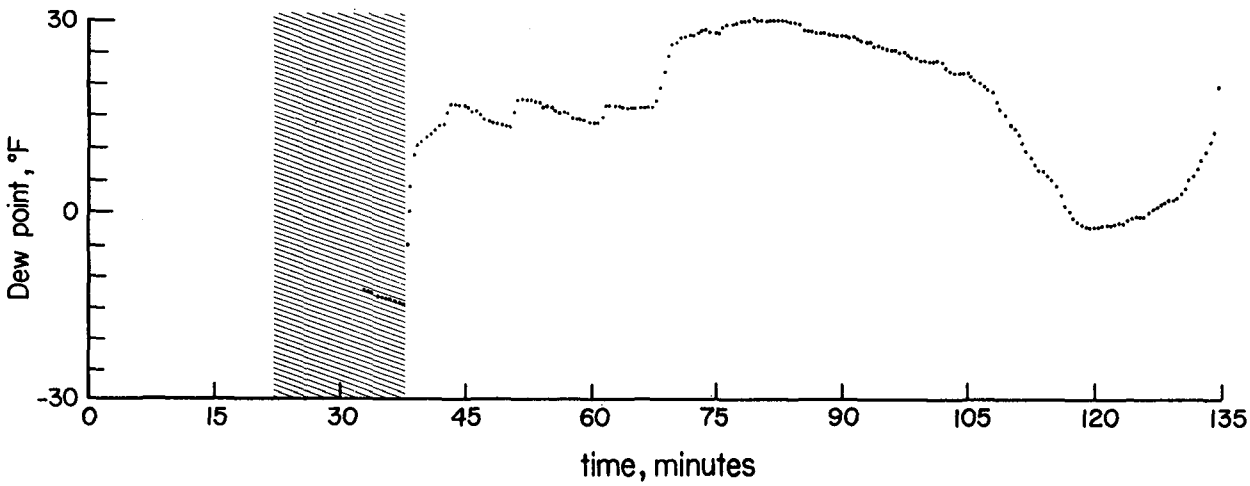

(b) Dew point as function of time.

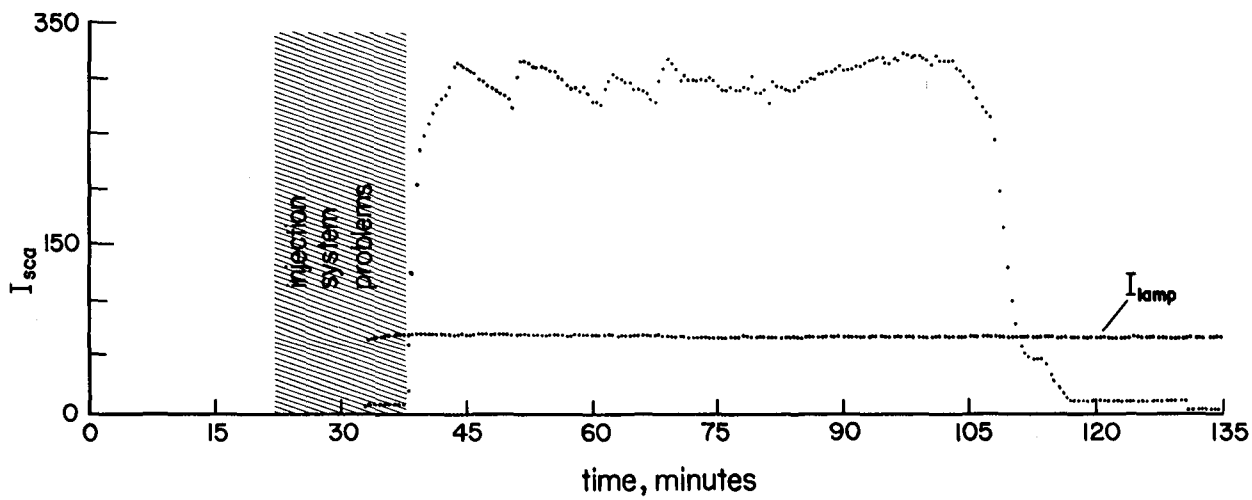

(c) Variation of scattered light.

Figure 35. Variation of scattered light as dew point varies for Mach number of 2.0.

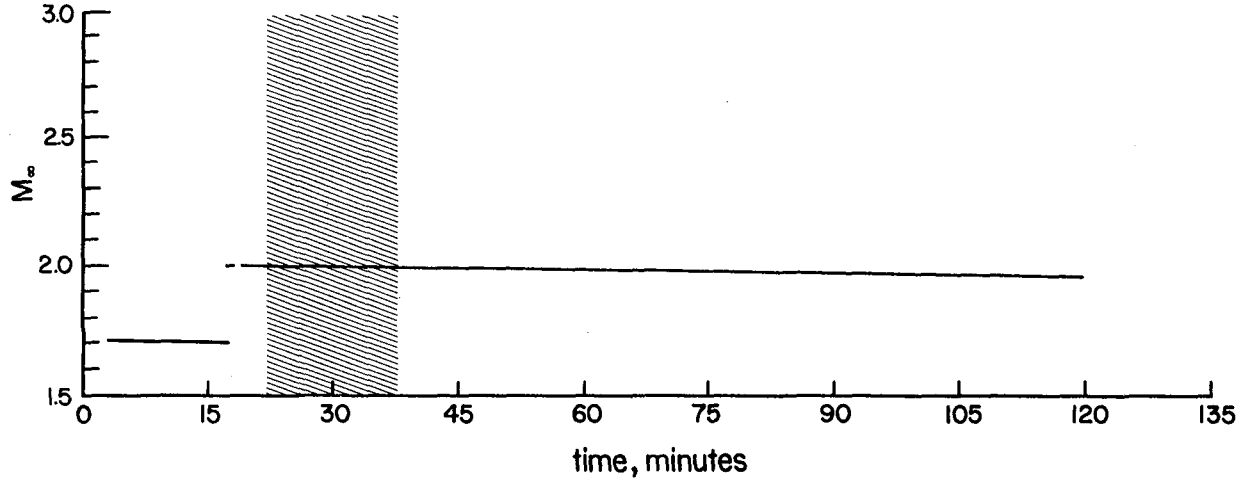

(a) Variation of Mach number.

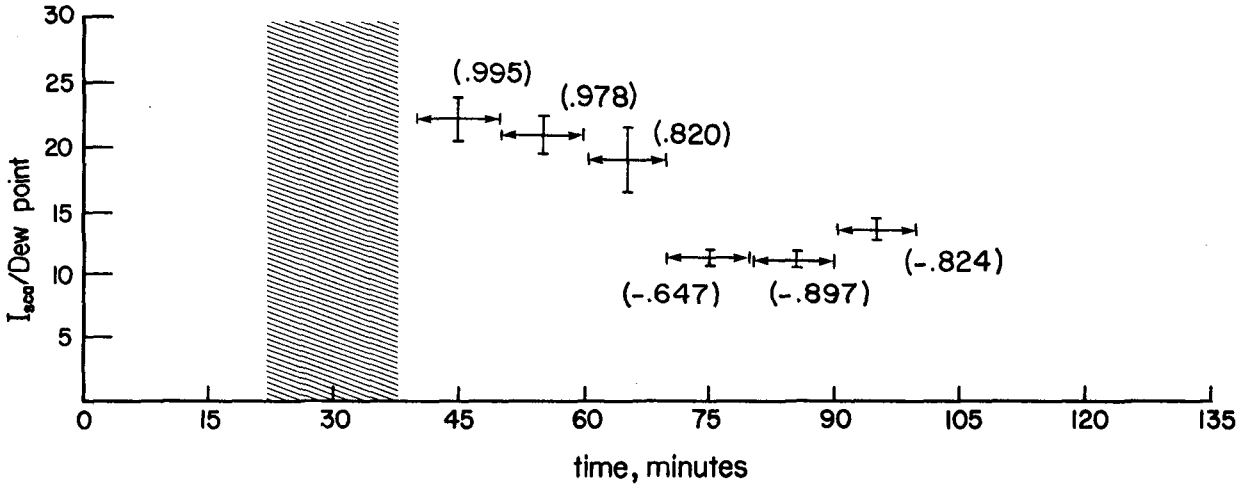

(b) Mean and variance.

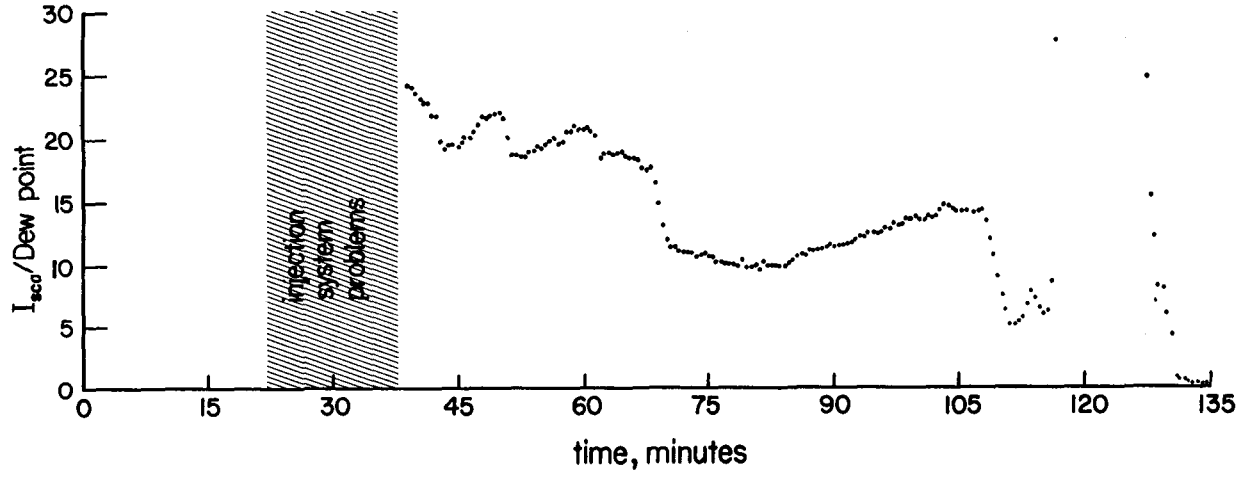

(c) Computed ratio.

Figure 36. Computed ratio of scattered light to dew point for fixed Mach number of 2.0.

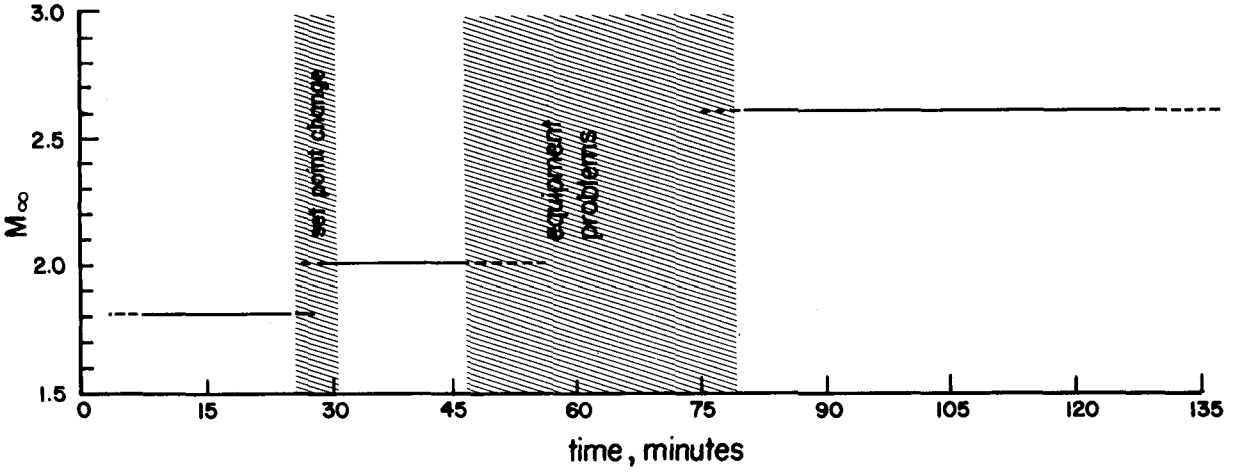

(a) Variation of Mach number. Dashes indicate regions where "set point" was not established.

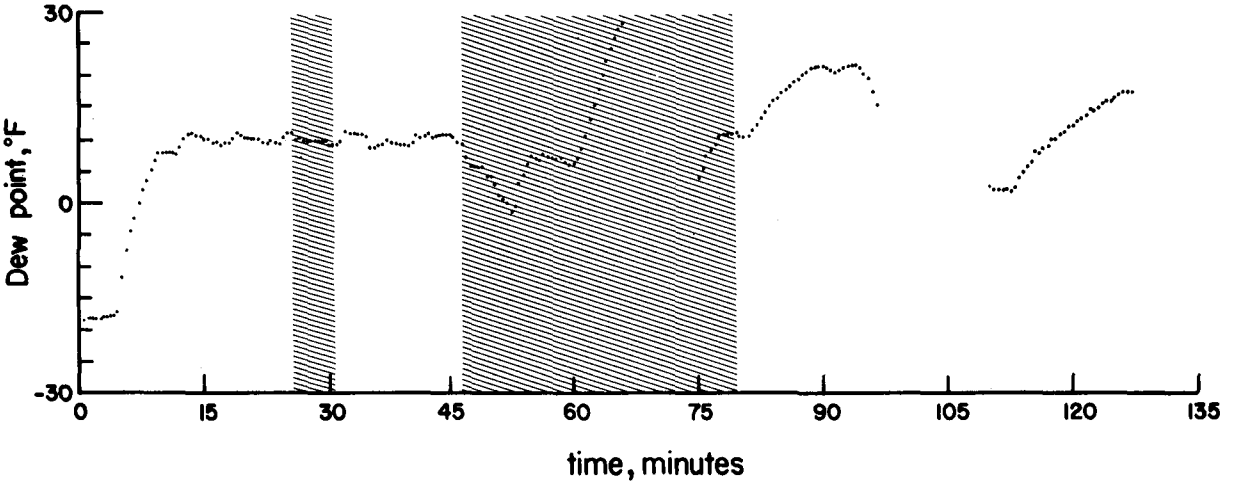

(b) Variation of dew point.

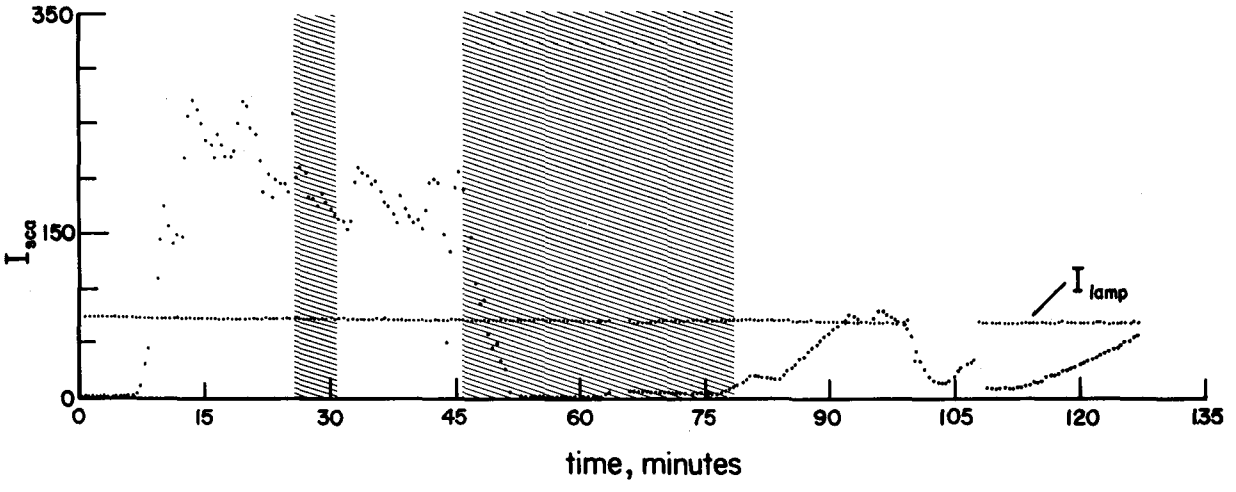

(c) Variation of scattered light.

Figure 37. Variation of scattered light as dew point and Mach number varies.

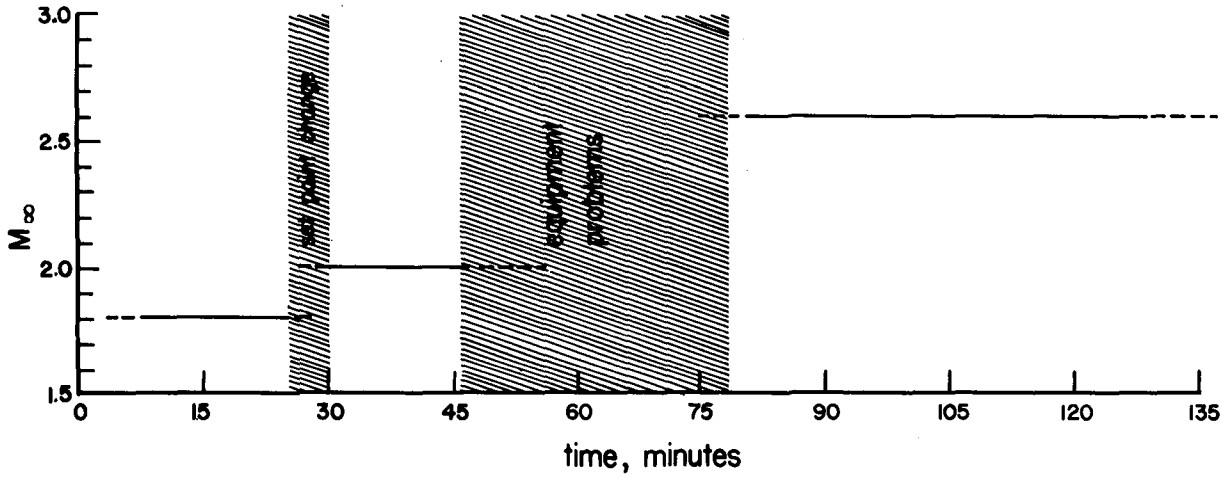

(a) Variation of Mach number.

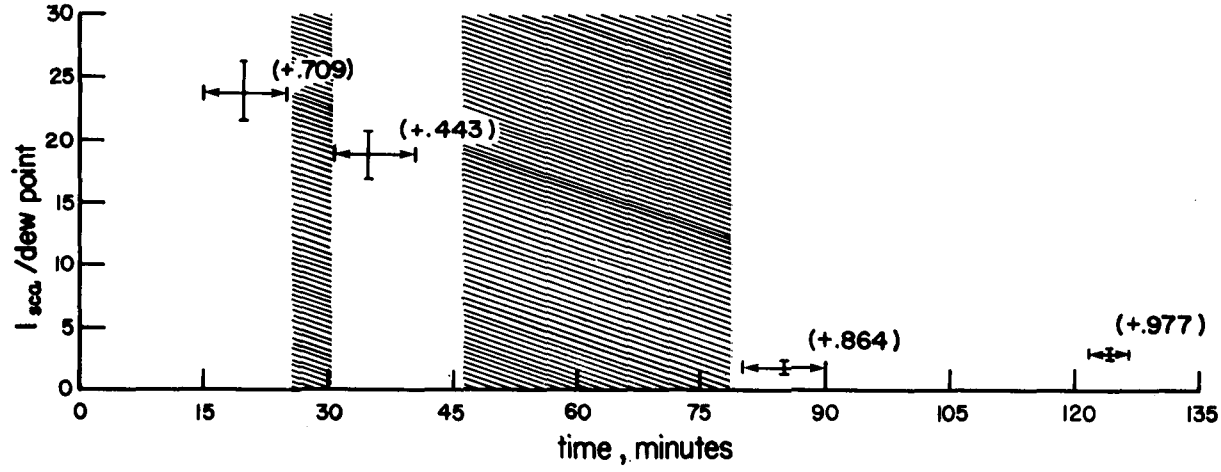

(b) Mean and variance of ratio.

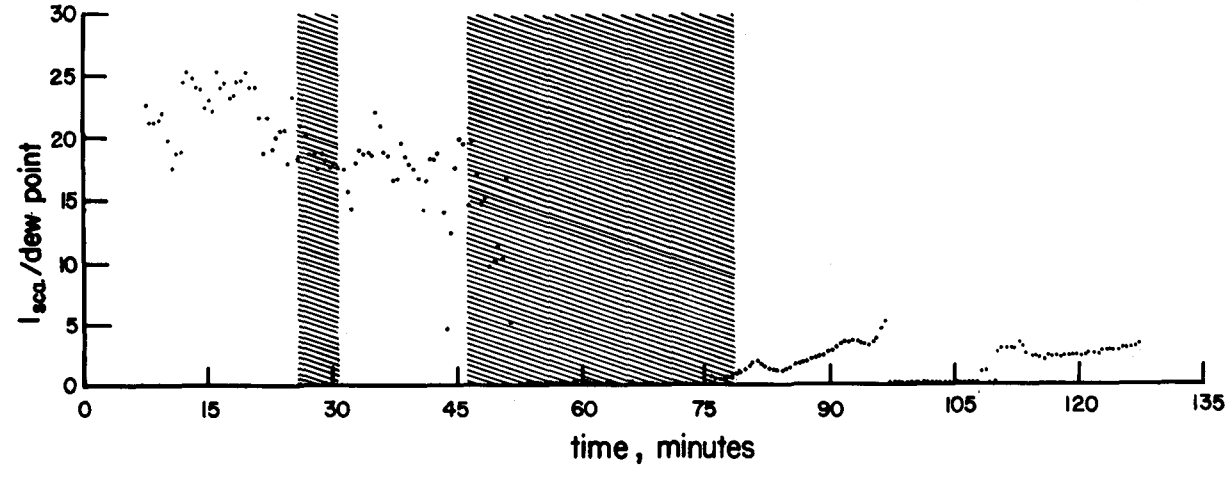

(c) Computed ratio.

Figure 38. Computed ratio of scattered light to dew point for varying Mach numbers. Rhodamine 6G dye was mixed with injection water during 105- to 125-minute interval.

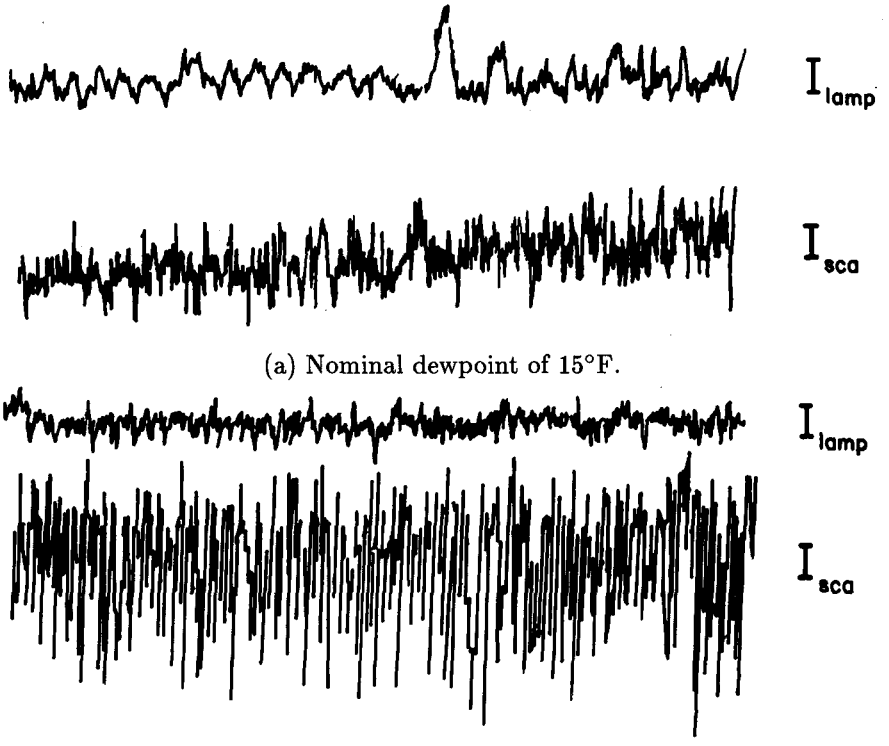

(a) Nominal dewpoint of 15°F.

(b) High dew point of 26°F.

Figure 39. Scattered light variation at Mach 2.0.

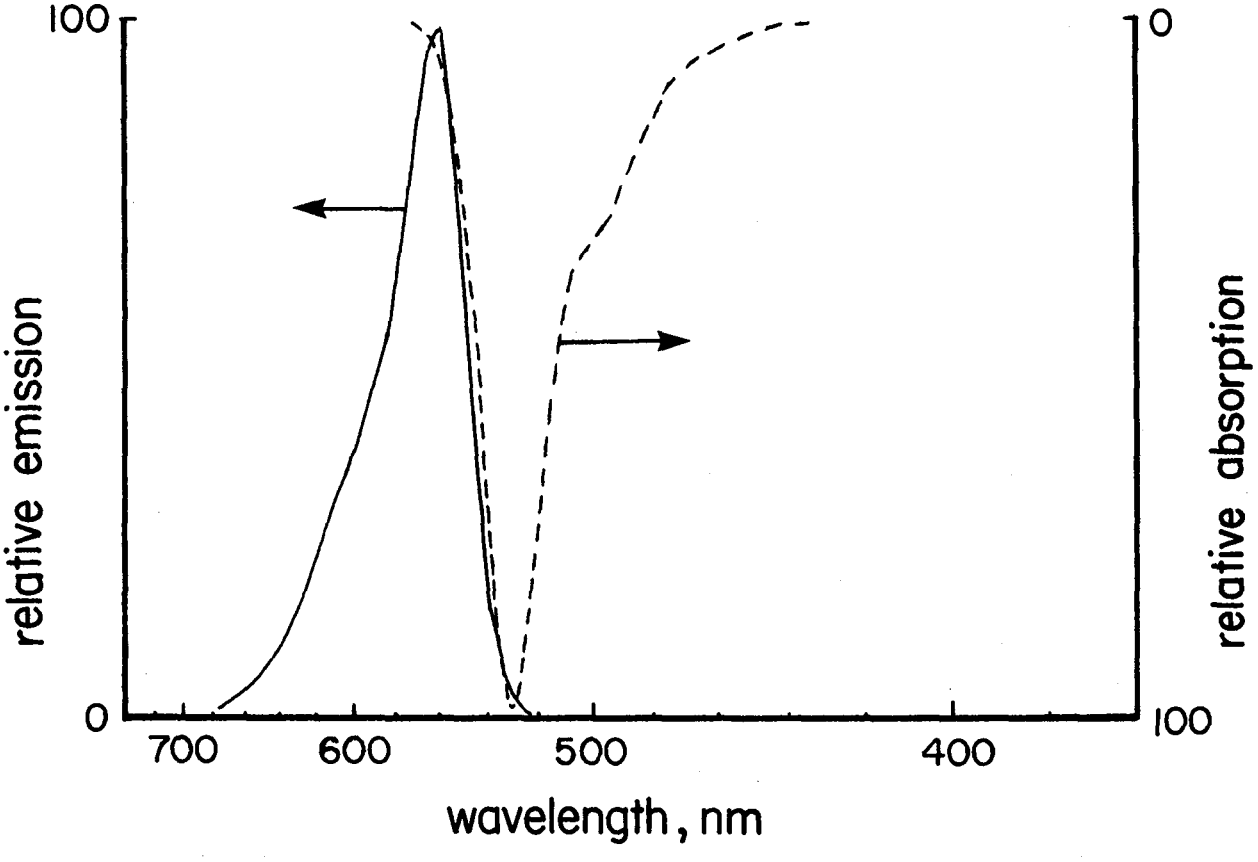

Figure 40. Emission-absorption characteristics of rhodamine 6G dye.

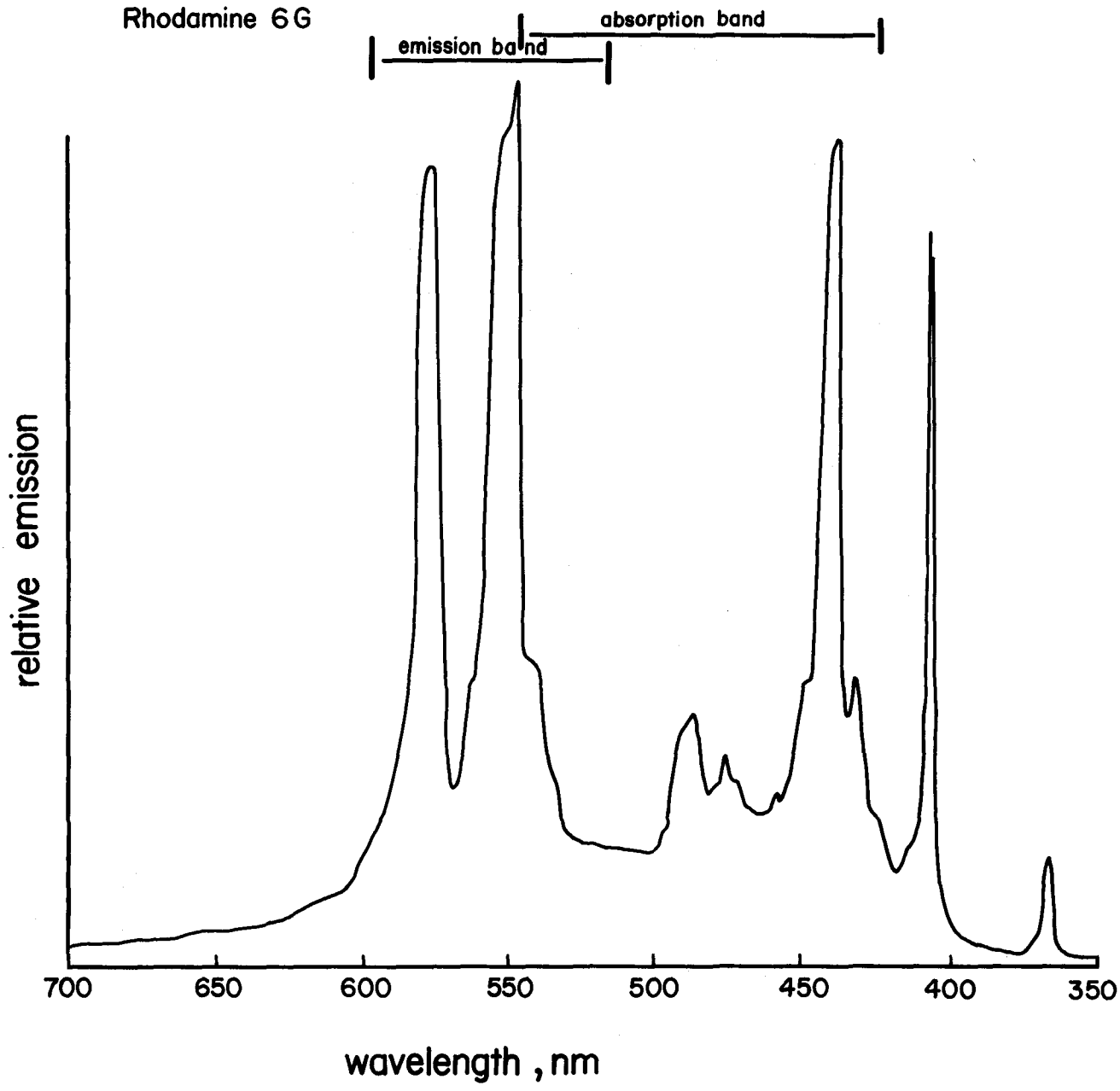

Figure 41. Emission-absorption intervals for rhodamine 6G superimposed on emission curves for a 1-kW high-pressure Hg lamp.

L-83-3992

Figure 42. Small commercially available dioctyl phthalate generator.

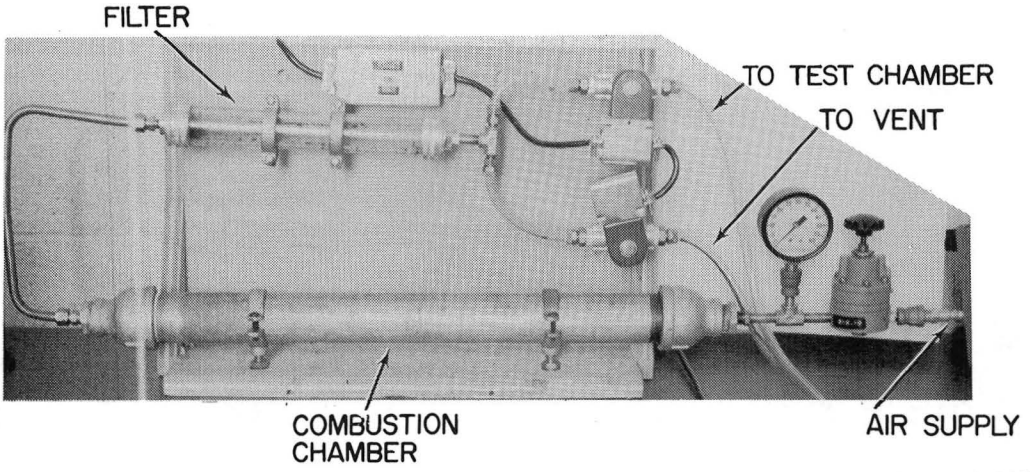

L-84-10,643

Figure 43. Smoke generator designed to burn wood shavings.

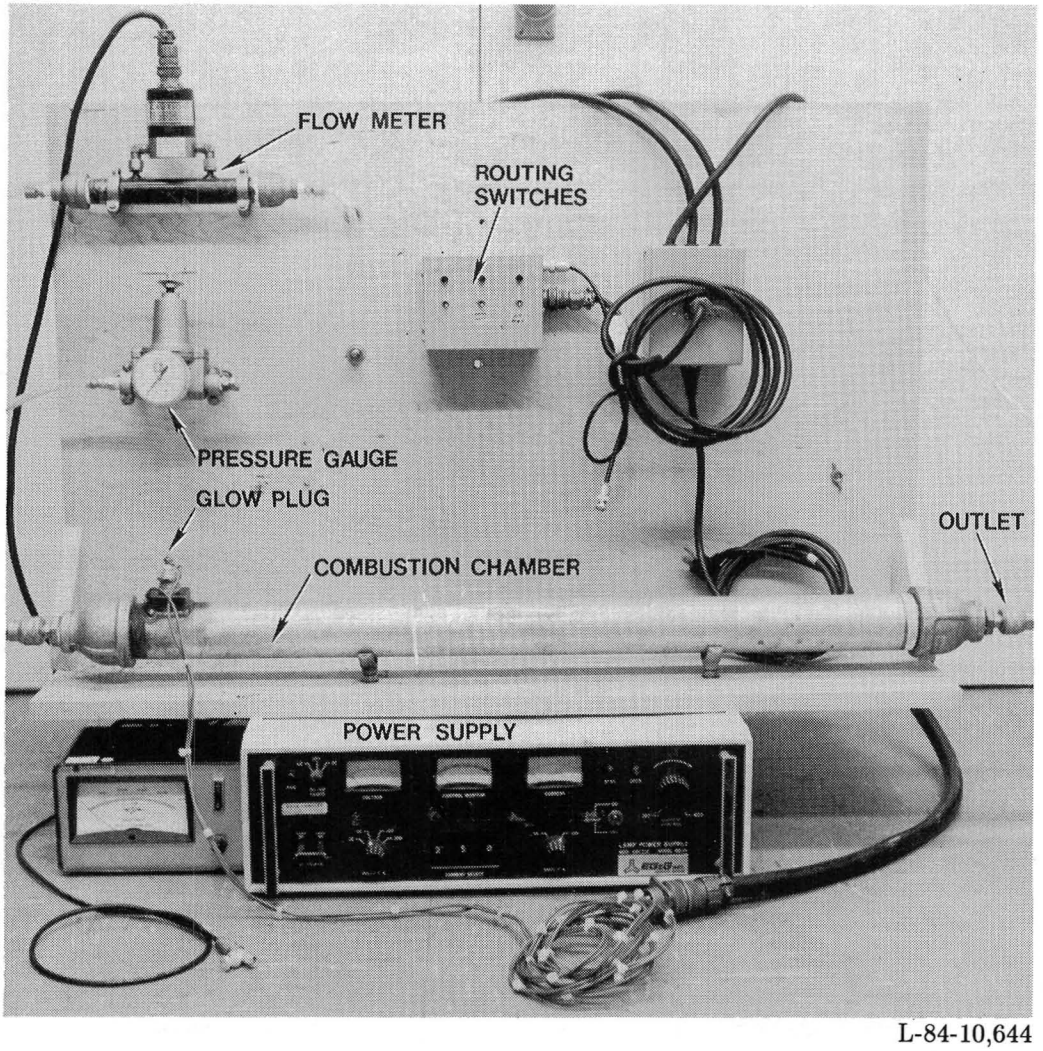

L-84-10,644

Figure 44. Frontal view of second model of smoke generator.

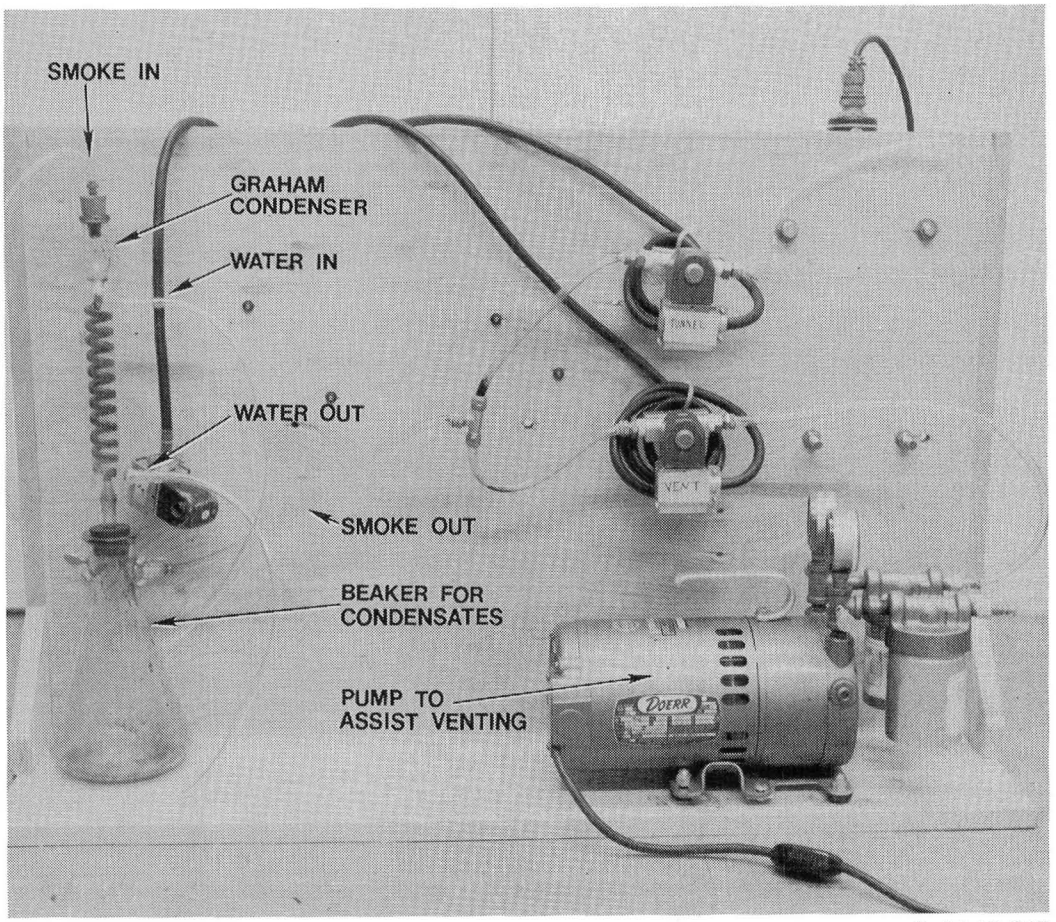

L-84-10,645

Figure 45. Rear view of second model of smoke generator.

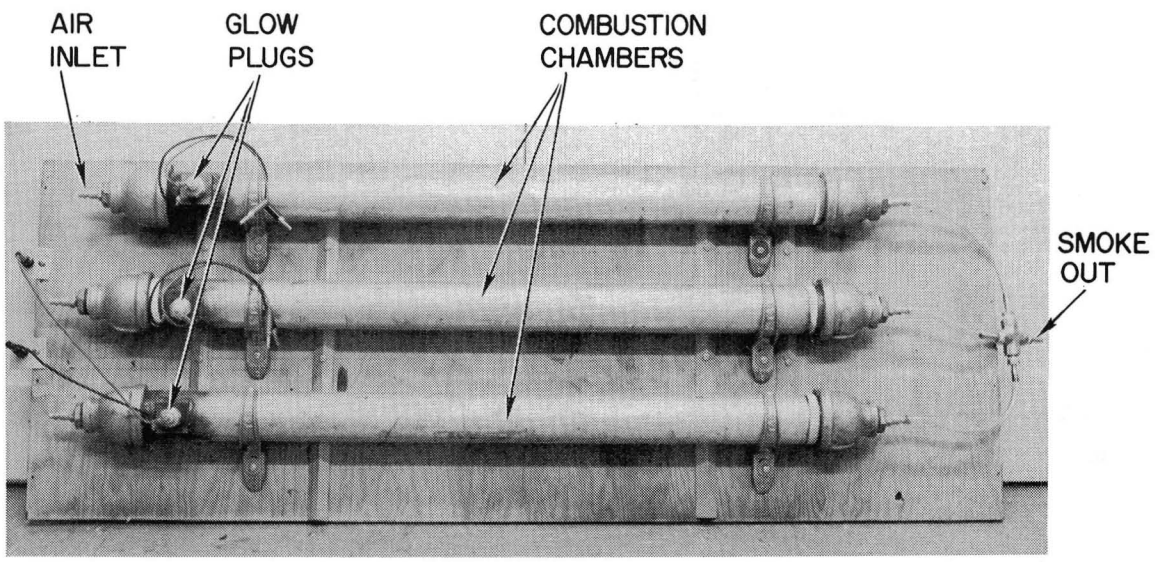

L-84-10,646

Figure 46. Third model of smoke generator.

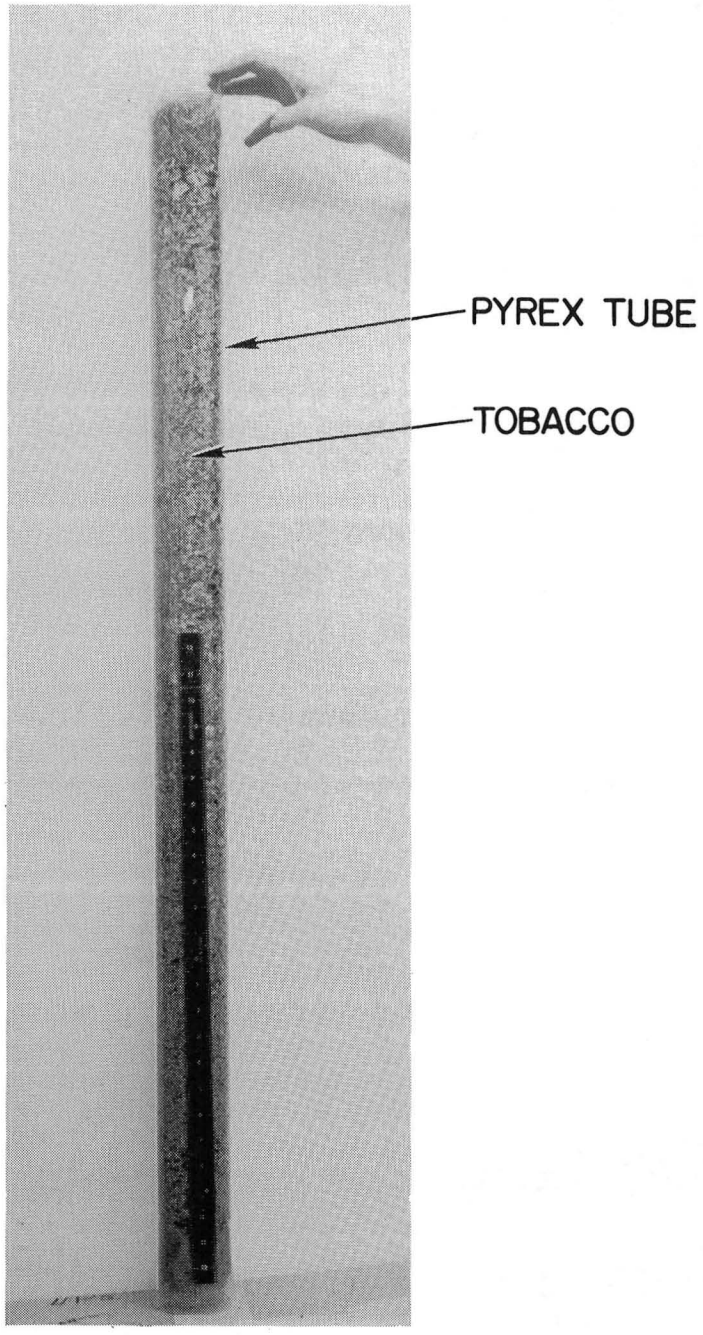

L-84-10,654

Figure 47. Pyrex tube filled with tobacco so combustion could be visually monitored. Dimensions, 3 in. diam. by 48 in. long.

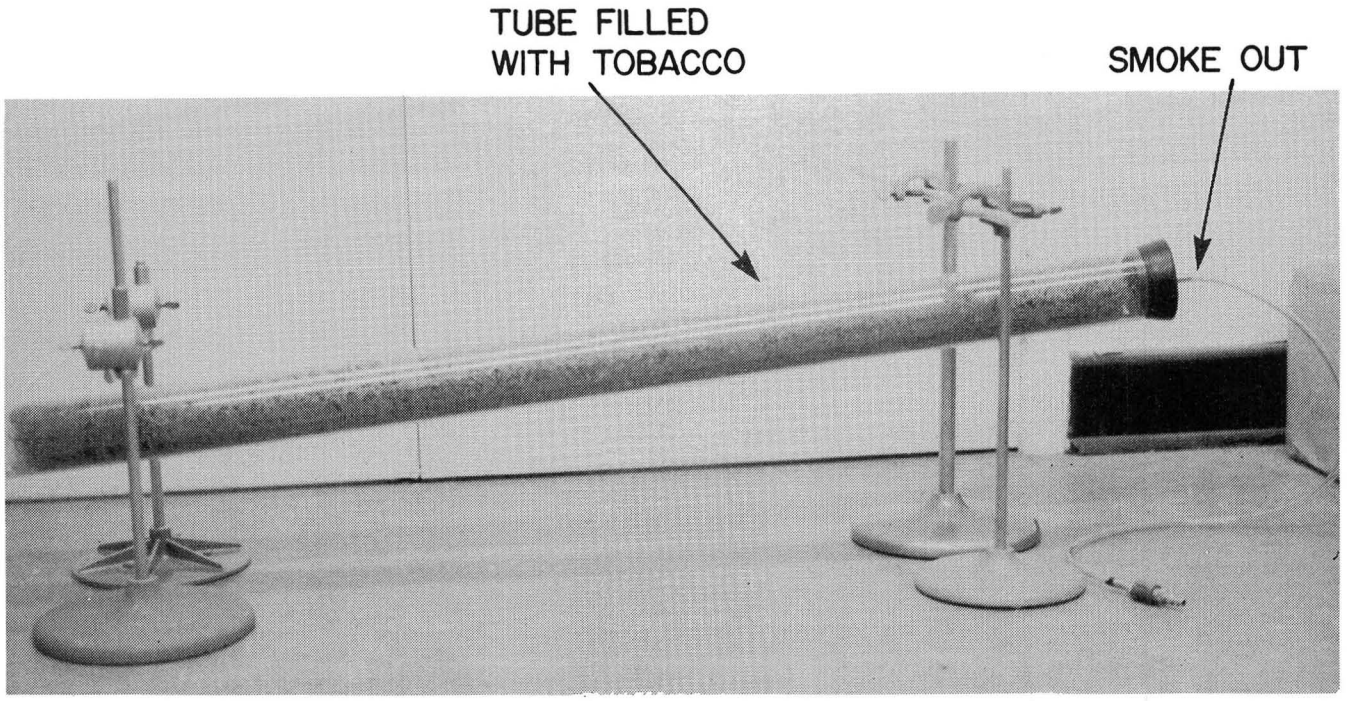

L-84-10,647

Figure 48. Tobacco-filled tube mounted for tunnel testing.

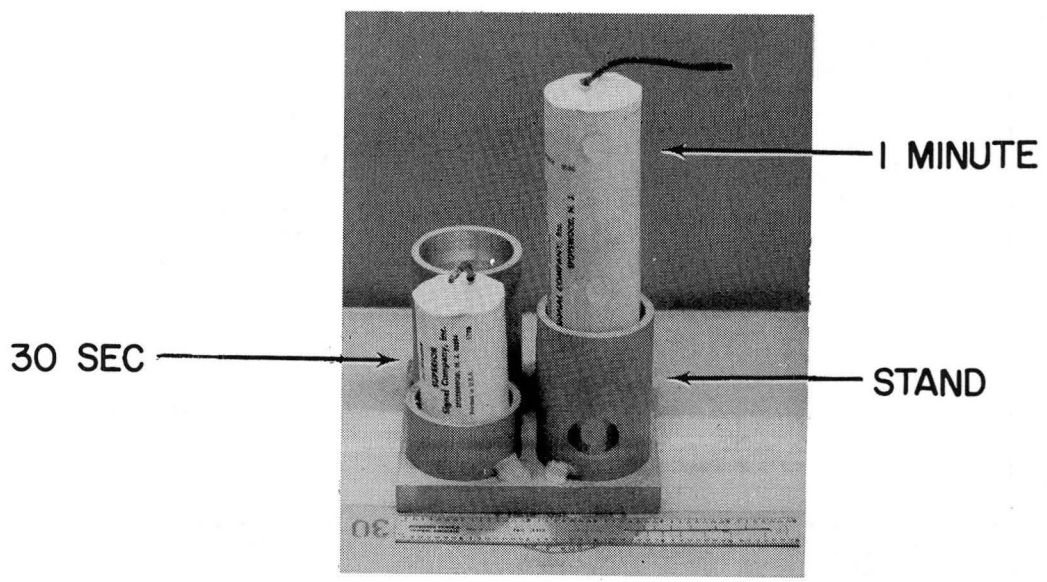

L-84-10,648

Figure 49. Commercially available smoke candles held in aluminum stand.

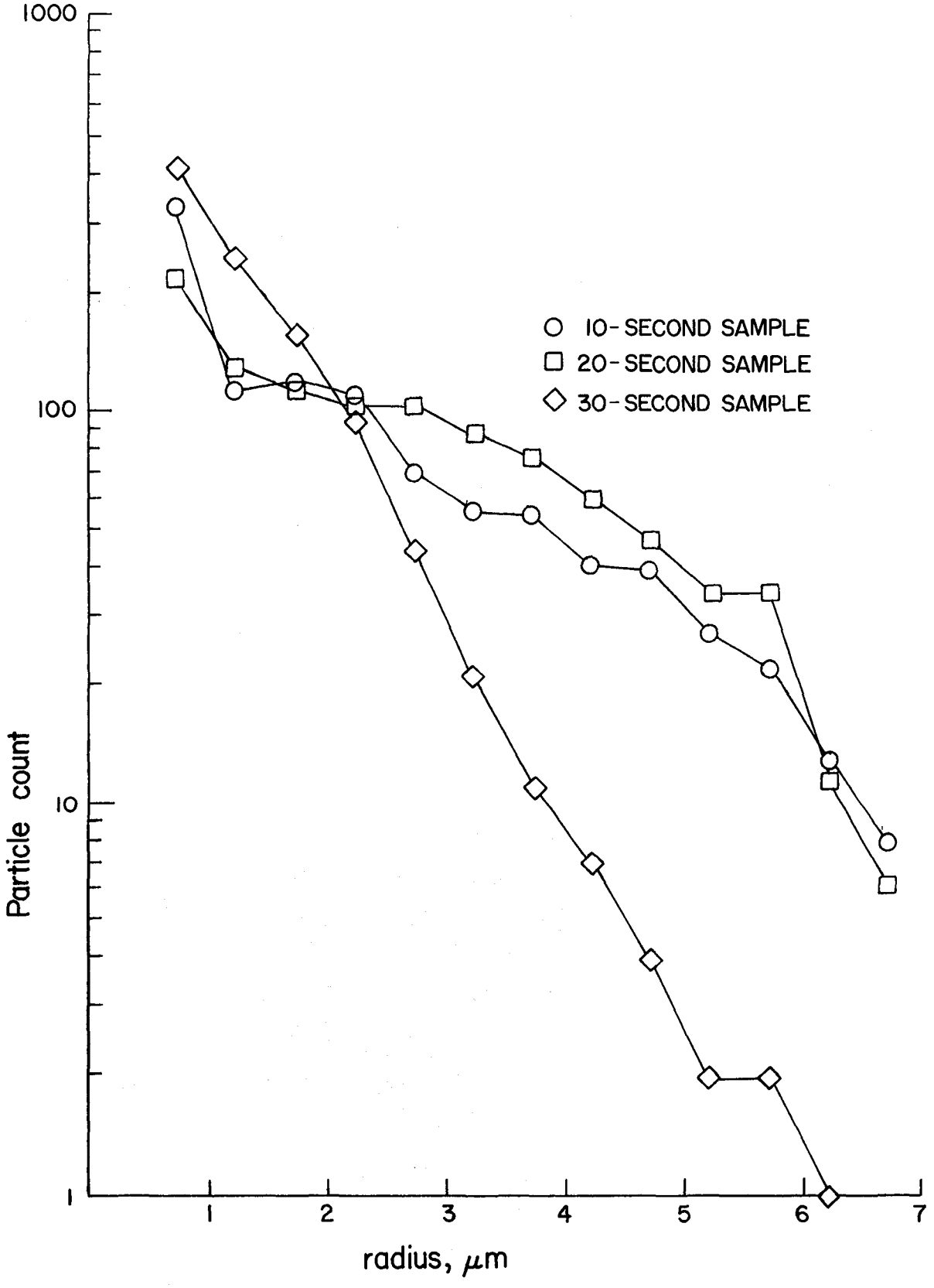

Figure 50. Measured size distributions of smoke-candle particles determined with Knollenberg FSSP instrument.

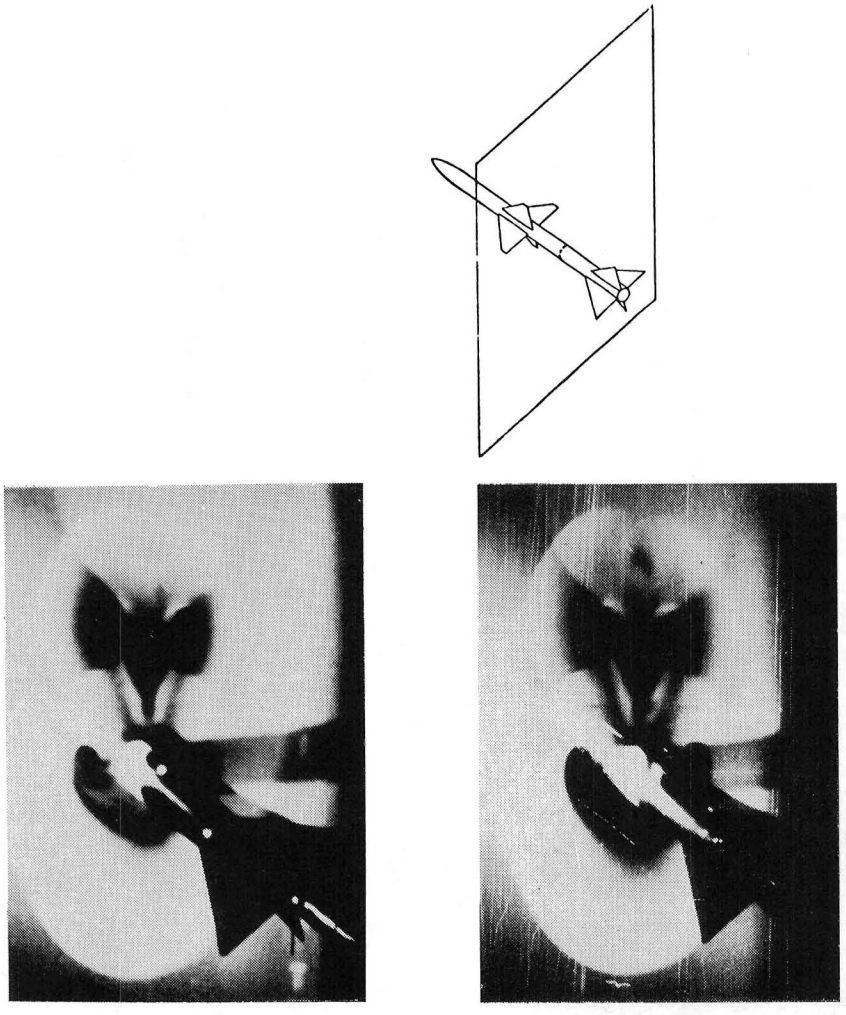

L-84-10,649

Figure 51. Comparison of vapor screen and smoke screen generated by candles. Mach number, 2.35; angle of attack, 30°; roll angle, 45°.

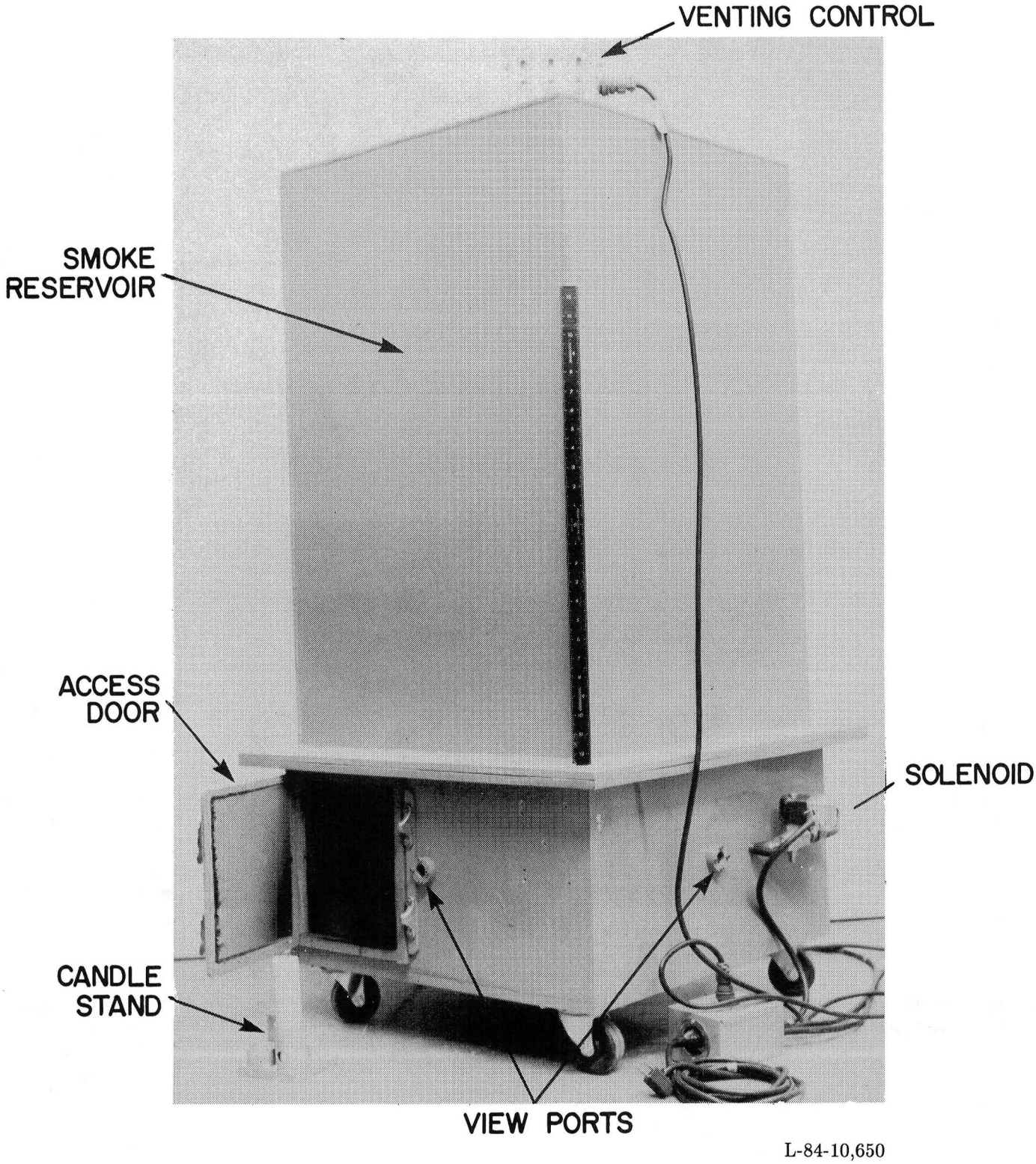

L-84-10,650

Figure 52. Chamber used to buffer smoke-candle output.

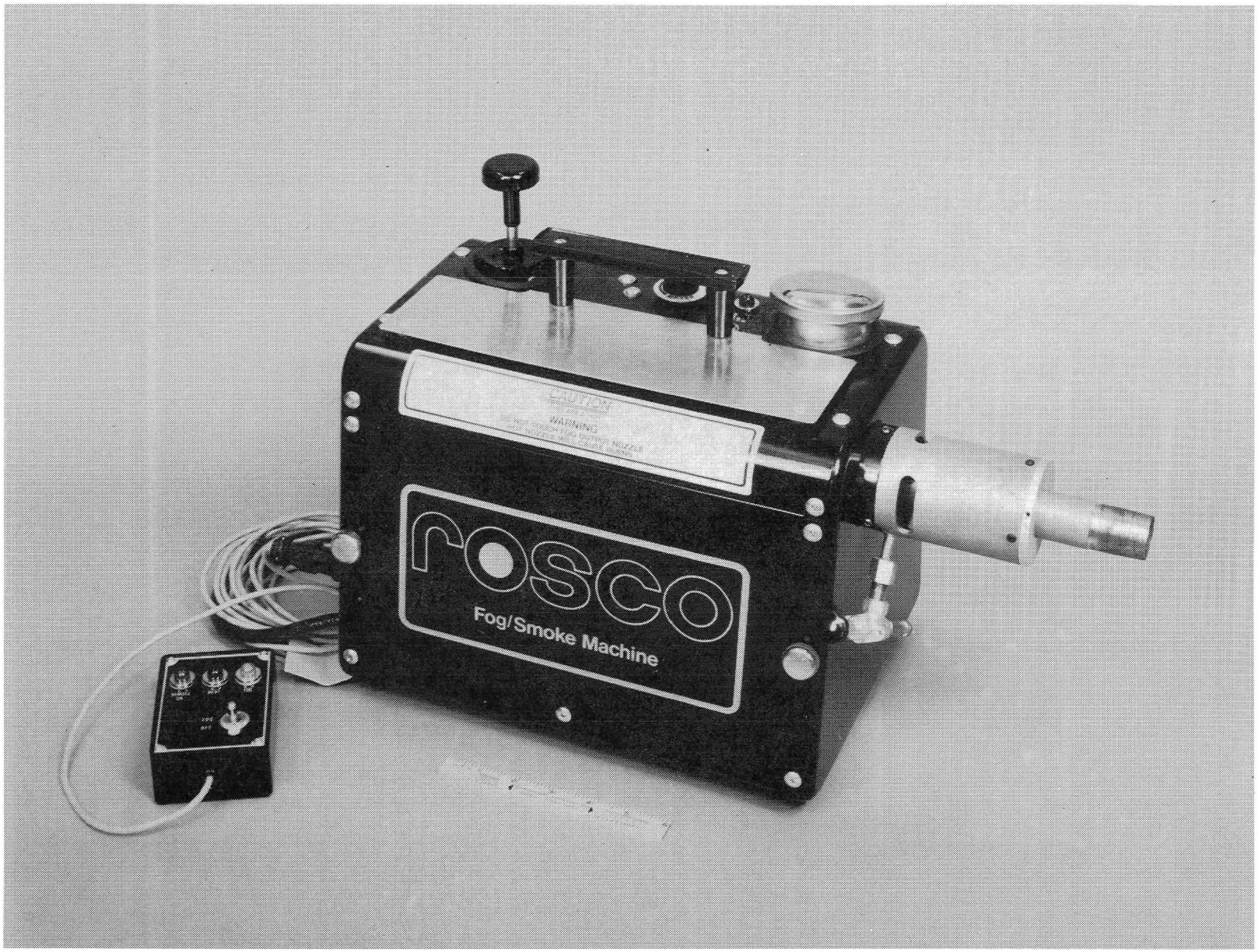

L-83-3993

Figure 53. Aerosol generator sold primarily for theatrical use.

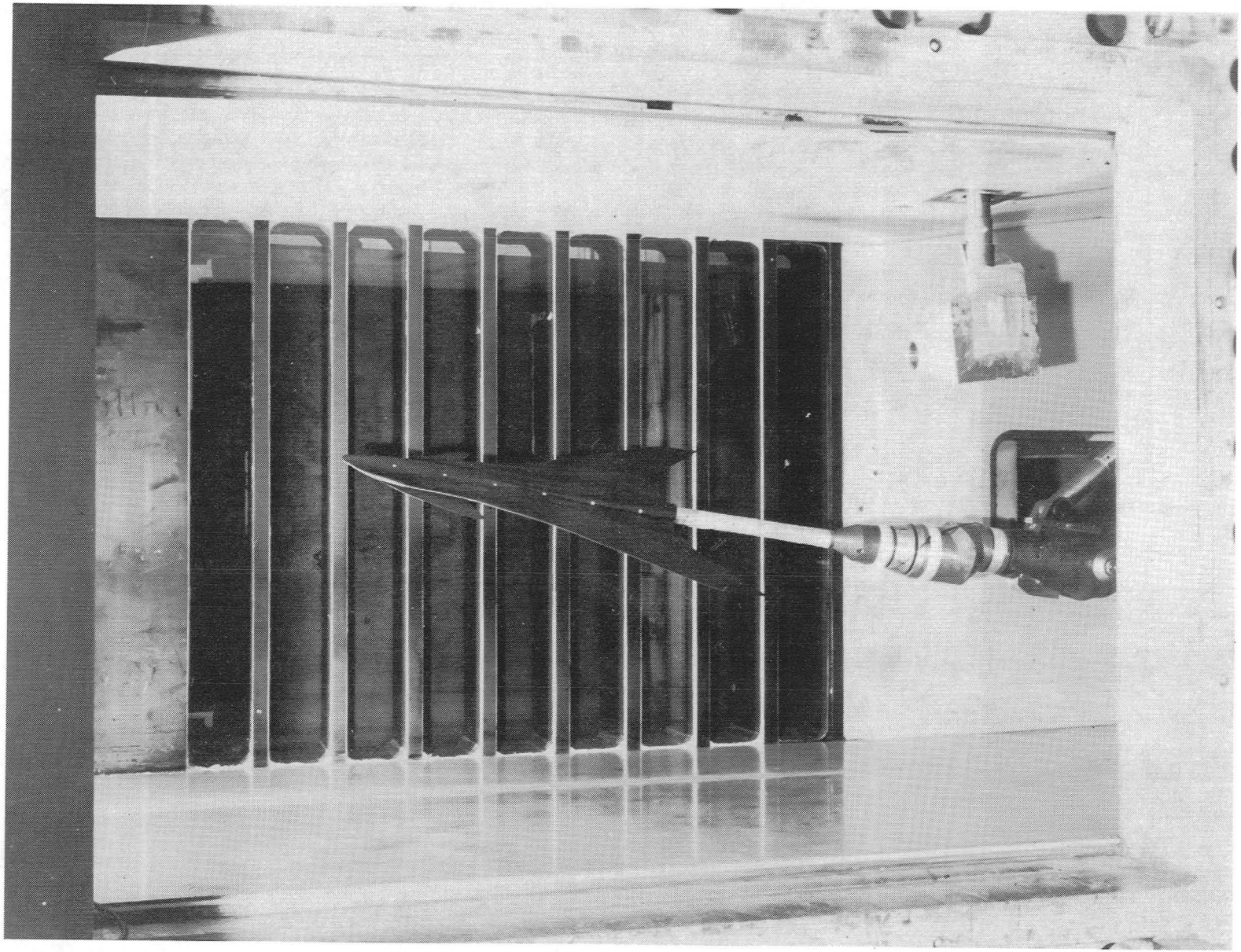

L-84-10,651

Figure 54. Model and inside camera mounted in tunnel.

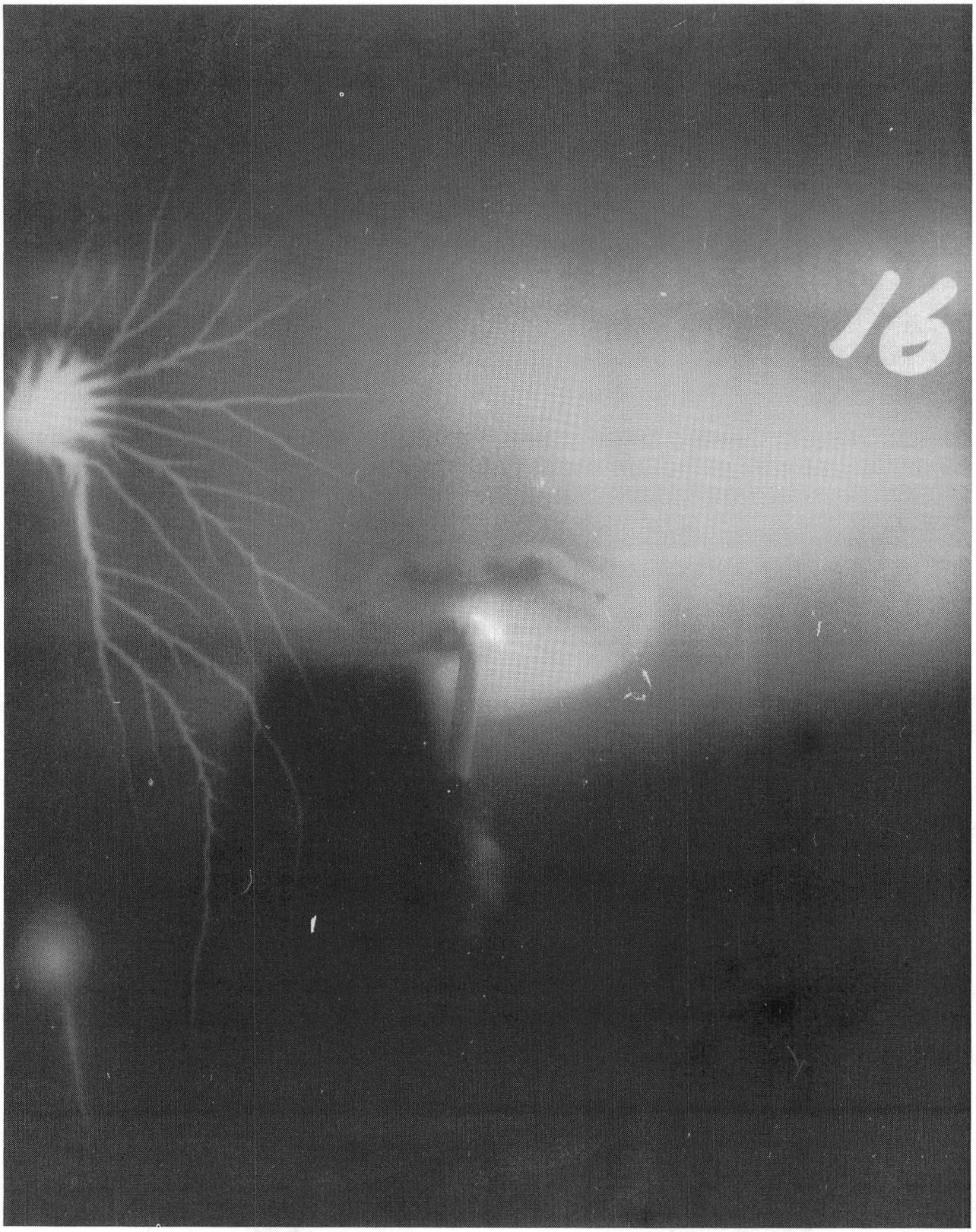

L-84-10,652

Figure 55. Discharge patterns which occasionally occur on data frames despite grounding attempts.

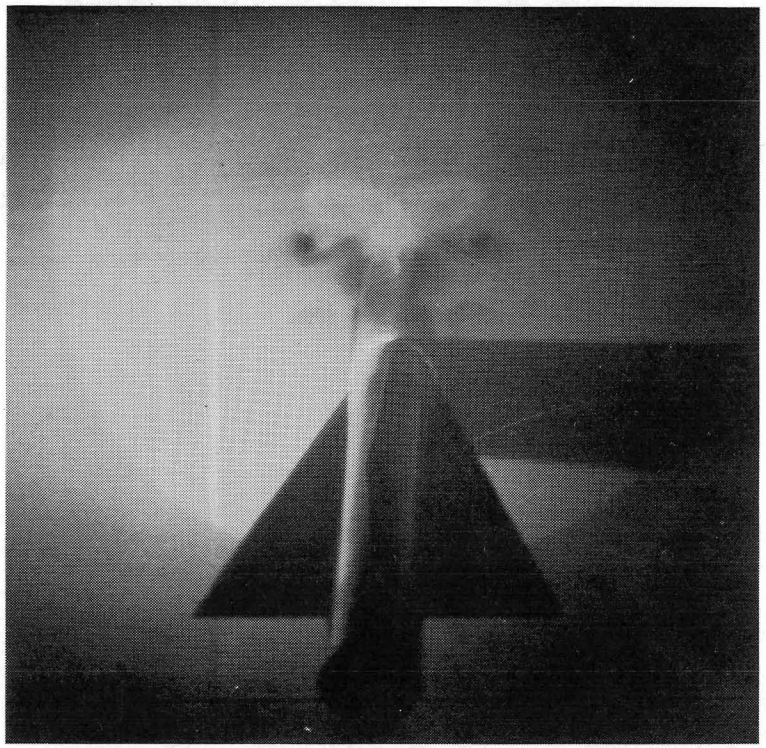

Periscope view

Side-mount view

L-84-10,653

Figure 56. Demonstration of the prototype periscope system. Exposure time at $f/11$ was 1 sec for periscope system; exposure time at $f/2.8$ was 1/8 sec for side-mount system. Mach number, 2.30; angle of attack, 29°.

1. Report No.	2. Government Accession No.	3. Recipient's Catalog No.
NASA TM-86290		

4. Title and Subtitle	5. Report Date
INVESTIGATION OF LIGHT SOURCE AND SCATTERING MEDIUM RELATED TO VAPOR-SCREEN FLOW VISUALIZATION IN A SUPERSONIC WIND TUNNEL	December 1984
	6. Performing Organization Code: 505-43-23-02
7. Author(s): Walter L. Snow and Odell A. Morris	8. Performing Organization Report No.: L-15836
9. Performing Organization Name and Address: NASA Langley Research Center, Hampton, VA 23665	10. Work Unit No.
	11. Contract or Grant No.
12. Sponsoring Agency Name and Address: National Aeronautics and Space Administration, Washington, DC 20546	13. Type of Report and Period Covered: Technical Memorandum
	14. Sponsoring Agency Code

15. Supplementary Notes

16. Abstract

Methods for increasing the radiant energy in light sheets used for vapor screen set-ups were investigated. Both high-pressure mercury arc lamps and lasers were considered. Pulsed operation of the air-cooled 1-kW lamps increased the light output but decreased reliability. An ellipsoidal mirror improved the output of the air-cooled lamps by concentrating the light but increased the complexity of the housing. Water-cooled 4-kW lamps coupled with high-aperture Fresnel lenses provided reasonable improvements over the air-cooled lamps. Fanned laser beams provided high-quality results and would afford greater flexibility for beam manipulation. Included also are measurements of scattered light versus dew point made in conjunction with successful attempts to control the fluid injection. A number of smoke generators are described and test results comparing smoke and vapor screens are shown. Finally, one test included a periscope system to relay the image to a camera outside the flow.

17. Key Words (Suggested by Authors(s))
Vapor screen
Light sheets
Mie scattering
Flow visualization

18. Distribution Statement
Unclassified—Unlimited

Subject Category 35

19. Security Classif.(of this report)	20. Security Classif.(of this page)	21. No. of Pages	22. Price
Unclassified	Unclassified	64	A04

For sale by the National Technical Information Service, Springfield, Virginia 22161

NASA-Langley, 1984

National Aeronautics and
Space Administration

Washington, D.C.
20546

Official Business
Penalty for Private Use, $300

THIRD-CLASS BULK RATE

Postage and Fees Paid
National Aeronautics and
Space Administration
NASA-451

NASA

POSTMASTER: If Undeliverable (Section 158
Postal Manual) Do Not Return